

**A Thesis for the Degree of Ph.D. in Science**

**Investigation of Geometric and Electronic Structures  
of Mass-selectively Deposited Superatom  
Nanoclusters by Photoelectron Spectroscopies**

**August 2016**

**Graduate School of Science and Technology**

**Keio University**

**Tsutomu Ohta**



## Acknowledgements

The contents of present thesis are the summaries and the author's work at Professor Nakajima group in School of Fundamental Science and Technology, Graduate School of Science and Technology, Keio University.

The author would like to express his best gratitude to Professor Atsushi Nakajima and Assistant Professor Masahiro Shibuta for their kind guidance, useful discussions, and enormous continuing supports during the research activities.

The author would like to be very grateful to Professor Kohei Itoh, Professor Hiroshi Kondoh, Professor Satoshi Yabushita, and Professor Naoki Yoshioka for making time in their busy schedules and offering constructive comments about this dissertation.

The author would like to thank Assistant Professor Hironori Tsunoyama, Associate Professor Toyoaki Eguchi at Tohoku University (belonged to Keio University by January 2016), Associate Professor Masato Nakaya at Nagoya University (belonged to Keio University by September 2014), Research associate Takeshi Iwasa at Hokkaido University (belonged to Keio University by September 2014), and Dr. Naoyuki Hirata for many beneficial discussions.

The author would like to be also very grateful to Associate Professor Yuichi Negishi at Tokyo University of Science and Assistant Professor Takashi Yamamoto at Keio University for great helps in performing the research.

The author would like to express his gratitude to all the members of the Physical Chemistry Research Group of Professor Nakajima and Professor Yabushita for their kindness and cooperation.

Finally, the author would like to express his hearty gratitude to his parents, his brother, and his friends for their heartfelt supports and encouragements.

This work is partly supported by JSPS KAKENHI of Grant-in-Aids for Young Scientists (B) grant no. 25810010 and for Scientific Research (A) grant no. 15H02002. The author is grateful to financial support from Gran-in Aid for JSPS Fellows.

Yokohama, Japan

August, 2016

Tsutomu Ohta

# Contents

	Acknowledgements	3
<b>1</b>	<b>General Introduction</b>	<b>8</b>
1.1	Introduction — potentials of nanomaterials . . . . .	9
1.2	Superatom nanoclusters . . . . .	10
1.2.1	Origin of magic number behaviors . . . . .	10
1.2.2	Magic number and superatoms . . . . .	12
1.2.3	Binary nanoclusters . . . . .	13
1.3	The purpose of this thesis . . . . .	14
	References . . . . .	18
<b>2</b>	<b>Experimental Setup</b>	<b>24</b>
2.1	Development of cluster generation system . . . . .	25
2.1.1	Principle of magnetron sputtering . . . . .	26
2.1.2	Quadrupole mass spectrometer . . . . .	27
2.1.3	Scheme of cluster generation and deposition system . . . . .	30
2.1.4	Evaluation of apparatus . . . . .	31
2.2	X-ray Photoelectron spectroscopy . . . . .	34

2.2.1	Photoelectron spectroscopies . . . . .	34
2.2.2	Basic principles . . . . .	35
2.2.3	Photoelectron spectroscopy system . . . . .	36
2.2.4	XPS analysis method . . . . .	39
2.2.4.1	Determination of backgrounds . . . . .	39
2.2.4.2	Origin of XPS peak shapes . . . . .	41
	References . . . . .	43
<b>3</b>	<b>Structure Dependence of Electronic States in Thiolate-Protected Gold Nanoclusters</b>	<b>46</b>
3.1	Introduction . . . . .	47
3.2	Experiment . . . . .	50
3.2.1	Sample preparation . . . . .	50
3.3	Results . . . . .	51
3.3.1	Analyses of core-level XPS spectra . . . . .	51
3.3.2	Analyses of valence-band XPS spectra . . . . .	56
3.4	Conclusions . . . . .	63
	References . . . . .	64
<b>4</b>	<b>Chemical Characterization of an Alkali-like Superatom Consisting of a Ta-encapsulating Si<sub>16</sub> cage</b>	<b>72</b>
4.1	Introduction . . . . .	73
4.2	Experiment . . . . .	76
4.3	Results . . . . .	77

4.3.1	Geometric characterization of Ta@Si <sub>16</sub> deposited on a HOPG . . .	77
4.3.2	Heating effect . . . . .	80
4.3.3	Oxygen exposure . . . . .	83
4.3.4	Valence band structures . . . . .	86
4.4	Conclusions . . . . .	89
	References . . . . .	90
<b>5</b>	<b>Charge Transfer Complexation of Ta-Encapsulating Superatom Ta@Si<sub>16</sub> with C<sub>60</sub></b>	<b>95</b>
5.1	Introduction . . . . .	96
5.2	Experiment . . . . .	98
5.3	Results . . . . .	99
5.3.1	XPS spectra of Ta@Si <sub>16</sub> deposited on a C <sub>60</sub> film . . . . .	99
5.3.2	Heating effect . . . . .	105
5.3.3	Oxygen exposure . . . . .	114
5.4	Conclusions . . . . .	116
	References . . . . .	117
<b>6</b>	<b>Conclusions</b>	<b>123</b>
6.1	Conclusions . . . . .	124
6.2	Outlooks of this research . . . . .	125
	References . . . . .	127
	<b>Appendix: Publications and Presentations</b>	<b>128</b>

## Chapter 1

# General Introduction

## 1.1 Introduction — potentials of nanomaterials

If there were a time machine, what time would you go to? If I had, I would definitely go to the future because I can never imagine the future society in detail, even for the next decade. Perhaps, many amazing gadgets, which seem impossible from our current scientific knowledge, would be invented in the 22nd century. Actually, the technology has been advancing very rapidly beyond our expectation.

In history, great pioneers have opened up a new prospect to overcome the technological limitations. For example, the development of Haber-Bosch process, which is undoubtedly one of the most famous technological innovations, enabled us to immobilize nitrogen atoms and solved the food problem in the early 20th century. In the middle of 20th century, transistors and other semiconductor devices were invented, which brought the large development of computers. Recently, computer science has developed dramatically. Last year, an artificial intelligence defeated a professional player in the game of Go,<sup>[1]</sup> which was considered extremely hard and unachievable for decades. This work will enable us to create a new society model, in which computers or robots do brain works instead of human.

What is common in all the technological innovations is that they were brought by discovering new natural phenomena. Indeed, catalytic activity of iron yielded the development of Haber-Bosch process, the establishment of carrier transport theory led to inventing of semiconductor devices, and the advanced algorithm allowed us to improve the artificial intelligence systems. In other words, if we find and utilize new natural

phenomena, new scientific or technological field will be created.

From these viewpoints, nanomaterials such as nanoparticles, nanosheets, nanorods and so on, have been attracted great attention due to their novel properties. For example, gold nanoparticles have catalytic activities<sup>[2-5]</sup> or magnetic properties<sup>[6-8]</sup> although the bulk gold is an inert metal and does not show chemical reactivities or magnetic properties. It is also remarkable that their properties are strongly dependent on their structures, because of the quantum effects. For instance, the characters of semiconductor nanomaterials can be tuned by their sizes or shapes.<sup>[9-12]</sup> The properties of a graphene are known to depend crucially on its edge structures.<sup>[13-15]</sup> In other words, these facts suggest, that we can find and control the novel properties of nanomaterials if they are constructible in atomic scale from the bottom-up approach. In order to construct a nanomaterial from the bottom-up strategy, suitable building blocks are required.

Recently, nanoclusters, which consist of several to several hundreds of atoms or molecules, are drawing attention for good candidates of the building blocks.<sup>[16-19]</sup> The reason why nanoclusters are so good candidates for utilizing as building blocks will be described in the next section.

## 1.2 Superatom nanoclusters

### 1.2.1 Origin of magic number behaviors

As mentioned above, nanomaterials have unique properties which do not appear in bulk or atoms. In the case of nanoclusters, the properties are more sensitive to their

sizes, even to the number of atoms, mainly due to the two reasons: the geometric and electronic shell structures.

For example, nanoclusters consisting of xenon atoms ( $\text{Xe}_n$ ) have been known to be stable when  $n = 13, 55,$  and  $147$ .<sup>[20,21]</sup> This behavior originates from the factor of geometric structure to minimize the surface energy. At these numbers of atoms, the  $\text{Xe}_n$  cluster can form a close-packed icosahedron structure and satisfy the shell-closing condition. Therefore, an additional xenon atom disfavors to connect with these icosahedral clusters and to break the symmetry. Because of the peculiar stabilities, the  $\text{Xe}_{13}$ ,  $\text{Xe}_{55}$ , and  $\text{Xe}_{147}$  nanoclusters are called as “magic number clusters”. The concept of magic number is one of the crucial keys to understand the properties for nanoclusters.

Magic number behavior is caused not only by the geometric effect, but also by the electronic confinement. Because the electronic states of nanoclusters are discrete, the electronic structure gives another magic number condition, especially for metal nanoclusters.<sup>[22]</sup> Knight *et al.* observed mass spectra of sodium clusters ( $\text{Na}_n$ ) and found the peak steps at  $n = 8, 20, 40, 58,$  and  $92$ ,<sup>[23]</sup> similarly to mass spectral behaviors for the  $\text{Xe}_n$  clusters. They also found the almost same behavior for potassium nanoclusters ( $\text{K}_n$ ) at  $n = 2, 8, 20,$  and  $40$ .<sup>[24]</sup> Altogether, alkali-metal nanoclusters show a different magic number series from the rare-gas nanoclusters at  $n = 13, 55, 147$ .

In the case of metal nanoclusters, valence electrons are delocalized and shared among all the atoms, and therefore the electronic state can be described as a jellium model. The electronic levels in jellium-like potentials were already well-known.<sup>[22]</sup> According to the calculation,  $2, 8, 18, 20, 34, 40, 58, 68, 70\dots$  electrons can satisfy the  $1s, 1p, 1d, 2s, 1f, 2p, 1g, 2d, 3s\dots$  electronic shell closing.<sup>[22,25]</sup> These numbers correspond to the

noted magic number of alkali-metal nanoclusters very well. Therefore, we can conclude that the electronic shell model is useful to understand the magic number behavior and properties of metal nanoclusters.

### 1.2.2 Magic number and superatoms

The concept of magic number is applicable to other nanoclusters and brings us an idea of superatoms. Leuchtner *et al.* evaluated the magic number behavior of aluminum cluster anions ( $\text{Al}_n^-$ ) by observing chemical reaction with oxygen.<sup>[26]</sup> As a result,  $\text{Al}_{13}^-$  and  $\text{Al}_{23}^-$  clusters showed extremely high stability in the range between  $n = 5$  and 24. In addition to the fact that 13 is one of the geometric magic numbers, these clusters satisfy the electron shell closing; the numbers of valence electron in  $\text{Al}_{13}^-$  and  $\text{Al}_{23}^-$  are estimated as  $13 \times 3 + 1 = 40$ , and  $23 \times 3 + 1 = 70$ , respectively, both of which satisfy the magic numbers of the jellium model.<sup>[26]</sup> Furthermore, they also evaluated their properties for cationic conditions, revealing that  $\text{Al}_{13}^+$  and  $\text{Al}_{23}^+$  showed no magic number behaviors, while  $\text{Al}_7^+$  were stable against oxygen because of the jellium shell closings with 20 electrons.<sup>[27]</sup> This experimental result indicates that some clusters prefer a particular charge state.

From the other perspective, these clusters can be regarded as a large atom, so-called “superatom”. That is,  $\text{Al}_{13}$  and  $\text{Al}_{23}$  act as halogen atoms and  $\text{Al}_7$  acts as an alkaline metal atom. As mentioned above, one can switch the reactivities of the superatoms by only changing their charge states, thereby superatom nanoclusters have a great potential to utilize as new building blocks for nanomaterials.<sup>[16, 17, 28, 29]</sup>

### 1.2.3 Binary nanoclusters

In addition to the single component nanoclusters, many magic number clusters consisting of multi elements have been discovered. Metal-encapsulating silicon nanoclusters ( $M@Si_{16}$ , Figure 1.1 left) are one of the most interesting binary nanoclusters.  $M@Si_{16}$

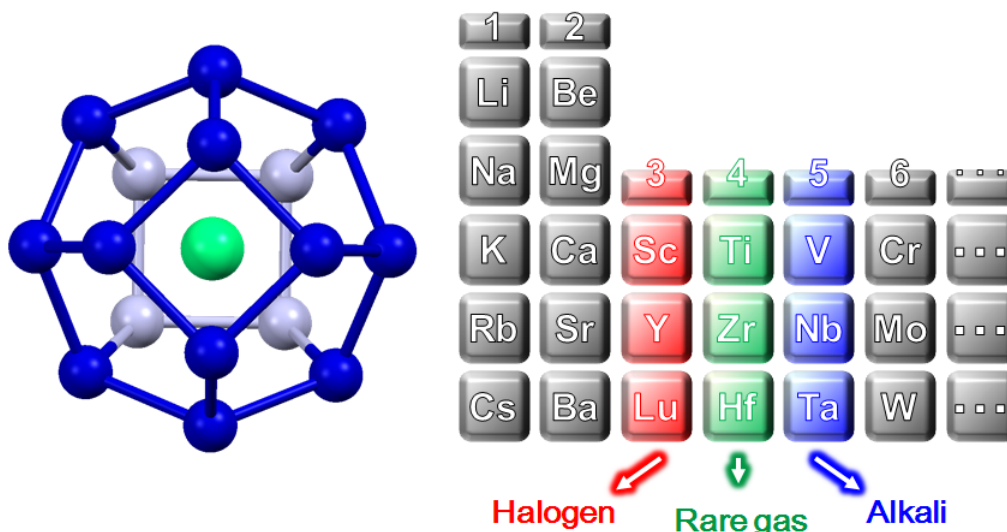


Figure 1.1 (Left) A molecule model of  $Ta@Si_{16}^+$ . Sixteen blue spheres show Si atoms and a central green sphere shows a Ta atom. (Right) Relationship between the superatomic behavior of  $M@Si_{16}$  and the central atom.

nanoclusters were experimentally discovered and demonstrated to have magic number behavior by Koyasu *et al.*<sup>[30,31]</sup>  $M@Si_{16}$  nanoclusters have opened up new approaches for constructing silicon-based nanomaterials because not only they are silicon-based and high symmetric clusters, but also their properties can be optimized by changing the central metal atom. For example,  $M@Si_{16}$  nanoclusters containing a group 4 metal atom exhibit rare-gas-like superatom behaviors because each atom bears four valence electrons, which results in 68 electrons closed-shell structure (Figure 1.1 right).<sup>[30–35]</sup> On

the other hand, group 3 and group 5 metal-encapsulating nanoclusters show halogen- and alkali-like nature, respectively, because the excess or missing electron satisfies the electronic closed-shell structure.<sup>[30, 31, 34]</sup> Because of these properties,  $M@Si_{16}$  nanoclusters have been expected to construct functional hetero-complexes.<sup>[36, 37]</sup>

Ligand-protected metal clusters are also attractive binary nanoclusters because they are stable enough to be synthesized in liquid phase, and of course they also exhibit novel properties. Actually, a series of magic number clusters have been precisely isolated and their geometric structures have been also revealed.<sup>[38–42]</sup> The large scale synthesis of ligand-protected nanoclusters have allowed us to evaluate many properties, such as optical, magnetic, and catalytic ones.<sup>[4, 5, 28, 43, 44]</sup>

As described above, binary nanoclusters can exhibit various properties none of which appear in the single-component nanoclusters due to the versatile combination of components, which opens up a wide outlook for the nanomaterial science.

### 1.3 The purpose of this thesis

The nanoclusters have been expected to be utilized as nanomaterials and their properties have been precisely examined by many experiments in the gas phase. However, there are few successful examples of applying them into actual devices. This gap between the basic science and technology is largely caused by the difficulty of immobilizing clusters without any destruction or aggregation. Because of this difficult problem, the properties, including their geometric and electronic structures, of deposited clusters have been hardly observed, which also limits the advances of nanocluster technology. In

order to advance the nanocluster technology for the nanomaterial applications, it has been investigated that the geometric and electronic structures of deposited nanoclusters using photoelectron spectroscopies, because their electronic properties are crucial to describe the functionality of optical and electric properties.

At first, I focused on three thiolate-protected gold (Au:SR) nanoclusters,  $[\text{Au}_{25}(\text{SR})_{18}]^-$ ,  $\text{Au}_{38}(\text{SR})_{24}$ , and  $\text{Au}_{144}(\text{SR})_{60}$  ( $\text{R}=\text{C}_{12}\text{H}_{25}$ ), because all of which geometric structures were already evaluated in atomic scale.<sup>[38–40, 42]</sup> It is expected that geometrically well-defined clusters enable us to discuss the relationship between geometric and electronic structures in details. The Au:SR nanoclusters were deposited as a monolayer film to a highly oriented pyrolytic graphite (HOPG) surface through Langmuir-Blodgett method in order to avoid the charge up during photoelectron spectroscopies. After producing thin films of nanoclusters, their electronic structures were evaluated by X-ray photoelectron spectroscopy (XPS) and ultraviolet photoelectron spectroscopy (UPS), which are powerful methods to evaluate the electronic structures of surfaces. In this way, I have revealed the relation between the electronic states and geometric structures for these nanoclusters.

As mentioned above, the thiolate-protected gold nanoclusters have been attracted great attention. However, their properties are strongly modified by the interactions caused by core cluster and ligand protection. Therefore, the assembly of “naked” clusters are important for material science, especially for utilizing their superatomic nature. For this reason, I also focused on metal-encapsulating silicon clusters, in particular, tantalum-encapsulating silicon cage clusters,  $\text{Ta}@\text{Si}_{16}$ , because of the novel characteristics described above.

Since “naked” Ta@Si<sub>16</sub> nanoclusters should be more reactive than ligand-protected nanoclusters, their deposition has to be done in vacuum condition. In order to establish the methodology, I developed at first the new deposition system for these nanoclusters, and revealed the physical and chemical characters of deposited nanoclusters by using XPS and UPS.

This thesis is composed of six chapters as follows.

Chapter 2 presents the experimental principles and apparatus of XPS and UPS system. The development and evaluation of cluster generation apparatus were also described.

Chapter 3 describes the XPS investigation for Langmuir-Blodgett films of thiolate-protected gold nanoclusters, of which geometric structures were well-defined, and discussion about the relation between geometric and electronic structures. XPS results from core level were consistent with the geometric structures of clusters. The size- and structure-dependence was clearly found by observation of valence electronic states.

Chapter 4 describes the chemical characterization of Ta@Si<sub>16</sub> cluster, which is one of the metal-encapsulating silicon cage clusters. Ta@Si<sub>16</sub> was generated in gas phase and deposited on a highly oriented pyrolytic graphite (HOPG) surface, and then its chemical states were evaluated by using XPS. The results indicated each silicon and tantalum atom has uniform chemical state, showing Ta@Si<sub>16</sub> maintains its original cage structure after deposition on HOPG. Its chemical stability was also revealed by examining its robustness against oxygen exposure and heating treatment.

Chapter 5 describes the chemical properties of Ta@Si<sub>16</sub> deposited on a C<sub>60</sub> film on

HOPG by XPS and UPS. The results showed that the Ta@Si<sub>16</sub> acts as an alkali-like superatom and forms superatomic complex (Ta@Si<sub>16</sub>)<sup>+</sup>C<sub>60</sub><sup>-</sup> with C<sub>60</sub> via a charge transfer (CT). The results also showed that the superatomic CT complex exhibits highly chemical and thermal robustness.

Finally, in Chapter 6, all the results and the conclusions of this thesis are summarized.

## References

- [1] D. Silver, A. Huang, C. J. Maddison, A. Guez, L. Sifre, G. v. d. Driessche, J. Schrittwieser, I. Antonoglou, V. Panneershelvam, M. Lanctot, S. Dieleman, D. Grewe, J. Nham, N. Kalchbrenner, I. Sutskever, T. Lillicrap, M. Leach, K. Kavukcuoglu, T. Graepel and D. Hassabis. “Mastering the game of Go with deep neural networks and tree search”. *Nature*, **2016**, 529, 484–489.
- [2] M. Haruta. “Catalysis of gold nanoparticles deposited on metal oxides”. *Cattech*, **2002**, 6(3), 102–115.
- [3] M.-C. Daniel and D. Astruc. “Gold nanoparticles: assembly, supramolecular chemistry, quantum-size-related properties, and applications toward biology, catalysis, and nanotechnology”. *Chem. Rev.*, **2004**, 104(1), 293–346.
- [4] T. Tsukuda. “Toward an atomic-level understanding of size-specific properties of protected and stabilized gold clusters”. *Bull. Chem. Soc. Jap.*, **2012**, 85(2), 151–168.
- [5] S. Yamazoe, K. Koyasu and T. Tsukuda. “Nonscalable oxidation catalysis of gold clusters”. *Acc. Chem. Res.*, **2013**, 47(3), 816–824.
- [6] P. Crespo, R. Litrán, T. Rojas, M. Multigner, J. D. I. Fuente, J. Sánchez-López, M. García, A. Hernando, S. Penadés and A. Fernández. “Permanent magnetism, magnetic anisotropy, and hysteresis of thiol-capped gold nanoparticles”. *Phys. Rev. Lett.*, **2004**, 93(8), 087204.
- [7] P. Crespo, R. Litrán, T. Rojas, M. Multigner, J. D. I. Fuente, J. Sánchez-López,

- M. García, A. Hernando, S. Penadés and A. Fernández. “Permanent magnetism, magnetic anisotropy, and hysteresis of thiol-capped gold nanoparticles”. *Phys. Rev. Lett.*, **2004**, 93(8), 087204.
- [8] Y. Negishi, H. Tsunoyama, M. Suzuki, N. Kawamura, M. M. Matsushita, K. Maruyama, T. Sugawara, T. Yokoyama and T. Tsukuda. “X-ray magnetic circular dichroism of size-selected, thiolated gold clusters”. *J. Am. Chem. Soc.*, **2006**, 128(37), 12034–12035.
- [9] A. P. Alivisatos. “Semiconductor clusters, nanocrystals, and quantum dots”. *Science*, **1996**, 271(5251), 933–937.
- [10] Y. Zhou, Z. Zhu, W. Huang, W. Liu, S. Wu, X. Liu, Y. Gao, W. Zhang and Z. Tang. “Optical coupling between chiral biomolecules and semiconductor nanoparticles: size-dependent circular dichroism absorption”. *Angew. Chem., Int. Ed.*, **2011**, 50(48), 11456–11459.
- [11] V. L. Colvin, A. P. Alivisatos and J. G. Tobin. “Valence-band photoemission from a quantum-dot system”. *Phys. Rev. Lett.*, **1991**, 66(21), 2786–2789.
- [12] A. N. Goldstein, C. M. Echer and A. P. Alivisatos. “Melting in semiconductor nanocrystals”. *Science*, **1992**, 256(5062), 1425–1427.
- [13] X. Jia, M. Hofmann, V. Meunier, B. G. Sumpter, J. Campos-Delgado, J. M. Romero-Herrera, H. Son, Y.-P. Hsieh, A. Reina, J. Kong, et al. “Controlled formation of sharp zigzag and armchair edges in graphitic nanoribbons”. *Science*, **2009**, 323(5922), 1701–1705.
- [14] B. Huang, M. Liu, N. Su, J. Wu, W. Duan, B.-l. Gu and F. Liu. “Quantum manifestations of graphene edge stress and edge instability: a first-principles study”.

- Phys. Rev. Lett.*, **2009**, 102, 166404.
- [15] P. Koskinen, S. Malola and H. Häkkinen. “Evidence for graphene edges beyond zigzag and armchair”. *Physical Review B*, **2009**, 80(7), 073401.
- [16] S. N. Khanna and P. Jena. “Assembling crystals from clusters”. *Phys. Rev. Lett.*, **1992**, 69, 1664–1667.
- [17] P. Jena. “Beyond the periodic table of elements: The role of superatoms”. *J. Phys. Chem. Lett.*, **2013**, 4(9), 1432–1442.
- [18] S. A. Claridge, A. Castleman Jr, S. N. Khanna, C. B. Murray, A. Sen and P. S. Weiss. “Cluster-assembled materials”. *Acs Nano*, **2009**, 3(2), 244–255.
- [19] X. Roy, C.-H. Lee, A. C. Crowther, C. L. Schenck, T. Besara, R. A. Lalancette, T. Siegrist, P. W. Stephens, L. E. Brus, P. Kim, et al. “Nanoscale atoms in solid-state chemistry”. *Science*, **2013**, 341(6142), 157–160.
- [20] O. Echt, K. Sattler and E. Recknagel. “Magic numbers for sphere packings: experimental verification in free xenon clusters”. *Phys. Rev. Lett.*, **1981**, 47, 1121–1124.
- [21] W. Miehle, O. Kandler, T. Leisner and O. Echt. “Mass spectrometric evidence for icosahedral structure in large rare gas clusters: Ar, Kr, Xe”. *J. Chem. Phys.*, **1989**, 91(10), 5940.
- [22] W. A. d. Heer. “The physics of simple metal clusters: experimental aspects and simple models”. *Rev. Mod. Phys.*, **1993**, 65, 611–676.
- [23] W. D. Knight, K. Clemenger, W. a. De Heer, W. a. Saunders, M. Y. Chou and M. L. Cohen. “Electronic shell structure and abundances of sodium clusters”. *Phys. Rev. Lett.*, **1984**, 52(24), 2141–2143.
- [24] W. Knight, W. A. d. Heer, K. Clemenger and W. A. Saunders. “Electronic shell

- structure in potassium clusters”. *Solid State Commun.*, **1985**, 53(5), 445–446.
- [25] M. G. Mayer and J. H. D. Jensen. *Elementary theory of nuclear shell structure*. John Wiley & Sons, 1955.
- [26] R. E. Leuchtner, a. C. Harms and a. W. Castleman. “Thermal metal cluster anion reactions: Behavior of aluminum clusters with oxygen”. *J. Chem. Phys.*, **1989**, 91(4), 2753–2754.
- [27] R. Leuchtner, A. Harms and A. Castleman Jr. “Aluminum cluster reactions”. *J. Chem. Phys.*, **1991**, 94(2), 1093–1101.
- [28] H. Yang, Y. Wang, H. Huang, L. Gell, L. Lehtovaara, S. Malola, H. Häkkinen and N. Zheng. “All-thiol-stabilized Ag<sub>44</sub> and Au<sub>12</sub>Ag<sub>32</sub> nanoparticles with single-crystal structures”. *Nat. Commun.*, **2013**, 4.
- [29] D. Bergeron, P. Roach, A. Castleman, N. Jones and S. Khanna. “Al cluster superatoms as halogens in polyhalides and as alkaline earths in iodide salts”. *Science*, **2005**, 307(5707), 231–235.
- [30] K. Koyasu, M. Akutsu, M. Mitsui and A. Nakajima. “Selective formation of MSi<sub>16</sub> (M= Sc, Ti, and V)”. *J. Am. Chem. Soc.*, **2005**, 127(14), 4998–4999.
- [31] K. Koyasu, J. Atobe, M. Akutsu, M. Mitsui and A. Nakajima. “Electronic and geometric stabilities of clusters with transition metal encapsulated by silicon”. *J. Phys. Chem. A*, **2007**, 111(1), 42–49.
- [32] V. Kumar and Y. Kawazoe. “Metal-encapsulated fullerenelike and cubic caged clusters of silicon”. *Phys. Rev. Lett.*, **2001**, 87(4), 045503.
- [33] H. Kawamura, V. Kumar and Y. Kawazoe. “Growth behavior of metal-doped silicon clusters Si<sub>n</sub>M (M= Ti, Zr, Hf; n= 8–16)”. *Phys. Rev. B*, **2005**, 71(7), 075423.

- [34] J. U. Reveles and S. N. Khanna. “Electronic counting rules for the stability of metal-silicon clusters”. *Phys. Rev. B*, **2006**, 74(3), 035435.
- [35] J. Lau, K. Hirsch, P. Klar, A. Langenberg, F. Lofink, R. Richter, J. Rittmann, M. Vogel, V. Zamudio-Bayer, T. Möller, et al. “X-ray spectroscopy reveals high symmetry and electronic shell structure of transition-metal-doped silicon clusters”. *Phys. Rev. A*, **2009**, 79(5), 053201.
- [36] T. Iwasa and A. Nakajima. “Geometric, electronic, and optical properties of a superatomic heterodimer and trimer:  $\text{Sc@Si}_{16}\text{-V@Si}_{16}$  and  $\text{Sc@Si}_{16}\text{-Ti@Si}_{16}\text{-V@Si}_{16}$ ”. *J. Phys. Chem. C*, **2012**, 116(26), 14071–14077.
- [37] H. Cantera-López, L. Balbás and G. Borstel. “First-principles calculations of structural and electronic properties of Ta-doped Si clusters, wires, and bulk systems”. *Phys. Rev. B*, **2011**, 83(7), 075434.
- [38] M. W. Heaven, A. Dass, P. S. White, K. M. Holt and R. W. Murray. “Crystal structure of the gold nanoparticle  $[\text{N}(\text{C}_8\text{H}_{17})_4][\text{Au}_{25}(\text{SCH}_2\text{CH}_2\text{Ph})_{18}]$ ”. *J. Am. Chem. Soc.*, **2008**, 130(12), 3754–3755.
- [39] M. Zhu, C. M. Aikens, F. J. Hollander, G. C. Schatz and R. Jin. “Correlating the crystal structure of a thiol-protected  $\text{Au}_{25}$  cluster and optical properties”. *J. Am. Chem. Soc.*, **2008**, 130(18), 5883–5885.
- [40] H. Qian, W. T. Eckenhoff, Y. Zhu, T. Pintauer and R. Jin. “Total structure determination of thiolate-protected  $\text{Au}_{38}$  nanoparticles”. *J. Am. Chem. Soc.*, **2010**, 132(24), 8280–8281.
- [41] P. D. Jadzinsky, G. Calero, C. J. Ackerson, D. A. Bushnell and R. D. Kornberg. “Structure of a thiol monolayer-protected gold nanoparticle at 1.1 Å resolution”.

*Science*, **2007**, 318(5849), 430–433.

- [42] O. Lopez-Acevedo, J. Akola, R. L. Whetten, H. Gronbeck and H. Haäkkinen. “Structure and bonding in the ubiquitous icosahedral metallic gold cluster  $\text{Au}_{144}(\text{SR})_{60}$ ”. *J. Phys. Chem. C*, **2009**, 113(13), 5035–5038.
- [43] R. Jin. “Quantum sized, thiolate-protected gold nanoclusters”. *Nanoscale*, **2010**, 2(3), 343–362.
- [44] M. Walter, J. Akola, O. Lopez-Acevedo, P. D. Jadzinsky, G. Calero, C. J. Ackerson, R. L. Whetten, H. Grönbeck and H. Häkkinen. “A unified view of ligand-protected gold clusters as superatom complexes”. *Proc. Natl. Acad. Sci.*, **2008**, 105(27), 9157–9162.

## Chapter 2

# Experimental Setup

## 2.1 Development of cluster generation system

In previous studies,  $M@Si_{16}$  nanoclusters were generated by the double laser vaporization method.<sup>[1,2]</sup> The double laser vaporization method is a method of generating clusters composed of two different elements from two independent laser vaporizations. In this method, clusters which contain two metal elements at any mixing ratio can be generated.<sup>[3]</sup> Moreover, it is capable for refractory metals, including molybdenum and tungsten.<sup>[4]</sup> However, laser vaporization is not applicable to engineering procedures such as nanodevice fabrication, mainly because of the limited scalability. In order to fabricate size-selected nanoclusters for nanoapplications, highly intense nanocluster ion sources are required.

Haberland and his co-workers have developed an intensive nanocluster source based on direct-current magnetron sputtering (MSP) method combined with a gas flow cell.<sup>[5]</sup> Compared to the laser vaporization method, the generation of highly intense nanocluster beam has been achieved by the MSP method due to the wide scalable area of the sputtering targets and the high average discharge energy.<sup>[6-8]</sup> In this study, I constructed a new apparatus, which is composed of a cluster synthesis apparatus using MSP method, a quadrupole mass spectrometer, and a deposition chamber. With the newly developed apparatus, nanoclusters can be mass-selected and deposited onto a substrate with mass spectrometry, and transferred to a photoelectron spectroscopy (PES) system under the ultrahigh vacuum.

### 2.1.1 Principle of magnetron sputtering

The basic mechanism of cluster generation by MSP is as follows: accelerated argon cations ( $\text{Ar}^+$ ) sputter a cathode target disk, and the vaporized atoms and ions from eroded materials are cooled by helium ( $\text{He}$ ) gas, and transported along with their aggregation. The scheme is shown as Figure 2.1. In order to sputter the target efficiently,

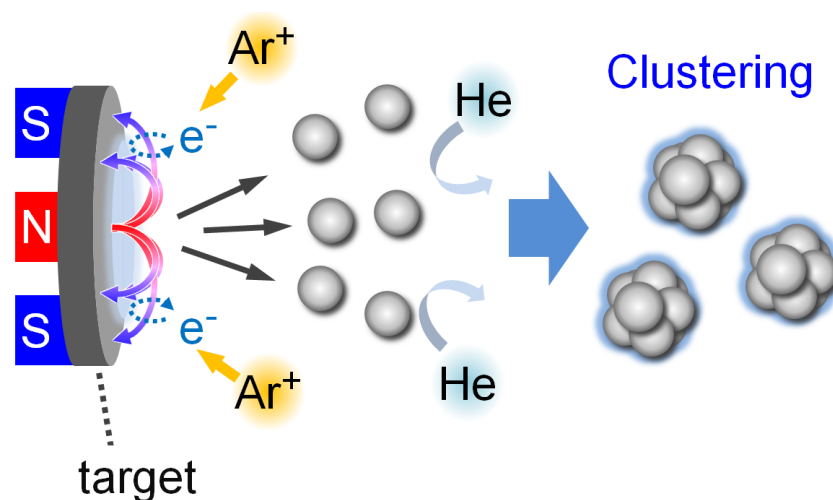


Figure 2.1 The schematic diagram of MSP. In the left figure, the situation of sputtering is drawn. The magnetic field lines trap electrons, which attract the  $\text{Ar}^+$  ions. The right figure shows the image of synthesized nanoclusters.

a permanent magnet is set behind the sputtered target disk. The magnetic field lines from the center to edge of disk trap the electrons near the sputtering target, and the electrons attract the  $\text{Ar}^+$  ions.

## 2.1.2

A qu  
shown

ides as  
plied a

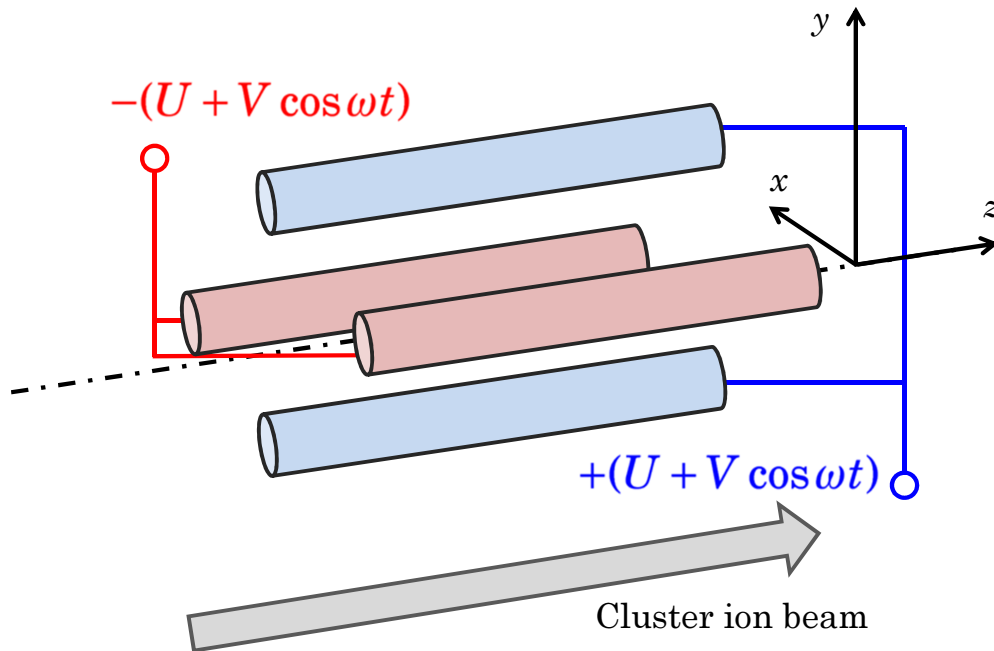


Figure 2.2 Structure of a Q-mass filter. The  $z$  axis shows the direction of cluster ions.

combination of radio frequency voltage with a direct-current offset voltage. When the voltage  $\pm(U + V \cos(\omega t))$  is applied for each pair, an electric field appears inside the poles and cluster ions feel the Coulombic potential.

### 図 四重極電極の構造

As shown in Figure 2.2, the  $z$ -axis is defined along the center line of the four electrodes. When a cluster ion is introduced into the Q-mass, it feels the Coulomb potential from the normal direction of  $z$ -axis. With controlling the  $U$ ,  $V$ , and  $\omega$ , only a particular ion which has specific ratio between mass and charge ( $m/z$ ) can pass through the filter. If the ion passes through the filter, it can be detected and counted as ion current.

Since the electric field  $\varphi$  is equal value in all direction,  $\varphi$  can be described as

$$\varphi = \varphi_0(\lambda x^2 + \sigma y^2 + \gamma z^2). \quad (2.1)$$

This  $\varphi$  satisfies

$$\Delta\varphi = \left( \frac{\partial^2\varphi}{\partial x^2} + \frac{\partial^2\varphi}{\partial y^2} + \frac{\partial^2\varphi}{\partial z^2} \right) = 0 \quad (2.2)$$

because of the Poisson's rule. From equations 2.1 and 2.2,

$$\lambda + \sigma + \gamma = 0 \quad (2.3)$$

is acquired. Considering that the length of electrodes are long enough than their intervals, the electric field of  $z$ -axis can be approximated to be constant, resulting in  $\gamma = 0$  and  $\lambda = -\sigma$ . By letting  $\lambda$  be  $\frac{1}{r_0^2}$ , equation 2.2 can be described as

$$\varphi = \frac{\varphi_0}{r_0^2}(x^2 - y^2) \quad (2.4)$$

and, if the given voltage of rods are  $\pm(U + V \cos(\omega t))$ ,  $\varphi$  can be represented as

$$\varphi = \frac{U + V \cos(\omega t)}{r_0^2}(x^2 - y^2), \quad (2.5)$$

and the electric field in every axis is evaluated as

$$E_x = -\frac{\partial\varphi}{\partial x} = -(U + V \cos \omega t) \frac{2x}{r_0^2}, \quad (2.6)$$

$$E_y = -\frac{\partial\varphi}{\partial y} = (U + V \cos \omega t) \frac{2y}{r_0^2}, \quad (2.7)$$

$$E_z = -\frac{\partial\varphi}{\partial z} = 0. \quad (2.8)$$

Therefore, the equations of motion for the particle, of which mass and charge  $e$  are  $e$  respectively, derived as

$$m \frac{d^2x}{dt^2} = -2e(U + V \cos \omega t) \frac{x}{r_0^2}, \quad (2.9)$$

$$m \frac{d^2y}{dt^2} = 2e(U + V \cos \omega t) \frac{y}{r_0^2}, \quad (2.10)$$

$$m \frac{d^2 z}{dt^2} = 0. \quad (2.11)$$

These results reveal that the particle vibrates periodically in the  $x$ - and  $y$ - direction while it doesn't feel any forces in the  $z$ - direction. By substituting each parameter for  $\xi$ ,  $a$ ,  $q$  with the relationship of

$$\xi = \frac{\omega t}{2}, \quad a = \frac{8eU}{mr_0^2\omega^2}, \quad q = \frac{4eV}{mr_0^2\omega^2}, \quad (2.12)$$

the equations 2.6 and 2.7 are given as differential equations,

$$\frac{d^2 x}{dt^2} + (a + 2q \cos 2\xi)x = 0 \quad (2.13)$$

$$\frac{d^2 y}{dt^2} - (a + 2q \cos 2\xi)y = 0 \quad (2.14)$$

where these formulas have been known as Mathieu equation. These formulas were already solved as follows:<sup>[9]</sup>

$$x = \alpha' e^{\mu\xi} \sum_{-\infty}^{+\infty} C_{2s} e^{2is\xi} + \alpha'' e^{-\mu\xi} \sum_{-\infty}^{+\infty} C_{2s} e^{-2is\xi}, \quad (2.15)$$

$$y = -\alpha' e^{\mu\xi} \sum_{-\infty}^{+\infty} C_{2s} e^{2is\xi} - \alpha'' e^{-\mu\xi} \sum_{-\infty}^{+\infty} C_{2s} e^{-2is\xi}. \quad (2.16)$$

These result means that an ion can pass through if  $x$  is limited even when the time is too large ( $\xi \rightarrow \infty, x \rightarrow \pm\infty$ ), otherwise the amplitude becomes larger and ion beam diverges.

Here  $\beta$  is used for these equations where  $\mu = i\beta$ , they are represented as

$$x = \alpha' \sum_{-\infty}^{+\infty} C_{2s} \cos(2s + \beta)\xi + \alpha'' \sum_{-\infty}^{+\infty} C_{2s} \sin(2s + \beta)\xi, \quad (2.17)$$

$$y = -\alpha' \sum_{-\infty}^{+\infty} C_{2s} \cos(2s + \beta)\xi - \alpha'' \sum_{-\infty}^{+\infty} C_{2s} \sin(2s + \beta)\xi. \quad (2.18)$$

These re

imaginary

number.

For th

. With

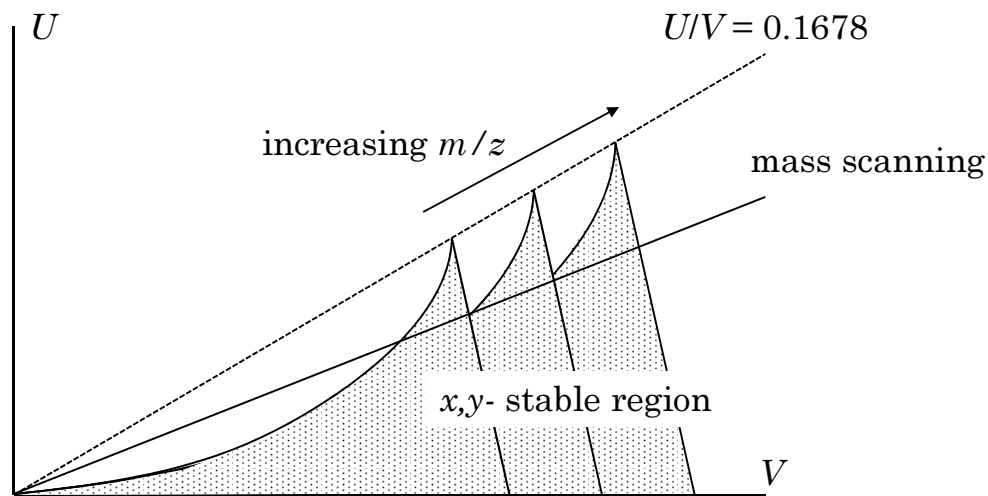


Figure 2.3  $x, y$ -stable region of Q-mass spectrometer.

increasing the ratio  $U/V$ , **四重極質量分析計の安定線図** therefore each ion is mass-selected well. In particular, the mass scanning line goes along the peak tops of stable regions when  $U/V = 0.1678$ , that is, if you increase  $U$  and  $V$  with maintaining the ratio  $U/V = 0.1678$ , the highest mass resolution will be achieved.<sup>[10]</sup>

### 2.1.3 Scheme of cluster generation and deposition system

An overall schematic diagram of the nanocluster generation and deposition system is shown in Figure 2.4. At first, nanoclusters can be generated in the MSP source. Then, the synthesized nanoclusters are guided by octopole ion guide (OPIG), which is a powerful tool for guiding ion beams by operating the r.f.-field.<sup>[11]</sup> After that, cations or anions are selectively deflected by an ion bender and precisely mass-selected through a

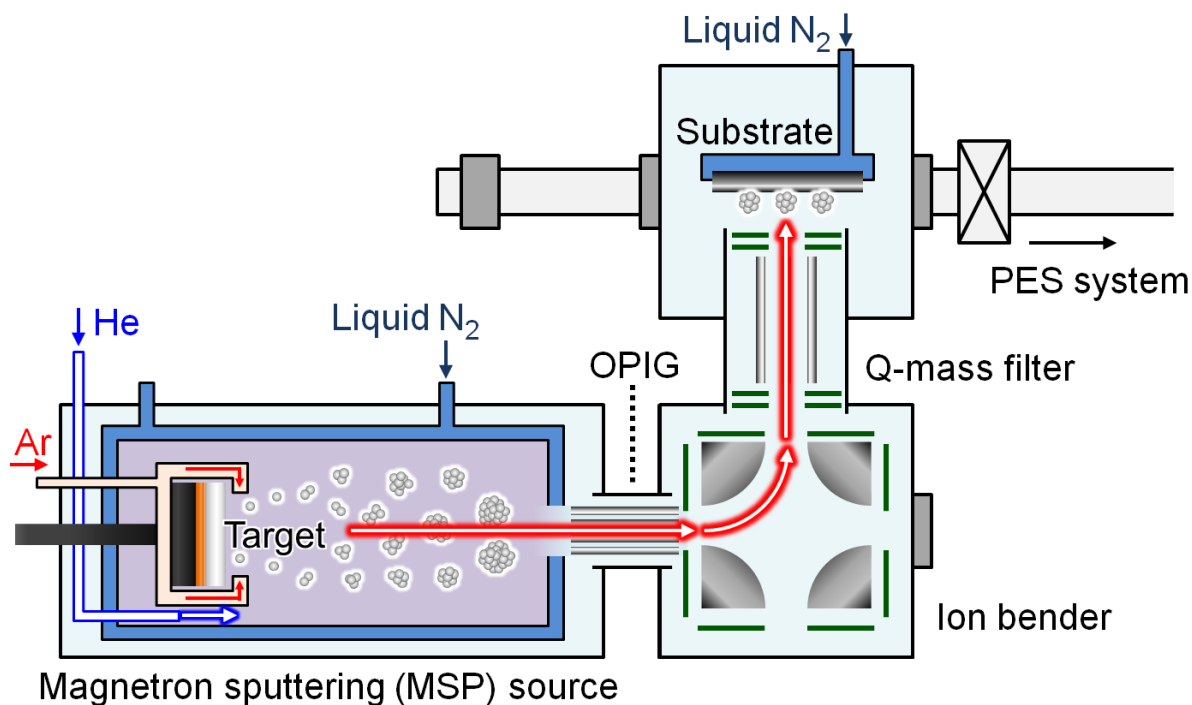


Figure 2.4 The schematic diagram of cluster generation system.

Q-mass filter, finally deposited onto a substrate with controlling their deposition energies by tuning the bias voltage of the substrate.

#### 2.1.4 Evaluation of apparatus

With this apparatus, silver nanocluster cations ( $\text{Ag}_n^+$ ) were generated, where the mass spectrum is shown in Figure 2.5. As shown,  $\text{Ag}_n^+$  can be generated up to the high mass regions ( $m/z$  of thousands) and mass-selected with an atomic level. Note that the scale bar in the spectrum shows the ion intensity of 100 pA, which corresponds with about  $2.3 \times 10^{12}$  clusters/h. If one nanocluster occupies a deposited area of  $1 \text{ nm}^2$ , nanocluster deposition with the average ion current of 400 pA for 1 hour brings the total deposition area of  $10 \text{ mm}^2$ , which is enough for spectroscopic analysis. In this way, the ability of nanocluster generation was evaluated by  $\text{Ag}_n^+$  nanocluster generation.

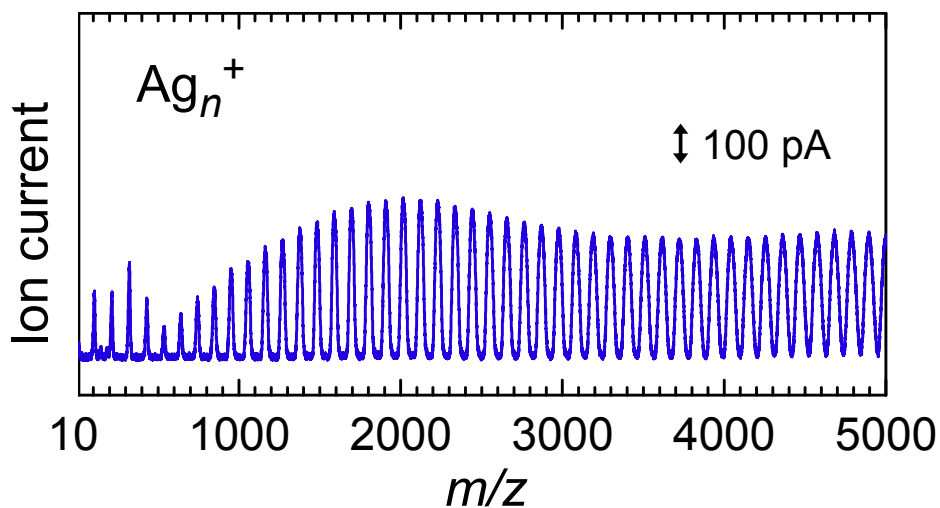


Figure 2.5 Typical mass spectrum for silver nanocluster cations ( $\text{Ag}_n^+$ ) obtained by the developed apparatus.

## Example of cluster generation

5

### Mass spectrum of $\text{TaSi}_n^+$ clusters

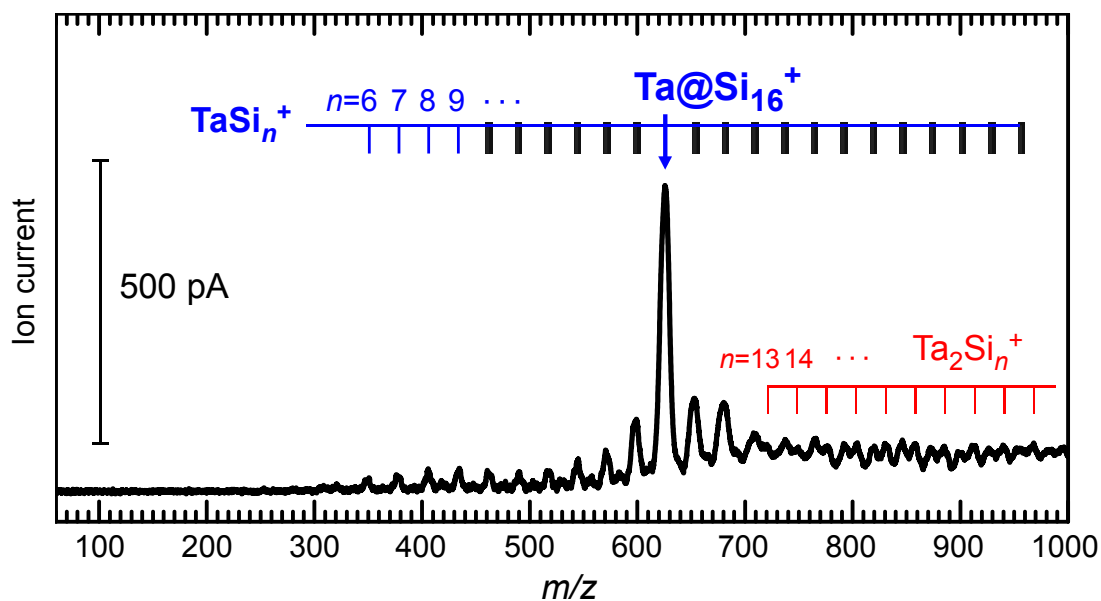


Figure 2.6 Mass spectrum for tantalum-silicon binary nanocluster cations ( $\text{TaSi}_n^+$ ).

can see, all nanoclusters were separated with an atomic level, and  $\text{Ta@Si}_{16}^+$  showed extremely strong peak in the mass spectrum. This result demonstrated not only that the developed apparatus has enough resolution for mass-selection, but also that  $\text{Ta@Si}_{16}$  nanoclusters show a magic number behavior even when synthesized by the MSP method. Note that

Interest  
 condition

## TaSi<sub>3</sub><sup>-</sup> generation

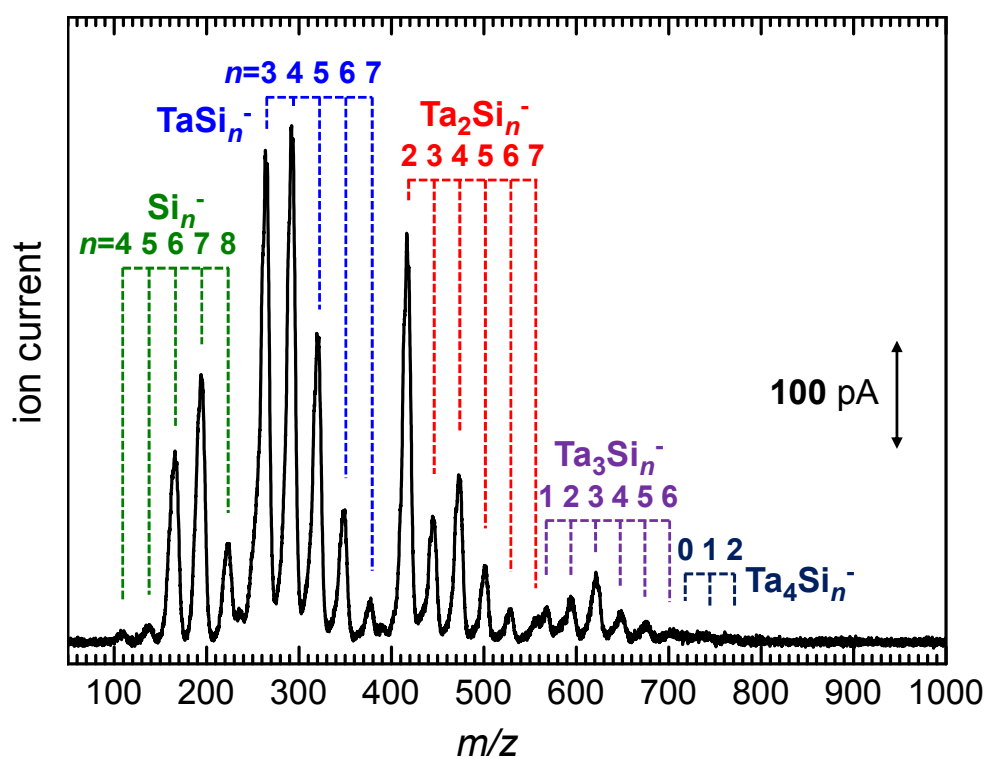


Figure 2.7 Mass spectrum for tantalum-silicon binary nanocluster anions ( $\text{TaSi}_n^-$ ).

experimental result also demonstrate that  $\text{Ta@Si}_{16}$  prefers a cationic condition.

Whether the nanocluster were deposited without destruction or not was also evaluated by spectroscopic methods. Details are described in Chapter 4.

## 2.2 X-ray Photoelectron spectroscopy

### 2.2.1 Photoelectron spectroscopies

When the light is irradiated to material, an electron can absorb the photon energy and emit to the outer side, if the energy is large enough to escape the Coulombic potential barrier. The emitted electron is called as a “photoelectron”. Photoelectron spectroscopies (PESs) are experimental methods to evaluate electronic structures of materials by measuring the kinetic energy and intensity distribution of the photoelectrons. In the PES studies, various excitation lights are available, depending on research purposes. In this study, X-ray ( $\text{MgK}\alpha$ , 1253.6 eV) and vacuum ultraviolet light ( $\text{HeI}\alpha$ , 21.22 eV) were mainly used. The photon energy of X-ray is large enough to put the electrons out from core levels so that X-ray photoelectron spectroscopy (XPS) is useful for core level photoemission. On the other hand, ultraviolet photoelectron spectroscopy (UPS) is a powerful method to detect the electronic structure of valence band. In particular, UPS results are very sensitive to the surface because the kinetic energy of photoelectrons in UPS is about several tens of eV, giving the small escape depth.<sup>[12,13]</sup> This relationship between the energy of photoelectrons and the escape depth has been known to be described as so-called “universal curve”.<sup>[12,13]</sup> In detail, experimental principles of XPS are described below.

## 2.2.2 Basic

As mentioned

level. Figure 2.8

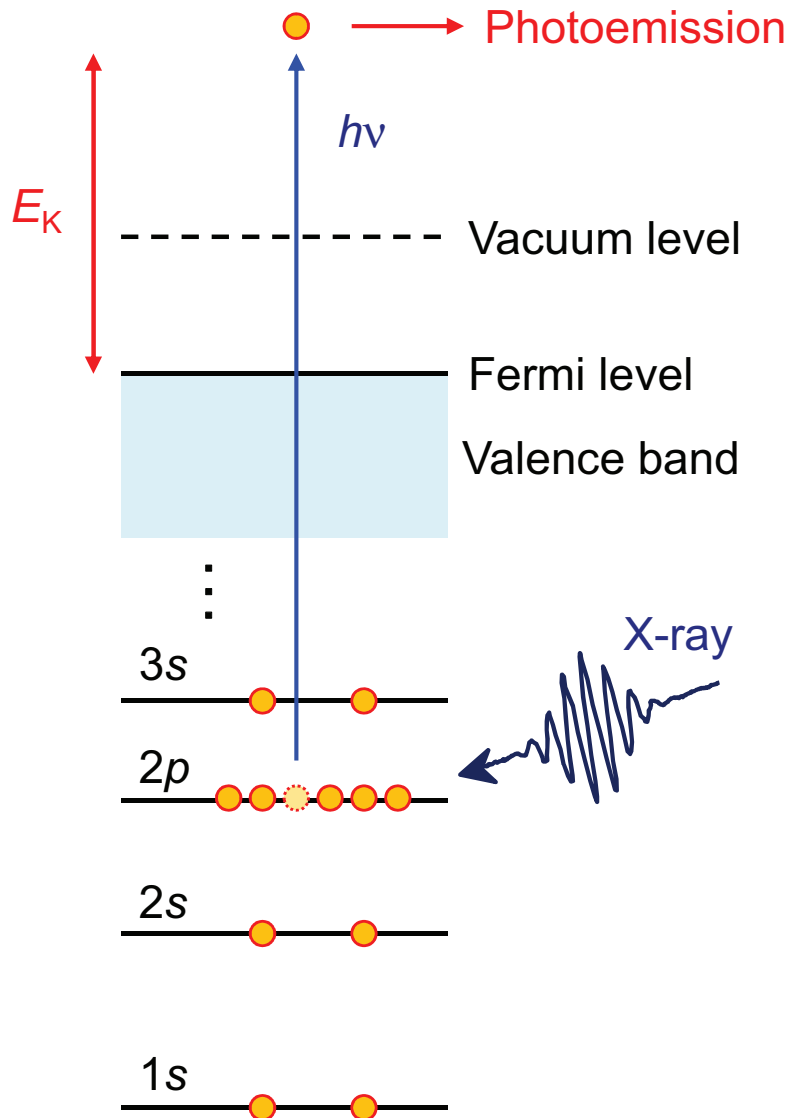


Figure 2.8 Mechanism of photoemission caused by X-ray irradiation. As an example, a photoemission from 2p core level is shown.

relationship between binding energy of an electron from Fermi level ( $E_B$ ) and kinetic

energy ( $E_K$ ) of photoelectron is given by

$$E_B = h\nu - E_K \quad (2.19)$$

where  $h\nu$  is the photon energy. Because the  $E_B$  is dependent on elements and core levels, XPS is often used for elemental analysis. That is, XPS peak positions represent the kinds of elements and the intensity ratio represents chemical composition. From this viewpoint, XPS is also called as Electron Spectroscopy for Chemical Analysis (ESCA).

Moreover, XPS measurements allow us to evaluate the chemical state information because the binding energy of core level also reflects on local chemical environments.<sup>[14–18]</sup> Basically, the binding energy shifts toward deeper when an atom is oxidized because the electrons feel the Coulomb potential from the atomic nucleus strongly,<sup>[15–17]</sup> although there are some exceptions.<sup>[19,20]</sup>

### 2.2.3 Photoelectron spectroscopy system

The photoelectron spectroscopy system is shown as Figure 2.9. The system is connected to the cluster generation system, so the measuring sample can be transferred under vacuum. In this study, photoelectrons were detected using a hemispherical electron analyzer (VG SCIENTA, R-3000) for XPS and UPS photoemission angles of  $45^\circ$  and  $0^\circ$  with respect to the surface normal, respectively.

The schematic diagram of the hemispherical analyzer is shown in Figure 2.10. The hemispherical analyzer consists of two hemispheres, the inner one and outer one. When a voltage  $V$  is applied between these hemispheres, the electric field  $\epsilon$  is generated and

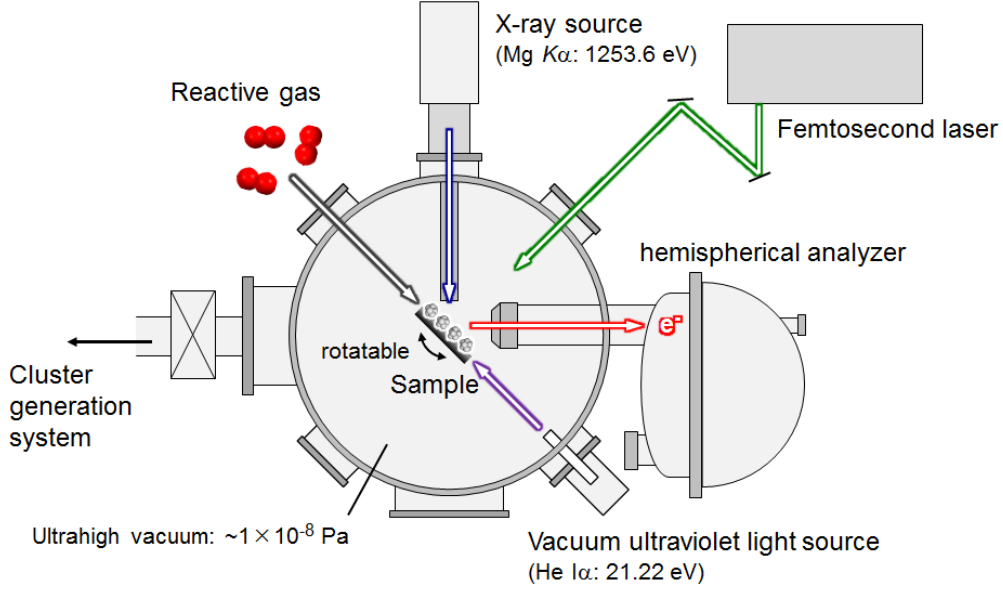


Figure 2.9 Schematic image of the apparatus for photoelectron spectroscopy.

described as

$$\epsilon = \frac{VR_1R_2}{R_0^2(R_2 - R_1)} \quad (2.20)$$

where  $R_1$  and  $R_2$  represents the radius of inner and outer hemisphere respectively, and  $R_0$  represent the average of  $R_1$  and  $R_2$  ( $= (R_1 + R_2)/2$ ). If the kinetic energy of photoelectrons is  $E_p$ , which is defined as

$$e\epsilon = \frac{2E_p}{R_0}, \quad (2.21)$$

the centrifugal force balances the Coulomb attraction, hence the electron can pass through the analyzer and be detected (by a CCD camera, in this apparatus). This value  $E_p$  is called as pass energy, and from the equation 2.20 and 2.21,  $E_p$  is given as the equation 2.22.

$$E_p = \frac{eV}{\left(\frac{R_2}{R_1} - \frac{R_1}{R_2}\right)} \quad (2.22)$$

In actual experiment, there is a slit width of entrance  $w$  and angle dispersion of

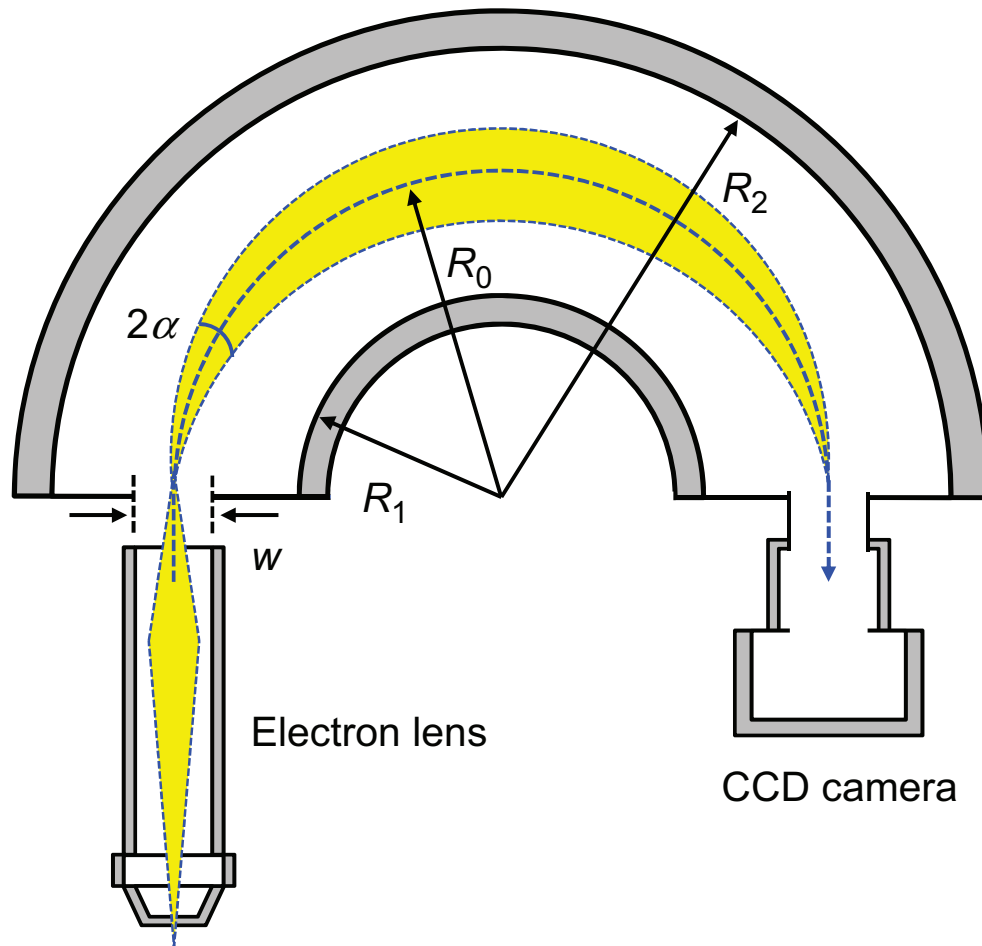


Figure 2.10 Sectional view of a hemispherical analyzer.

photoemission 図 2.10 半球型アナライザーの概略図 as shown in Figure 2.10 producing the distribution of detective photoelectron energies. The distribution becomes prominent when the ratio between  $w$  and  $R_0$  is large, therefore the resolution of hemispherical analyzer  $\Delta E$  is described as the equation 2.23.

$$\Delta E = \frac{w}{2R_0} E_p \quad (2.23)$$

As shown above, the resolution  $\Delta E$  depends on the pass energy  $E_p$ , which is determined by the voltage between two hemispheres,  $V$ . For this reason, the voltage  $V$  has to be fixed to be constant during XPS measurements. In order to detect various

energies of electrons, therefore, the electron lens is set before entrance of analyzer and photoelectrons can be decelerated by the lens.

## 2.2.4 XPS analysis method

For accurate discussion, precise XPS analysis is required. In particular, the peak deconvolution and area estimation must be determined objectively. In this part, I describe how to treat and evaluate the XPS results.

### 2.2.4.1 Determination of backgrounds

Subtraction of a background from spectrum is principal but difficult problem.<sup>[21]</sup> In order to estimate the background component precisely, a famous hypothesis was supposed by Shirley in 1972.<sup>[22]</sup> That is, the backgrounds was occurred by inelastic electron scatterings of which numbers are proportional to peak intensity. Recently, this method of background determination for XPS has been widely adopted.

As a simple example, imagine that there are two peaks,  $\alpha$  and  $\beta$  in a XPS spectrum, having no peak widths (Figure 2.11). According to the Shirley's model, the performed background  $l_3$  can be separated to two components;  $l_1$  and  $l_2$ , which are produced by inelastic electron scatterings derived from peak  $\alpha$  and  $\beta$ , respectively. Note that the height of each background component is proportional to the intensity of corresponding peak. Considering that an actual XPS peak has some peak widths such as schematically drawn in Figure 2.12, background estimation is not so simple but the basic idea is same.

In the Figure 2.12, a background intensity at position  $x$  ( $B(x)$ ) is proportional to

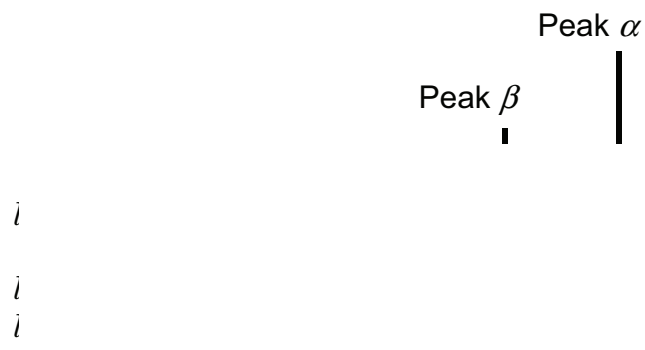


Figure 2.11 Sche

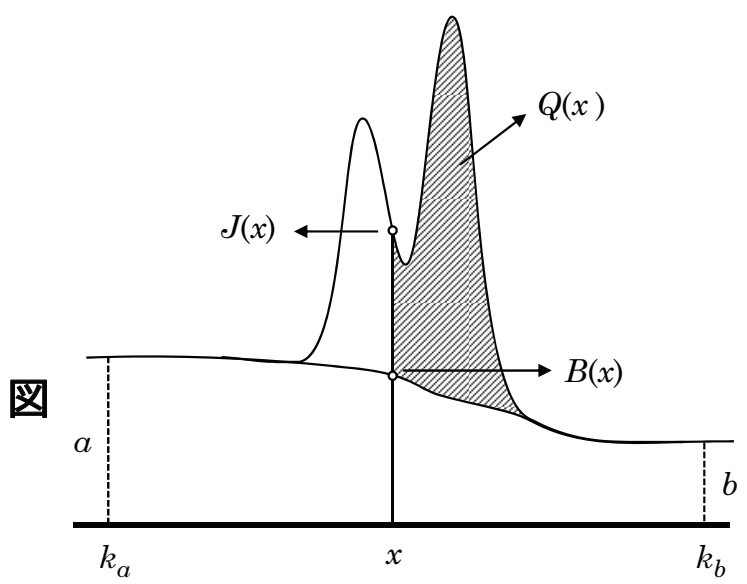


Figure 2.12 Scheme of a Shirley background determination.  $J(x)$ ,  $B(x)$ ,  $Q(x)$  shows the photoemission intensity, the background intensity at the position of  $x$ , and the peak area between  $k_b$  and  $x$ , respectively.

法の考え方

the peak area between the position of  $x$  and  $k_b$ , described as  $Q(x)$ . Because the  $B(x)$  converges on  $a$  and  $b$  at  $x = k_a$  and  $k_b$  respectively,  $B(x)$  can be represented as equation 2.24.

$$B(x) = \frac{(a - b) Q(x)}{\int_x^{k_b} [J(t) - B(t)] dt} + b \quad (2.24)$$

In XPS analysis, the backgrounds were determined by calculation based on this Shirley's model.

#### 2.2.4.2 Origin of XPS peak shapes

In addition to the estimation of background, the peak broadness must be accurately determined as well. As mentioned at section 2.2.3, the peak broadening due to the resolution of hemispherical analyzer are inevitable in principle. Furthermore, MgK $\alpha$  X-ray has a half width of 0.65 eV,<sup>[23]</sup> which also broadens the original peak and form a Gaussian shape.

Besides, extremely short lifetime of core hole brings the peak energy distributions due to the uncertainty principle. If there are no more interactions, the peak broads in accordance with the Lorentzian function. However, if a density of electrons near Fermi level is high, many valence electrons are excited during the photoemission process, resulting in a peak shoulder at the higher binding energy region.

This effect was evaluated and formulated by Doniach and Sunjic as

$$Y(E) = \frac{\Gamma(1 - \alpha) \cos \left\{ \frac{\pi\alpha}{2} + (1 - \alpha) \tan^{-1} \frac{E - E_0}{\gamma} \right\}}{\{(E - E_0)^2 + \gamma^2\}} \quad (2.25)$$

where  $Y(E)$  is a photoelectron yield function-spectral line shape,  $\Gamma$  is a gamma function,  $E_0$  is a center of peak position,  $\gamma$  is a natural width of peak, and  $\alpha$  is a singularity

index.<sup>[24]</sup>

In this study, the convolution integral of Gaussian function and the Doniach-Sunjik function was used for each XPS analysis.

## References

- [1] K. Koyasu, M. Akutsu, M. Mitsui and A. Nakajima. “Selective Formation of  $MSi_{16}$  (M= Sc, Ti, and V)”. *J. Am. Chem. Soc.*, **2005**, 127(14), 4998–4999.
- [2] K. Koyasu, J. Atobe, M. Akutsu, M. Mitsui and A. Nakajima. “Electronic and geometric stabilities of clusters with transition metal encapsulated by silicon”. *J. Phys. Chem. A*, **2007**, 111(1), 42–49.
- [3] S. Nonose, Y. Sone, K. Onodera, S. Sudo and K. Kaya. “Structure and reactivity of bimetallic cobalt-vanadium ( $Co_nV_m$ ) clusters”. *J. Phys. Chem.*, **1990**, 94(7), 2744–2746.
- [4] J. Hopkins, P. Langridge-Smith, M. D. Morse and R. Smalley. “Supersonic metal cluster beams of refractory metals: Spectral investigations of ultracold  $Mo_2$ ”. *J. Chem. Phys.*, **1983**, 78(4), 1627–1637.
- [5] H. Haberland and M. Karrais. “Thin films from energetic cluster impact: A feasibility study”. *J. Vac. Sci. Technol., A*, **1992**, 10(1992), 3266–3271.
- [6] V. N. Popok, I. Barke, E. E. Campbell and K.-H. Meiwes-Broer. “Cluster–surface interaction: From soft landing to implantation”. *Surf. Sci. Rep.*, **2011**, 66(10), 347–377.
- [7] H. Tsunoyama, C. Zhang, H. Akatsuka, H. Sekiya, T. Nagase and A. Nakajima. “Development of high-flux ion source for size-selected nanocluster ions based on high-power impulse magnetron sputtering”. *Chem. Lett.*, **2013**, 42(8), 857–859.
- [8] C. Zhang, H. Tsunoyama, H. Akatsuka, H. Sekiya, T. Nagase and A. Nakajima.

- “Advanced nanocluster ion source based on high-power impulse magnetron sputtering and time-resolved measurements of nanocluster formation”. *J. Phys. Chem. A*, **2013**, 117(40), 10211–10217.
- [9] W. Paul, H. Reinhard and U. Von Zahn. “Das elektrische massenfilter als massenspektrometer und isotopentrenner”. *Z. Phys.*, **1958**, 152(2), 143–182.
- [10] S. Wright, S. O’Prey, R. R. Syms, G. Hong and A. S. Holmes. “Microfabricated quadrupole mass spectrometer with a Brubaker prefilter”. *J. Microelectromech. Syst.*, **2010**, 19(2), 325–337.
- [11] P. Tosi, G. Fontana, S. Longano and D. Bassi. “Transport of an ion beam through an octopole guide operating in the RF-only mode”. *Int. J. Mass Spectrom. Ion Process.*, **1989**, 93(1), 95–105.
- [12] M. P. Seah and W. A. Dench. “Quantitative electron spectroscopy of surfaces: A standard data base for electron inelastic mean free paths in solids”. *Surf. Interface Anal.*, **1979**, 1(1), 2–11.
- [13] W. A. Clay, Z. Liu, W. Yang, J. D. Fabbri, J. E. Dahl, R. M. K. Carlson, Y. Sun, P. R. Schreiner, A. A. Fokin, B. A. Tkachenko, N. A. Fokina, P. A. Pianetta, N. Melosh and Z. X. Shen. “Origin of the monochromatic photoemission peak in diamondoid monolayers”. *Nano Lett.*, **2009**, 9(1), 57–61.
- [14] J. Hedman, Y. Baer, A. Berndtsson, M. Klasson, G. Leonhardt, R. Nilsson and C. Nordling. “Influence of doping on the electron spectrum of silicon”. *J. Electron Spectrosc. Relat. Phenom.*, **1972**, 1(1), 101–104.
- [15] G. Rangelov and T. Fauster. “Thermally-induced evolution of codeposited Co-Si layers on Si(100) surfaces”. *Surf. Sci.*, **1996**, 365(2), 403–410.

- [16] M. Gomoyunova, I. Pronin, D. Malygin, N. Gall, D. Vyalikh and S. Molodtsov. “Photoemission study of cobalt interaction with the oxidized Si(100)  $2 \times 1$  surface”. *Surf. Sci.*, **2006**, 600(12), 2449–2456.
- [17] D. M. Riffe and G. Wertheim. “Ta(110) surface and subsurface core-level shifts and  $4f_{7/2}$  line shapes”. *Phys. Rev. B*, **1993**, 47(11), 6672.
- [18] J. S. Brinen, S. Greenhouse and L. Pinatti. “ESCA and SIMS studies of plasma treatments of intraocular lenses”. *Surf. Interface Anal.*, **1991**, 17(2), 63–70.
- [19] O. Wertheim. “Anomalous chemical shifts: barium compounds”. *J. Electron Spectrosc. Relat. Phenom.*, **1984**, 34(3), 309–312.
- [20] K. Kim, T. O’leary and N. Winograd. “X-ray photoelectron spectra of lead oxides”. *Anal. Chem.*, **1973**, 45(13), 2214–2218.
- [21] M. Repoux. “Comparison of background removal methods for XPS”. *Surf. Interface Anal.*, **1992**, 18(7), 567–570.
- [22] D. A. Shirley. “High-resolution X-ray photoemission spectrum of the valence bands of gold”. *Phys. Rev. B*, **1972**, 5, 4709–4714.
- [23] F. Wuilleumier and M. O. Krause. “Photoionization of neon between 100 and 2000 eV: Single and multiple processes, angular distributions, and subshell cross sections”. *Phys. Rev. A*, **1974**, 10, 242–258.
- [24] S. Doniach and M. Sunjic. “Many-electron singularity in X-ray photoemission and X-ray line spectra from metals”. *J. Phys. C*, **1970**, 3(2), 285.

## Chapter 3

# Structure Dependence of Electronic States in Thiolate-Protected Gold Nanoclusters

## 3.1 Introduction

As mentioned in Chapter 1, metal nanoparticles (NPs) and nanoclusters have attracted a great deal of attention because of their potential application to magnetic, optical, electronic devices, and catalysts.<sup>[1,2]</sup> One of the most important issues of these nanoclusters is that their properties are controllable not only by their constituent elements, but also by their sizes. Among the metal NPs, gold NPs protected by thioliates have been studied most extensively with regard to synthesis methods, size-dependent properties, and functionalization,<sup>[3-8]</sup> which are relevant to thiolate-protected gold surfaces and interfaces, including self-assembled monolayers of organic molecules on gold.<sup>[9,10]</sup> Thiolate-protected Au (Au:SR) NPs have been successfully synthesized with high monodispersity,<sup>[11-21]</sup> and various of their properties, such as optical,<sup>[11-15]</sup> electronic,<sup>[11,16]</sup> magnetic,<sup>[17-19]</sup> and catalytic,<sup>[20,21]</sup> have been investigated, none of which appear in the bulk form. In order to reveal the origin of the size specific properties, it is crucial to investigate the size dependence of their electronic structures. Although systematic studies of the electronic structure of Au:SR NPs have revealed a size dependence of the charge state of the Au atoms, the valence band energy levels, and the hole density in the Au 5*d* band,<sup>[22-28]</sup> the origin of these size-specific properties is still under debate. For example, Au 4*f* levels of Au NPs was known to shift higher binding energy, but the origin was unknown. Zhang and Sham observed the Au 4*f* with changing the size of alkanethiolate-capped Au NPs and insisted that the energy shift is occurred by increasing d-holes.<sup>[27]</sup> On the other hand, Tanaka *et al.* observed

the same phenomenon with changing the size of dodecanethiolate-passivated Au NPs and insisted that it is occurred by final state effect,<sup>[24]</sup> which is likely ascribable to a poor understanding of the correlation between their geometric and electronic structures. Recently, Au:SR nanoclusters with a well-defined “size” and “chemical composition” have been successfully synthesized, and as a result, a series of stable nanoclusters, so-called magicnumber clusters have been isolated.<sup>[5–8]</sup> Among them, the geometric structures of  $[\text{Au}_{25}(\text{SR})_{18}]^-$ ,  $\text{Au}_{38}(\text{SR})_{24}$ , and  $\text{Au}_{102}(\text{SR})_{44}$  nanoclusters were identified by single-crystal X-ray diffraction (XRD).<sup>[29–32]</sup>  $\text{Au}_{144}(\text{SR})_{60}$  is the second most common of the magic-number Au:SR nanoclusters. Although the single-crystal XRD analysis of  $\text{Au}_{144}(\text{SR})_{60}$  has not been reported yet, there are extensive discussions about its geometric structure based on the combination of various experiments and quantum chemical calculations.<sup>[33]</sup> These achievements enable us to establish a correlation between electronic and geometric structures at the atomic level. Indeed, some of the properties of Au:SR nanoclusters, such as their magneto-optical and photoluminescence properties, have been reconsidered based on this geometric model.<sup>[5]</sup> In this study, by using X-ray photoelectron spectroscopy (XPS), we have studied the electronic states of three different sizes of Au:SR nanoclusters having well-established geometric structures,  $[\text{Au}_{25}(\text{SR})_{18}]^-$ ,<sup>[29,30]</sup>  $\text{Au}_{38}(\text{SR})_{24}$ ,<sup>[31]</sup> and  $\text{Au}_{144}(\text{SR})_{60}$ <sup>[33]</sup> ( $\text{R} = \text{C}_{12}\text{H}_{25}$ ), each with a single atomic composition [see structural models in Figure 3.1(a)–(c)]; their size and structure dependences are discussed from the atomic viewpoint.

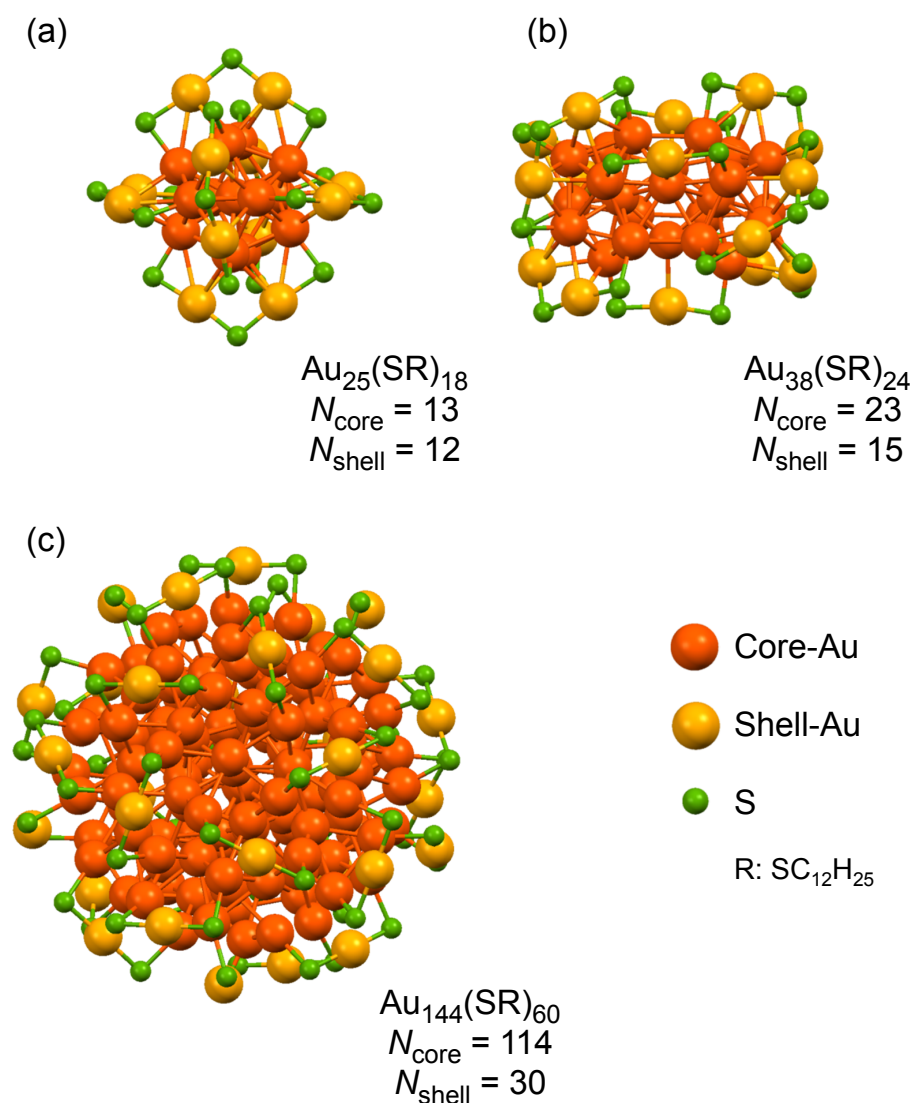


Figure 3.1 Geometric structures of (a)  $\text{Au}_{25}(\text{SR})_{18}$ , (b)  $\text{Au}_{38}(\text{SR})_{24}$ , and (c)  $\text{Au}_{144}(\text{SR})_{60}$  ( $\text{R}=\text{C}_{12}\text{H}_{25}$ ). Red, orange, and green spheres represent core-Au, shell-Au, and S atoms, respectively. The alkyl chain groups (R) are omitted for simplicity. The number of core-Au and shell-Au are shown as  $N_{\text{core}}$  and  $N_{\text{shell}}$ , respectively. Reprinted with permission from {Ohta, T.; Shibuta, M.; Tsunoyama, H.; Negishi, Y.; Eguchi, T.; Nakajima, A. Size and structure dependence of electronic states in thiolate-protected gold nanoclusters of  $\text{Au}_{25}(\text{SR})_{18}$ ,  $\text{Au}_{38}(\text{SR})_{24}$ , and  $\text{Au}_{144}(\text{SR})_{60}$ }. Copyright {2013} American Chemical Society.

### 図 チオラート保護金クラスターの構造

## 3.2 Experiment

### 3.2.1 Sample preparation

The apparatus and principle of photoelectron spectroscopy were described in Chapter 2. In this section, the experimental manipulation of sample preparation is explained.

Single composition Au:SR nanoclusters of  $[\text{Au}_{25}(\text{SR})_{18}]^-$  (abbreviated as  $\text{Au}_{25}(\text{SR})_{18}$ ),  $\text{Au}_{38}(\text{SR})_{24}$ , and  $\text{Au}_{144}(\text{SR})_{60}$  have been synthesized by the Brust method<sup>[34]</sup> with a little modification. Isolation of each nanocluster was confirmed by matrix assisted laser desorption/ionization mass spectrometry and ultraviolet/visible absorption spectroscopy based on the reported spectra.<sup>[35,36]</sup> The Langmuir-Blodgett (LB) method has been employed to fabricate uniform and monolayer films of Au:SR nanoclusters on a highly oriented pyrolytic graphite (HOPG) substrate which is suitable to analyze the valence band structures of the Au nanoclusters supported on the substrate, because the density of state of HOPG near the Fermi level is very low and nearly constant. The HOPG substrate was cleaved in air and heated up to 700 K in ultra high vacuum (UHV) for 20 h before use. To prepare LB films, nanoclusters of  $\text{Au}_{25}(\text{SR})_{18}$ ,  $\text{Au}_{38}(\text{SR})_{24}$ , and  $\text{Au}_{144}(\text{SR})_{60}$  were dissolved in 56  $\mu\text{M}$  dichloromethane, 20  $\mu\text{M}$  chloroform, and 25  $\mu\text{M}$  chloroform, respectively. These solutions were carefully spread onto ultrapure water in a trough with subsequent evaporation of solvent and compression of the nanocluster into a monolayer film (USI Corp., FSD-50). The cleaned HOPG substrate was carefully contacted to the monolayer film of nanoclusters at a surface pressure of 10 mN/m and immediately introduced into an UHV chamber through a load lock. All XPS measure-

ments were performed under UHV condition with a base pressure of  $<2 \times 10^{-8}$  Pa. The X-ray source using the Mg  $K\alpha$  line ( $h\nu = 1253.6$  eV) was irradiated on the sample at an incident angle of  $45^\circ$ . Photoelectrons emitted at  $45^\circ$  from the surface normal were collected by a hemispherical electron analyzer (VG Scienta, R-3000). The samples were well connected to ground to avoid a sample charging as a result of electron emission during X-ray irradiation. It was carefully verified that there were no effects of X-ray irradiation on the XPS spectra for all samples.

## 3.3 Results

### 3.3.1 Analyses of core-level XPS spectra

At first, Au  $4f$  XPS spectra were measured and shown in Figure 3.2. For reference, the XPS spectrum of Au(111) clean surface was also measured and shown at the top of the Figure 3.2. With decreasing the cluster size, the Au  $4f$  peak shifted toward the higher binding-energy and broadened relative to that of Au(111).

In order to reveal this spectral difference, the peak parameter of Au  $4f$  was firstly evaluated by the XPS analysis of Au(111) based on previous X-ray photoemission studies.<sup>[24,25,37]</sup> At first, a Shirley background was evaluated and subtracted from the spectra before analysis, and the Au(111) spectrum was deconvoluted into two components, the bulk Au atoms (solid lines) and the surface Au atoms (broken lines) with an energy separation of 0.28 eV. Every peak component was described by convolution of a Doniach-Sunjic line shape with a Gaussian to represent the instrumental energy broadening ( $\Gamma_G$ ). The Doniach-Sunjic line shape is characterized by a Lorentzian ( $\Gamma_L$ ),

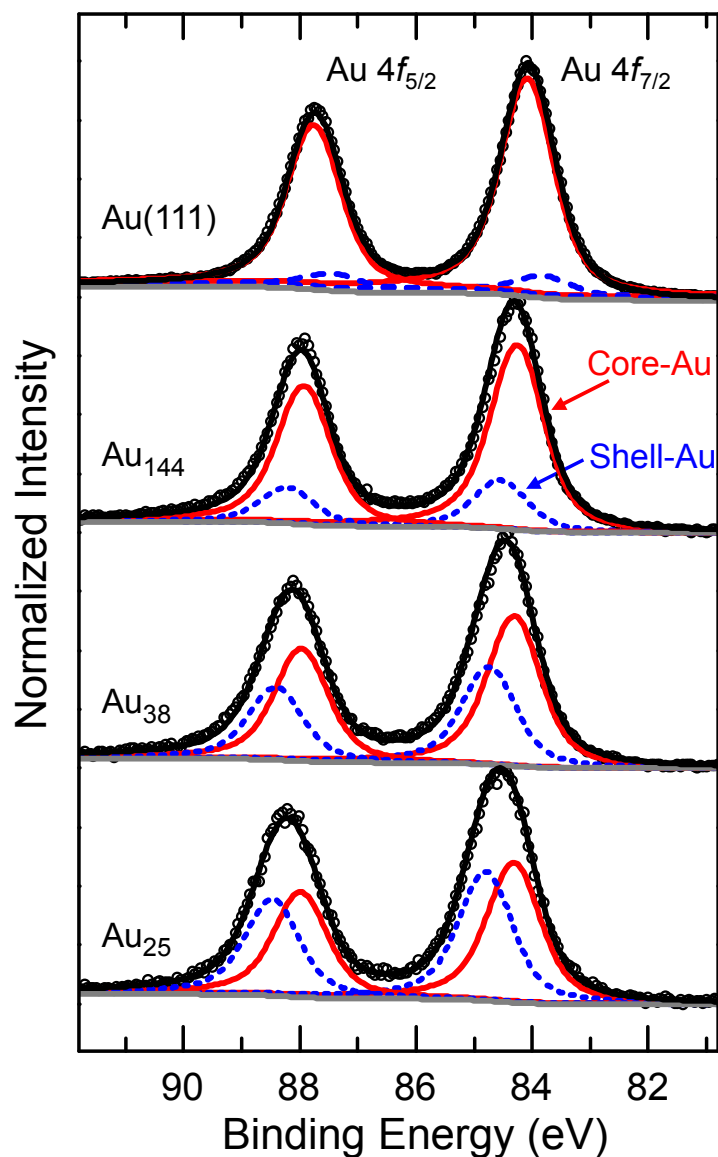


Figure 3.2 Au 4f XPS for the three nanoclusters. Black circles show the original XPS data. Solid- and dotted-lines in the spectra represent the components derived from core-Au and shell-Au, respectively. The Au 4f spectrum of Au(111) clean surface is also shown as a reference, in which solid- and broken-lines also represent the bulk- and surface-components, respectively. Reprinted with permission from {Ohta, T.; Shibuta, M.; Tsunoyama, H.; Negishi, Y.; Eguchi, T.; Nakajima, A. Size and structure dependence of electronic states in thiolate-protected gold nanoclusters of  $\text{Au}_{25}(\text{SR})_{18}$ ,  $\text{Au}_{38}(\text{SR})_{24}$ , and  $\text{Au}_{144}(\text{SR})_{60}$ }. Copyright {2013} American Chemical Society.

which occurs from the short lifetime of excited state, and the singularity index ( $\alpha$ ). From the peak analysis,  $\Gamma_G$ ,  $\Gamma_L$ , and  $\alpha$  of Au 4*f* spectrum have been evaluated to be 0.75 eV, 0.56 eV, and 0.02, respectively. The separation due to the spin-orbit splitting peaks of Au4*f*<sub>7/2</sub> and Au4*f*<sub>5/2</sub> was found to be 3.67 eV with a branching ratio of 4:3. Based on these results, the XPS analysis of the Au:SR nanoclusters was performed.

Because the core-Au and shell-Au should have different chemical environments,<sup>[24,25]</sup> it is reasonable to deconvolute the XPS spectra of Au:SR nanoclusters into two components originating from core- and shell-Au atoms. As shown in Figure 3.1, Au<sub>25</sub>(SR)<sub>18</sub>, Au<sub>38</sub>(SR)<sub>24</sub>, and Au<sub>144</sub>(SR)<sub>60</sub> have a common motif and consist of two components; bulk-like Au core and molecular-like shell layer of  $-\text{S}(\text{R})-\text{Au}-\text{S}(\text{R})-$ <sub>*n*</sub> oligomers with different length (*n* = 1 and 2). After deconvolution has been performed by changing the energy position of the core- and shell-Au components using the  $\Gamma_G$ ,  $\Gamma_L$ , and  $\alpha$  values determined by Au(111), the Au 4*f* spectra of the Au:SR nanoclusters have been separated clearly into two components as shown in Figure 3.2, in which the solid- and dotted-lines represent the photoemission from core- and shell-Au atoms, respectively. Note that the intensity ratio between core- and shell-Au was fixed to the value of  $N_{\text{core}}$  and  $N_{\text{shell}}$ , which is estimated from the counted number of core- and shell-Au atoms, as shown in Figure 3.1. On the other hand, all of the S 2*p* spectra, which is shown in Figure 3.3, can be fitted well by considering only a single component with a common peak width ( $\Gamma_G = 0.75$  eV and  $\Gamma_L = 0.58$  eV), energy separation (1.20 eV) and branching ratio (2:1). The results also support that the deposited nanoclusters maintain their original structures in the LB films without no oxidization or desorption of ligands. The obtained parameters of XPS analysis are listed in Table 3.1. One can think that photoemission

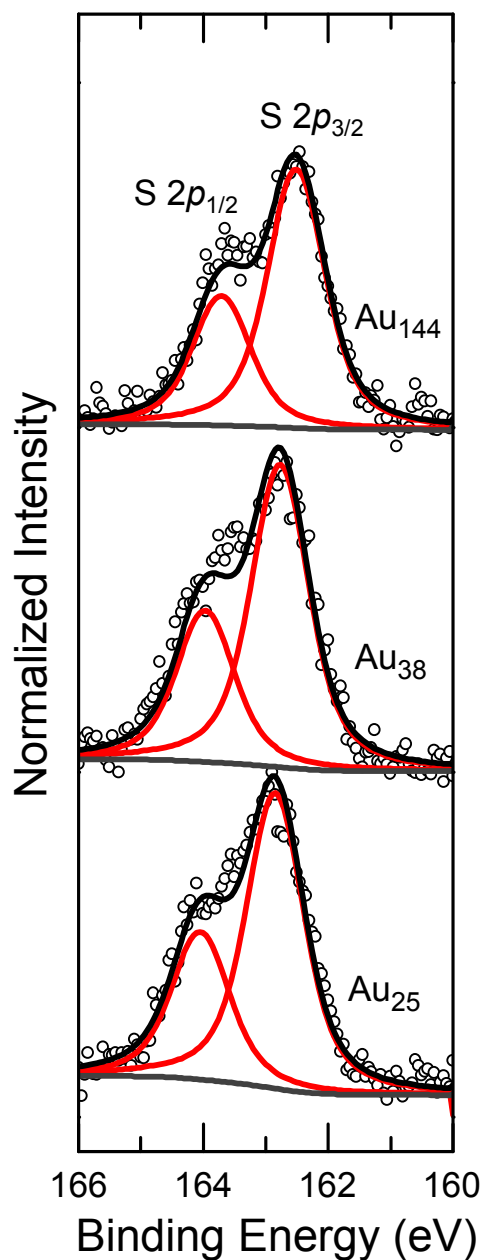


Figure 3.3 S 2p XPS for the three nanoclusters. Black circles show the original XPS data. **図** チオラート保護金クラスターの付近のスペクトル The red solid lines in the spectra represent the component derived from S 2p<sub>3/2</sub> and S 2p<sub>1/2</sub>, respectively. Reprinted with permission from {Ohta, T.; Shibuta, M.; Tsunoyama, H.; Negishi, Y.; Eguchi, T.; Nakajima, A. Size and structure dependence of electronic states in thiolate-protected gold nanoclusters of Au<sub>25</sub>(SR)<sub>18</sub>, Au<sub>38</sub>(SR)<sub>24</sub>, and Au<sub>144</sub>(SR)<sub>60</sub>}. Copyright {2013} American Chemical Society.

from core-Au must be further divided into two species: the one is from surface of core-Au atoms which have a connection with one sulfur atom, and the other one is from the central core-Au atoms which don't connect with any sulfur atoms. Strictly speaking, these Au atoms should appear as different peaks. However, all XPS peaks were already well-fitted although the core-Au was regarded as a single component. This means that the difference between two types of core-Au is too small to be evaluated quantitatively by this experimental setup.

Table 3.1 Energy positions of Au  $4f_{7/2}$  and S  $2p_{3/2}$  determined by the peak analysis

	$N_{\text{shell}}/N_{\text{core}}$	Au $4f_{7/2(\text{core})}$ (eV)	Au $4f_{7/2(\text{shell})}$ (eV)	$\Delta 4f$ (eV)	S $2p$ (eV)
Au(111)		84.08			
Au <sub>144</sub> (SR) <sub>60</sub>	0.263	84.25	84.52	0.27	162.5
Au <sub>38</sub> (SR) <sub>24</sub>	0.652	84.30	84.73	0.43	162.8
Au <sub>25</sub> (SR) <sub>18</sub>	0.923	84.30	84.79	0.49	162.9

The fitting result for Au  $4f$  spectra shows that the shell-Au component has a larger binding energy about 0.5 eV than that of the core-Au, which is consistent with previous studies on monodispersed Au NPs.<sup>[23–25]</sup> This result suggests that the surrounding thiolate sulfur atoms more effectively extract electrons from shell-Au atoms rather than from core-Au atoms. Moreover, on reducing the cluster size, the energy positions of both core- and shell-Au components in the Au  $4f$  spectra shift toward the high binding energy side relative to that of the bulk Au(111). A similar tendency of energy shift to the higher binding energy is seen in the S  $2p$  spectra. If the energy shift is caused by the electron transfer from Au to S, Au  $4f$  and S  $2p$  spectra should shift in the opposite

directions each other. Therefore, the observed energy shift is considered to be mainly attributed to the effect of a core hole left to a nanocluster immediately after photoemission, so-called the final-state effect.<sup>[38,39]</sup> When a photoelectron is emitted by the excitation light, the photohole left behind in the nanoclusters within the time scale of the photoemission process lowers the kinetic energy of the photoelectron through the Coulomb interaction, which results in the apparent energy shift to higher binding energy. The final-state effect would play a significant role in the present Au:SR nanoclusters supported on the substrates because of the weak interaction between the nanoclusters and the substrates through the thiolate molecules, and become more spectacular for smaller clusters, as shown in the present result. This effect makes it difficult to discuss the size dependence of the absolute chemical shift both in Au and S atoms.

### 3.3.2 Analyses of valence-band XPS spectra

Now, we can evaluate that the Au:SR nanoclusters maintain their geometric structures in the LB film on an HOPG surface. Then, their valence electronic states have been evaluated. It is remarkable that photoelectrons from Au can be derived from a kind of buried surface beneath the alkyl chain layer, because Au atoms of thiolate-protected gold nanoclusters are surrounded by long alkyl chains. In general, the kinetic energies of photoelectrons in the UPS measurements are several tens of eV, which is around the minimum point of the universal curve;<sup>[40,41]</sup> the probe depth of the UPS measurements is too short to provide proper information on valence electronic states. In contrast to UPS, XPS can probe electronic states of the Au atoms because photoelectrons are emitted with the kinetic energy of over several hundreds of eV; the photoelectrons from

buried su

Figure

and the  $A$

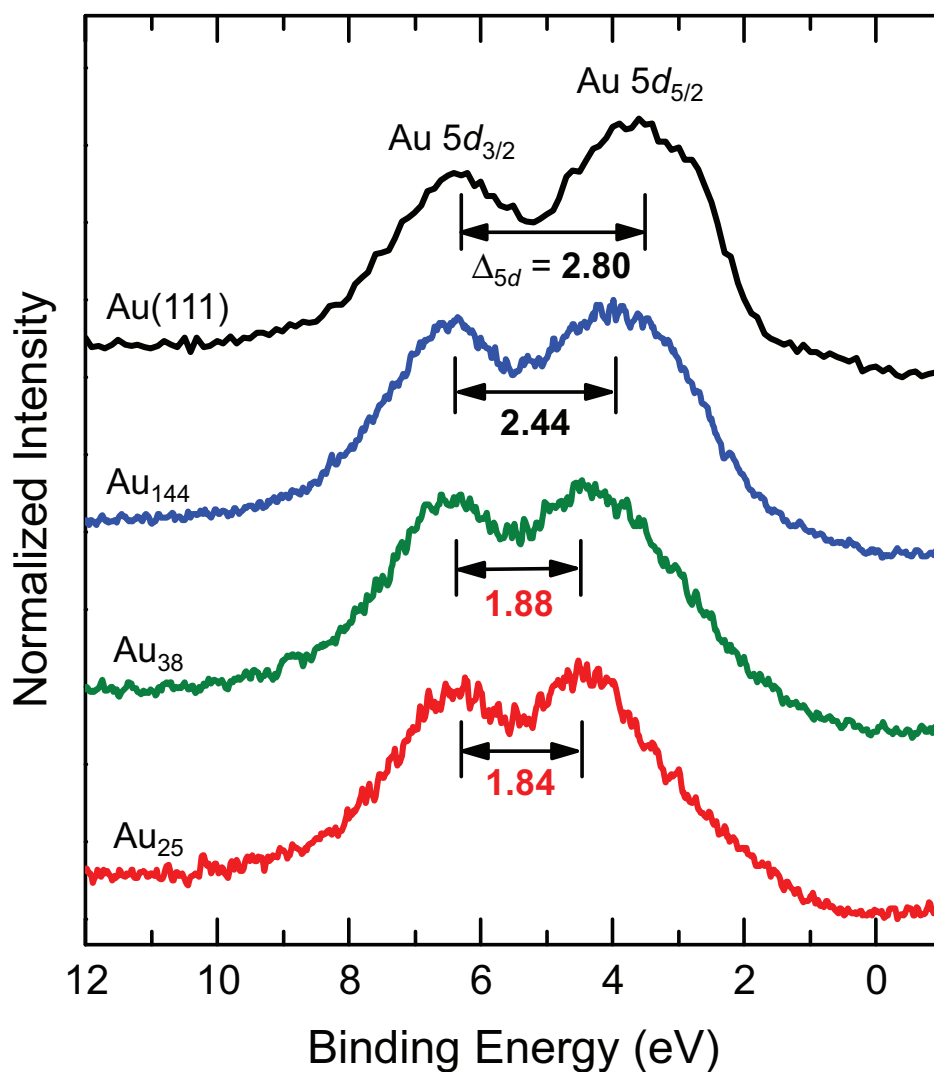


Figure 3.4 Au 5d XPS of the three nanoclusters and Au(111) clean surface. Apparent spin-orbit splitting widths ( $\Delta_{5d}$ ) as marked are also shown. Reprinted with permission from {Ohta, T.; Shibuya, N.; Sato, Y.; Nishiyama, H.; Nishii, Y.; Eguchi, T.; Nakajima, A. Size and structure dependence of electronic states in thiolate-protected gold nanoclusters of Au<sub>25</sub>(SR)<sub>18</sub>, Au<sub>38</sub>(SR)<sub>24</sub>, and Au<sub>144</sub>(SR)<sub>60</sub>}. Copyright {2013} American Chemical Society.

図 3.4 Au(111) 表面と Au<sub>144</sub>, Au<sub>38</sub>, Au<sub>25</sub> ナノクラスターの Au 5d XPS 測定結果。Au(111) 表面の Au 5d XPS 測定結果は黒線、Au<sub>144</sub> ナノクラスターの Au 5d XPS 測定結果は青線、Au<sub>38</sub> ナノクラスターの Au 5d XPS 測定結果は緑線、Au<sub>25</sub> ナノクラスターの Au 5d XPS 測定結果は赤線である。Au(111) 表面の Au 5d XPS 測定結果の Au 5d<sub>3/2</sub> と Au 5d<sub>5/2</sub> のピーク間のエネルギー差は  $\Delta_{5d} = 2.80$  eV、Au<sub>144</sub> ナノクラスターの Au 5d XPS 測定結果の Au 5d<sub>3/2</sub> と Au 5d<sub>5/2</sub> のピーク間のエネルギー差は 2.44 eV、Au<sub>38</sub> ナノクラスターの Au 5d XPS 測定結果の Au 5d<sub>3/2</sub> と Au 5d<sub>5/2</sub> のピーク間のエネルギー差は 1.88 eV、Au<sub>25</sub> ナノクラスターの Au 5d XPS 測定結果の Au 5d<sub>3/2</sub> と Au 5d<sub>5/2</sub> のピーク間のエネルギー差は 1.84 eV である。

els split by a spin-orbit interaction are clearly visible in all spectra, and the apparent spin-orbit splitting width  $\Delta_{5d}$  decreased on reducing the cluster size, which exhibits a similar tendency to that reported for monodispersed Au nanoparticles.<sup>[23–27]</sup> Size dependent electronic properties of monodispersed Au nanoparticles have been studied by changing the mean diameter in the range from 1.6 to 5.2 nm,<sup>[24–27]</sup> while the size of the nanoclusters in this study are smaller; about 1.6, 1.3, and 1.0 nm for Au<sub>144</sub>(SR)<sub>60</sub>, Au<sub>38</sub>(SR)<sub>24</sub>, and Au<sub>25</sub>(SR)<sub>18</sub>, respectively.<sup>[42]</sup> MacDonald and co-workers have studied the size-dependent nature of bonding in these three Au:SR nanoclusters from the X-ray absorption near-edge structure (XANES) analysis, and also reported about the comparison between the valence band XPS for bulk Au and Au<sub>144</sub>(SR)<sub>60</sub> but not that for Au<sub>38</sub>(SR)<sub>24</sub> and Au<sub>25</sub>(SR)<sub>18</sub>.<sup>[23]</sup> As can be seen in Figure 3.4, the  $\Delta_{5d}$  of the Au<sub>144</sub>(SR)<sub>60</sub> and Au<sub>38</sub>(SR)<sub>24</sub> show the systematic narrowing of  $\Delta_{5d}$  as expected from their smaller size with comparing to the bulk, however the  $\Delta_{5d}$  of Au<sub>25</sub>(SR)<sub>18</sub> is very close to that of Au<sub>38</sub>(SR)<sub>24</sub>, although the number of Au atoms and the sizes of clusters are different. It has been established that the Au *d*-bandwidth and apparent spin-orbit splitting become narrower as the coordination number (CN) of the nearest Au atom decreases.<sup>[43,44]</sup> In the previous reports for Au nanoparticles, the CNs were estimated from the size of the nanoparticles using an equation proposed by Pirkkalainen and Serimaa,<sup>[45]</sup> although the CN depends on the geometric structure, not on the size. Since here single-composition nanoclusters having well-established geometric structures have been used as samples,<sup>[29,31,33]</sup> it is possible to determine the average coordination number (ACN) based on their geometric structures as shown in Figure 3.5. The ACN is obtained by weighting the CN of each nonequivalent atom of the clusters by the number of atoms

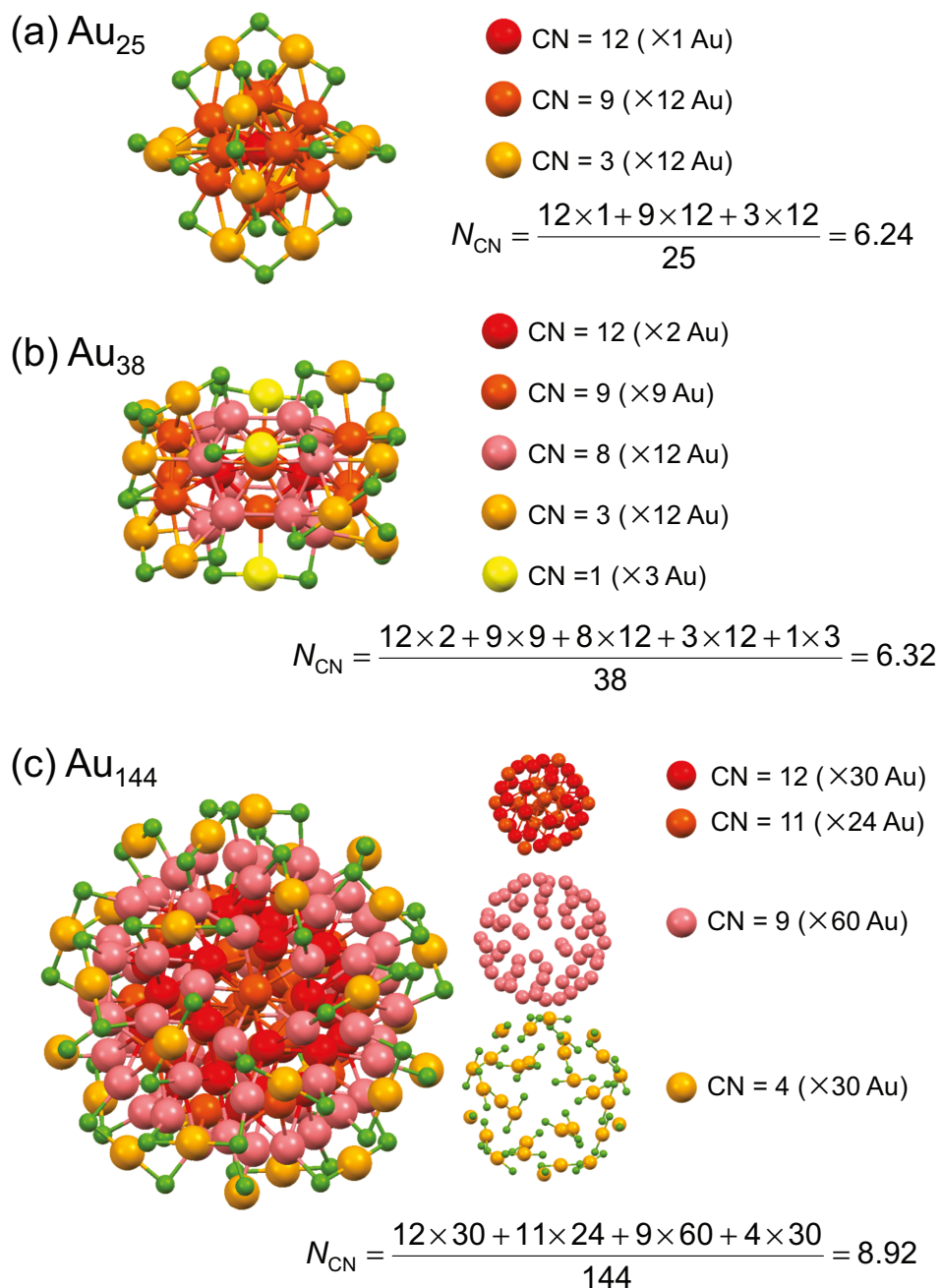


Figure 3.5 図 3.5 平均配位数とその求め方  
 Calculations of average coordination number for (a) Au<sub>25</sub>(SR)<sub>18</sub>, (b) Au<sub>38</sub>(SR)<sub>24</sub>, and (c) Au<sub>144</sub>(SR)<sub>60</sub>. The cluster models for (a), (b), and (c) are taken from crystal structures in refs<sup>[29, 31, 33]</sup>, respectively. Reprinted with permission from {Ohta, T.; Shibuta, M.; Tsunoyama, H.; Negishi, Y.; Eguchi, T.; Nakajima, A. Size and structure dependence of electronic states in thiolate-protected gold nanoclusters of Au<sub>25</sub>(SR)<sub>18</sub>, Au<sub>38</sub>(SR)<sub>24</sub>, and Au<sub>144</sub>(SR)<sub>60</sub> }. Copyright {2013} American Chemical Society.

having the same CN. The ACNs of Au<sub>25</sub>(SR)<sub>18</sub>, (b) Au<sub>38</sub>(SR)<sub>24</sub>, and (c) Au<sub>144</sub>(SR)<sub>60</sub> are estimated to be 6.24, 6.32, and 8.92 based on their structural models.<sup>[29,31,33]</sup> The first coordination shell distance is defined as 0.29–0.32 nm, which is slightly larger than the nearest-neighbor distance of bulk Au (0.288 nm). It is found that Au<sub>25</sub>(SR)<sub>18</sub> and Au<sub>38</sub>(SR)<sub>24</sub> have almost the same ACN although their sizes are different, which is quite consistent with the obtained  $\Delta_{5d}$  value. These results clearly indicate that  $\Delta_{5d}$  of nanocluster depends not on their sizes but rather on ACNs.

Note that the intensity of the Au  $5d_{5/2}$  component relative to that of Au  $5d_{3/2}$  obviously decreased with reducing the cluster size, which is clearly seen in superimposed spectra normalized to the maxima of the Au  $5d_{3/2}$  shown in Figure 3.6. There have been reports on a decrease of the  $5d$ -electron or an increase in that of  $5d$ -hole with a decrease the size of Au:SR NPs based on XANES measurement on the Au  $L_3$ -edge, from which it is possible to probe the unoccupied densities of  $5d$  state just above the Fermi level arising from  $s$ - $d$  hybridization in Au.<sup>[23]</sup> Zhang and Sham have estimated the contribution of  $5d_{5/2}$  and  $5d_{3/2}$  to the  $d$ -hole redistribution by measuring the XANES of Au:SR NPs at the  $L_3$  and  $L_2$  edges, which are associated with a dipole transition from  $2p_{3/2}$  to  $5d_{5/2,3/2}$  and from  $2p_{1/2}$  to  $5d_{3/2}$ , respectively, and they concluded that the holes in the  $5d_{3/2}$  orbitals show a more significant change than that of the  $5d_{5/2}$ .<sup>[28]</sup> Ohyama *et al.*, however, have pointed out that the Au  $L_3$ - and  $L_2$ -edge XANES spectra reflected not only the electronic properties of the Au NPs themselves, but also the large scattering intensity of the Au-S pair, which is more significant in the  $L_2$ -edge.<sup>[46]</sup> Therefore, the XANES spectra cannot provide straightforward information to quantitatively evaluate the contribution of  $5d_{5/2}$  and  $5d_{3/2}$ .

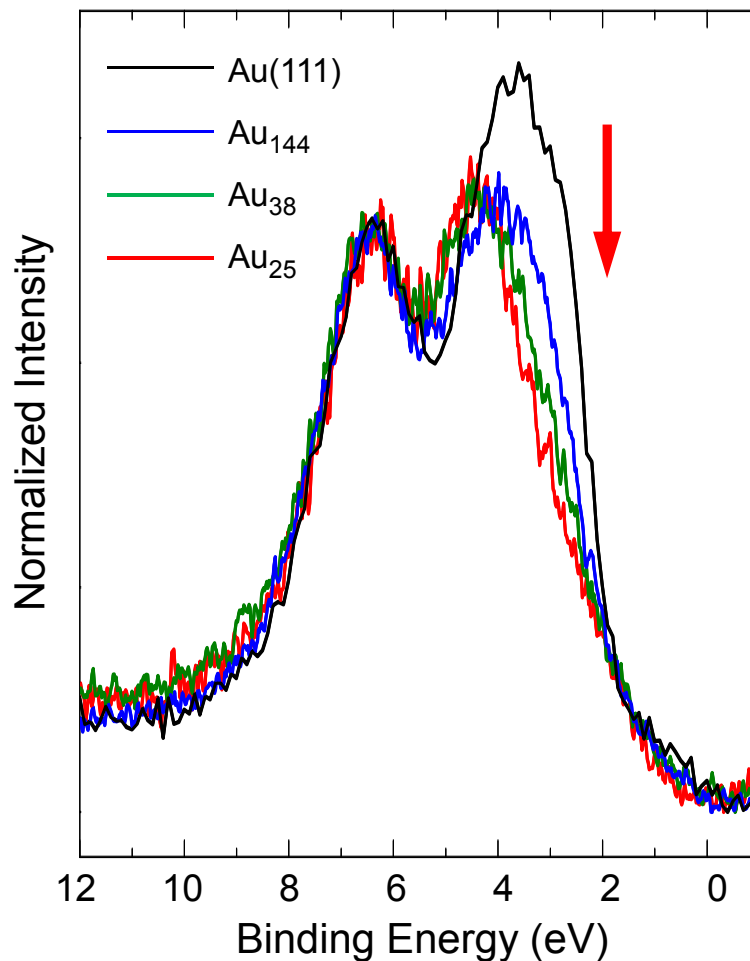


Figure 3.6 Overlaid Au 5d XPS spectra of Au(111), Au<sub>144</sub>(SR)<sub>60</sub>, Au<sub>38</sub>(SR)<sub>24</sub>, and Au<sub>25</sub>(SR)<sub>18</sub>. All the spectra were normalized to the Au 5d<sub>3/2</sub> intensity. Reprinted with permission from {Ohta, T.; Shibuta, M.; Tsunoyama, H.; Negishi, Y.; Eguchi, T.; Nakajima, A. Size and structure dependence of electronic states in thiolate-protected gold nanoclusters of Au<sub>25</sub>(SR)<sub>18</sub>, Au<sub>38</sub>(SR)<sub>24</sub>, and Au<sub>144</sub>(SR)<sub>60</sub> }. Copyright {2013} American Chemical Society.

Alternatively, our XPS measurement directly reveals that the decrement of the Au 5d electron preferentially occurs in the 5d<sub>5/2</sub> orbital: The electron depletion in the Au 5d band becomes significant as the cluster size decreases, as shown in Figure 3.6. This can be explained by the ratio of Au atoms to S atoms ligated. As pointed out by

Venkataraman and coworkers,<sup>[47]</sup> it is reasonable that the interaction between Au and S atoms involves electron donation from the S lone pair to Au 6s and a back-donation from Au 5d to S states, but it seems that an electron accepting part should be discussed in detail. In theoretical calculations for ligand-protected Au<sub>102</sub>(SC<sub>7</sub>O<sub>2</sub>H<sub>5</sub>)<sub>44</sub> clusters,<sup>[48]</sup> the Au atoms in the outermost layer show a small but distinct positive mean charge, and DOS for Au 5d in the outermost layer is smaller than those in the inner layers. Furthermore, for density of states projected on local atomic basis (PLDOS) for S atoms of thiolate-protected Au<sub>25</sub>(SR)<sub>18</sub> and Au<sub>38</sub>(SR)<sub>24</sub> clusters,<sup>[49, 50]</sup> theoretical calculations show that their PLDOS for S 3p are distributed widely in the range from -7 to 0 eV. Our result clearly shows that a substantial charge transfer takes place particularly in the outermost Au layer when thiols interact with an Au atom. Since the electronegativity of an S atom is slightly larger than that of an Au atom, it is likely that a charge transfer from Au to S occurs from the Au 5d<sub>5/2</sub> orbital rather than from the Au 5d<sub>3/2</sub>. Since the 5d<sub>5/2</sub> orbital is less stable than 5d<sub>3/2</sub>, it seems reasonable that the 5d<sub>5/2</sub> orbital is more responsible for metal-ligand binding.

The electronic structures of Au<sub>25</sub>(SR)<sub>18</sub><sup>[30, 51-54]</sup> and Au<sub>38</sub>(SR)<sub>24</sub><sup>[50, 55, 56]</sup> nanoclusters have been extensively discussed based on theoretical calculation. The calculations based on density functional theory have reveal that the *d*-band of Au<sub>25</sub>(SR)<sub>18</sub>, which is mostly composed of Au 5d atomic orbitals, is distributed narrower energy range and have a less component at lower binding energy compare to that of Au<sub>38</sub>(SR)<sub>24</sub>.<sup>[30, 55]</sup> A similar tendency has also been reported through that comparison of Au<sub>25</sub>(SR)<sub>18</sub> and Au<sub>19</sub>(SR)<sub>13</sub>,<sup>[54]</sup> which reveals the *d* bandwidth of core-Au atoms becomes narrower with a decreasing number of atoms, while that of shell-Au atoms are almost unchanged.

These results are quite consistent with our experimental findings indicating preferential electron depletion at the lower binding energy side, as shown in Figure 3.6.

## 3.4 Conclusions

We have systematically investigated the electronic states of Au:SR magic-number clusters of various sizes using XPS. The Au  $4f$  and S  $2p$  core-level spectra of each cluster have been interpreted in a manner consistent with their geometric structures. We have clearly demonstrated the size- and structure-dependent change in the valence electronic states. These findings will be useful in developing a deeper understanding of the relations between geometric and electronic structures of other ligand-protected metal nanoclusters.

## References

- [1] H. Haberland. *Clusters of atoms and molecules: theory, experiment, and clusters of atoms*, Vol. 52. Springer Science & Business Media, 2013.
- [2] G. Schmid. *Clusters and colloids: from theory to applications*. John Wiley & Sons, 2008.
- [3] A. C. Templeton, W. P. Wuelfing and R. W. Murray. “Monolayer-protected cluster molecules”. *Acc. Chem. Res.*, **2000**, 33(1), 27–36.
- [4] R. L. Whetten, J. T. Khoury, M. M. Alvarez, S. Murthy, I. Vezmar, Z. Wang, P. W. Stephens, C. L. Cleveland, W. Luedtke and U. Landman. “Nanocrystal gold molecules”. *Adv. Mater.*, **1996**, 8(5), 428–433.
- [5] T. Tsukuda. “Toward an atomic-level understanding of size-specific properties of protected and stabilized gold clusters”. *B. Chem. Soc. Jpn.*, **2012**, 85(2), 151–168.
- [6] R. Jin. “Quantum sized, thiolate-protected gold nanoclusters”. *Nanoscale*, **2010**, 2(3), 343–362.
- [7] J. F. Parker, C. A. Fields-Zinna and R. W. Murray. “The story of a monodisperse gold nanoparticle: Au<sub>25</sub>L<sub>18</sub>”. *Acc. Chem. Res.*, **2010**, 43(9), 1289–1296.
- [8] H. Häkkinen. “Atomic and electronic structure of gold clusters: understanding flakes, cages and superatoms from simple concepts”. *Chem. Soc. Rev.*, **2008**, 37(9), 1847–1859.
- [9] M. Walter, J. Akola, O. Lopez-Acevedo, P. D. Jadzinsky, G. Calero, C. J. Ackerson, R. L. Whetten, H. Grönbeck and H. Häkkinen. “A unified view of ligand-

- protected gold clusters as superatom complexes”. *Proc. Natl. Acad. Sci. U.S.A.*, **2008**, 105(27), 9157–9162.
- [10] H. Häkkinen. “The gold-sulfur interface at the nanoscale”. *Nat. Chem.*, **2012**, 4(6), 443–455.
- [11] Y. Negishi, K. Nobusada and T. Tsukuda. “Glutathione-protected gold clusters revisited: bridging the gap between gold (I)-thiolate complexes and thiolate-protected gold nanocrystals”. *J. Am. Chem. Soc.*, **2005**, 127(14), 5261–5270.
- [12] S. Chen, R. S. Ingram, M. J. Hostetler, J. J. Pietron, R. W. Murray, T. G. Schaaff, J. T. Khoury, M. M. Alvarez and R. L. Whetten. “Gold nanoelectrodes of varied size: transition to molecule-like charging”. *Science*, **1998**, 280(5372), 2098–2101.
- [13] S. Knoppe, N. Kothalawala, V. R. Jupally, A. Dass and T. Bürgi. “Ligand dependence of the synthetic approach and chiroptical properties of a magic cluster protected with a bicyclic chiral thiolate”. *Chem. Commun.*, **2012**, 48(38), 4630–4632.
- [14] H. Yao, K. Miki, N. Nishida, A. Sasaki and K. Kimura. “Large optical activity of gold nanocluster enantiomers induced by a pair of optically active penicillamines”. *J. Am. Chem. Soc.*, **2005**, 127(44), 15536–15543.
- [15] T. G. Schaaff, G. Knight, M. N. Shafiqullin, R. F. Borkman and R. L. Whetten. “Isolation and selected properties of a 10.4 kDa gold: glutathione cluster compound”. *J. Phys. Chem. B*, **1998**, 102(52), 10643–10646.
- [16] T. Laaksonen, V. Ruiz, P. Liljeroth and B. M. Quinn. “Quantised charging of monolayer-protected nanoparticles”. *Chem. Soc. Rev.*, **2008**, 37(9), 1836–1846.
- [17] Y. Negishi, H. Tsunoyama, M. Suzuki, N. Kawamura, M. M. Matsushita,

- K. Maruyama, T. Sugawara, T. Yokoyama and T. Tsukuda. “X-ray magnetic circular dichroism of size-selected, thiolated gold clusters”. *J. Am. Chem. Soc.*, **2006**, 128(37), 12034–12035.
- [18] P. Crespo, R. Litrán, T. Rojas, M. Multigner, J. D. I. Fuente, J. Sánchez-López, M. García, A. Hernando, S. Penadés and A. Fernández. “Permanent magnetism, magnetic anisotropy, and hysteresis of thiol-capped gold nanoparticles”. *Phys. Rev. Lett.*, **2004**, 93(8), 087204.
- [19] H. Hori, Y. Yamamoto, T. Iwamoto, T. Miura, T. Teranishi and M. Miyake. “Diameter dependence of ferromagnetic spin moment in Au nanocrystals”. *Phys. Rev. B*, **2004**, 69(17), 174411.
- [20] Y. Zhu, H. Qian, B. A. Drake and R. Jin. “Atomically Precise Au<sub>25</sub>(SR)<sub>18</sub> Nanoparticles as Catalysts for the Selective Hydrogenation of  $\alpha$ ,  $\beta$ -Unsaturated Ketones and Aldehydes”. *Angew. Chem., Int. Ed.*, **2010**, 122(7), 1317–1320.
- [21] Y. Zhu, Z. Wu, C. Gayathri, H. Qian, R. R. Gil and R. Jin. “Exploring stereoselectivity of Au<sub>25</sub> nanoparticle catalyst for hydrogenation of cyclic ketone”. *J. Catal.*, **2010**, 271(2), 155–160.
- [22] M. A. MacDonald, P. Zhang, N. Chen, H. Qian and R. Jin. “Solution-phase structure and bonding of Au<sub>38</sub>(SR)<sub>24</sub> nanoclusters from X-ray absorption spectroscopy”. *J. Phys. Chem. C*, **2010**, 115(1), 65–69.
- [23] M. A. MacDonald, P. Zhang, H. Qian and R. Jin. “Site-Specific and Size-Dependent Bonding of Compositionally Precise Gold-Thiolate Nanoparticles from X-ray Spectroscopy”. *J. Phys. Chem. Lett.*, **2010**, 1(12), 1821–1825.
- [24] A. Tanaka, Y. Takeda, M. Imamura and S. Sato. “Dynamic final-state effect on the

- Au 4*f* core-level photoemission of dodecanethiolate-passivated Au nanoparticles on graphite substrates”. *Phys. Rev. B*, **2003**, 68(19), 1–5.
- [25] A. Tanaka, Y. Takeda, T. Nagasawa and K. Takahashi. “Chemical states of dodecanethiolate-passivated Au nanoparticles: synchrotron-radiation photoelectron spectroscopy”. *Solid State Commun.*, **2003**, 126, 191–196.
- [26] Y. Yiu, P. Zhang and T. Sham. “The Electronic Properties and L<sub>3</sub> XANES of Au and Nano-Au”. **2003**, 3, 183–186.
- [27] P. Zhang and T. Sham. “X-ray studies of the structure and electronic behavior of alkanethiolate-capped gold nanoparticles: The interplay of size and surface effects”. *Phys. Rev. Lett.*, **2003**, 90(245502), 3–6.
- [28] P. Zhang and T. Sham. “Tuning the electronic behavior of Au nanoparticles with capping molecules”. *Appl. Phys. Lett.*, **2002**, 81, 736–738.
- [29] M. W. Heaven, A. Dass, P. S. White, K. M. Holt and R. W. Murray. “Crystal structure of the gold nanoparticle [N(C<sub>8</sub>H<sub>17</sub>)<sub>4</sub>][Au<sub>25</sub>(SCH<sub>2</sub>CH<sub>2</sub>Ph)<sub>18</sub>]”. *J. Am. Chem. Soc.*, **2008**, 130(12), 3754–3755.
- [30] M. Zhu, C. M. Aikens, F. J. Hollander, G. C. Schatz and R. Jin. “Correlating the crystal structure of a thiol-protected Au<sub>25</sub> cluster and optical properties”. *J. Am. Chem. Soc.*, **2008**, 130(18), 5883–5885.
- [31] H. Qian, W. T. Eckenhoff, Y. Zhu, T. Pintauer and R. Jin. “Total structure determination of thiolate-protected Au<sub>38</sub> nanoparticles”. *J. Am. Chem. Soc.*, **2010**, 132(24), 8280–8281.
- [32] P. D. Jadzinsky, G. Calero, C. J. Ackerson, D. A. Bushnell and R. D. Kornberg. “Structure of a thiol monolayer-protected gold nanoparticle at 1.1 Å resolution”.

- Science*, **2007**, 318(5849), 430–433.
- [33] O. Lopez-Acevedo, J. Akola, R. L. Whetten, H. Gronbeck and H. Häkkinen. “Structure and bonding in the ubiquitous icosahedral metallic gold cluster  $\text{Au}_{144}(\text{SR})_{60}$ ”. *J. Phys. Chem. C*, **2009**, 113(13), 5035–5038.
- [34] M. Brust, M. Walker, D. Bethell, D. J. Schiffrin and R. Whyman. “Synthesis of thiol-derivatised gold nanoparticles in a two-phase liquid–liquid system”. *J. Chem. Soc., Chem. Commun.*, **1994**, (7), 801–802.
- [35] Y. Negishi, N. K. Chaki, Y. Shichibu, R. L. Whetten and T. Tsukuda. “Origin of magic stability of thiolated gold clusters: a case study on  $\text{Au}_{25}(\text{SC}_6\text{H}_{13})_{18}$ ”. *J. Am. Chem. Soc.*, **2007**, 129(37), 11322–11323.
- [36] N. K. Chaki, Y. Negishi, H. Tsunoyama, Y. Shichibu and T. Tsukuda. “Ubiquitous 8 and 29 kDa gold: alkanethiolate cluster compounds: mass-spectrometric determination of molecular formulas and structural implications”. *J. Am. Chem. Soc.*, **2008**, 130(27), 8608–8610.
- [37] P. H. Citrin, G. K. Wertheim and Y. Baer. “Surface-atom x-ray photoemission from clean metals: Cu, Ag, and Au”. *Phys. Rev. B*, **1983**, 27(6), 3160–3175.
- [38] G. Wertheim, S. DiCenzo and S. Youngquist. “Unit charge on supported gold clusters in photoemission final state”. *Phys. Rev. Lett.*, **1983**, 51(25), 2310–2313.
- [39] A. Howard, D. N. S. Clark, C. E. J. Mitchell, R. G. Egdell and V. R. Dhanak. “Initial and final state effects in photoemission from Au nanoclusters on  $\text{TiO}_2(110)$ ”. *Surf. Sci.*, **2002**, 518(3), 210–224.
- [40] M. P. Seah and W. A. Dench. “Quantitative electron spectroscopy of surfaces: A standard data base for electron inelastic mean free paths in solids”. *Surf. Interface*

- Anal.*, **1979**, 1(1), 2–11.
- [41] W. A. Clay, Z. Liu, W. Yang, J. D. Fabbri, J. E. Dahl, R. M. K. Carlson, Y. Sun, P. R. Schreiner, A. A. Fokin, B. A. Tkachenko, N. A. Fokina, P. A. Pianetta, N. Melosh and Z. X. Shen. “Origin of the monochromatic photoemission peak in diamondoid monolayers”. *Nano Lett.*, **2009**, 9(1), 57–61.
- [42] Y. Zhu, R. Jin and Y. Sun. “Atomically monodisperse gold nanoclusters catalysts with precise core-shell structure”. *Catalysts*, **2011**, 1(1), 3–17.
- [43] A. Bzowski, T. K. Sham, R. E. Watson and M. Weinert. “Electronic structure of Au and Ag overlayers on Ru(001): The behavior of the noble-metal d bands”. *Phys. Rev. B*, **1995**, 51(15), 9979–9984.
- [44] T. K. Sham, Y. M. Yiu, M. Kuhn and K. H. Tan. “Electronic structure of ordered and disordered Cu<sub>3</sub>Au: The behavior of the Au 5d bands”. *Phys. Rev. B*, **1990**, 41(17), 11881–11886.
- [45] K. Pirkkalainen and R. Serimaa. “Coordination number in ideal spherical nanocrystals”. *J. Appl. Crystallogr.*, **2009**, 42, 442–447.
- [46] J. Ohyama, K. Teramura, T. Shishido, Y. Hitomi, K. Kato, H. Tanida, T. Uruga and T. Tanaka. “In situ Au L<sub>3</sub> and L<sub>2</sub> edge XANES spectral analysis during growth of thiol protected gold nanoparticles for the study on particle size dependent electronic properties”. *Chem. Phys. Lett.*, **2011**, 507(1-3), 105–110.
- [47] Y. S. Park, A. C. Whalley, M. Kamenetska, M. L. Steigerwald, M. S. Hybertsen, C. Nuckolls and L. Venkataraman. “Contact chemistry and single-molecule conductance: a comparison of phosphines, methyl sulfides, and amines”. *J. Am. Chem. Soc.*, **2007**, 129(51), 15768–15769.

- [48] O. Lopez-Acevedo, P. Clayborne and H. Häkkinen. “Electronic structure of gold, aluminum, and gallium superatom complexes”. *Phys. Rev. B*, **2011**, 84(3), 035434.
- [49] J. Akola, K. A. Kacprzak, O. Lopez-Acevedo, M. Walter, H. Grönbeck and H. Häkkinen. “Thiolate-protected Au<sub>25</sub> superatoms as building blocks: dimers and crystals”. *J. Phys. Chem. C*, **2010**, 114(38), 15986–15994.
- [50] O. Lopez-Acevedo, H. Tsunoyama, T. Tsukuda and C. M. Aikens. “Chirality and electronic structure of the thiolate-protected Au<sub>38</sub> nanocluster”. *J. Am. Chem. Soc.*, **2010**, 132(23), 8210–8218.
- [51] J. Akola, M. Walter, R. L. Whetten, H. Häkkinen and H. Grönbeck. “On the structure of thiolate-protected Au<sub>25</sub>”. *J. Am. Chem. Soc.*, **2008**, 130(12), 3756–3757.
- [52] C. M. Aikens. “Geometric and electronic structure of Au<sub>25</sub>(SPhX)<sub>18</sub><sup>-</sup> (X= H, F, Cl, Br, CH<sub>3</sub>, and OCH<sub>3</sub>)”. *J. Phys. Chem. Lett.*, **2010**, 1(17), 2594–2599.
- [53] C. M. Aikens. “Effects of core distances, solvent, ligand, and level of theory on the TDDFT optical absorption spectrum of the thiolate-protected Au<sub>25</sub> nanoparticle”. *The Journal of Physical Chemistry A*, **2009**, 113(40), 10811–10817.
- [54] D. M. Chevrier, M. A. MacDonald, A. Chatt, P. Zhang, Z. Wu and R. Jin. “Sensitivity of structural and electronic properties of gold-thiolate nanoclusters to the atomic composition: A comparative X-ray study of Au<sub>19</sub>(SR)<sub>13</sub> and Au<sub>25</sub>(SR)<sub>18</sub>”. *J. Phys. Chem. C*, **2012**, 116(47), 25137–25142.
- [55] Y. Pei, Y. Gao and X. C. Zeng. “Structural prediction of thiolate-protected Au<sub>38</sub>: a face-fused bi-icosahedral Au core”. *J. Am. Chem. Soc.*, **2008**, 130(25), 7830–7832.
- [56] M. A. MacDonald, P. Zhang, N. Chen, H. Qian and R. Jin. “Solution-phase struc-

ture and bonding of Au<sub>38</sub>(SR)<sub>24</sub> nanoclusters from X-ray absorption spectroscopy”.

*J. Phys. Chem. C*, **2010**, 115(1), 65–69.

## Chapter 4

# Chemical Characterization of an Alkali-like Superatom Consisting of a Ta-encapsulating Si<sub>16</sub> cage

## 4.1 Introduction

Recently there has been notable progress in cluster science that has revealed a promising potential for opening up new avenues of material science based on organic and inorganic chemistry.<sup>[1-10]</sup> Following the discovery of carbon-based fullerene,<sup>[11]</sup> many synthetic and theoretical investigations have been conducted. In particular, metal (M)-encapsulating binary nanoclusters, such as  $M@B_n$ ,<sup>[12]</sup>  $M@Si_n$ ,<sup>[13-23]</sup>  $M@Al_{12}$ ,<sup>[24, 25]</sup>  $M@Au_{12}$ ,<sup>[26]</sup> and  $M@Sn_n$ ,<sup>[23, 27]</sup> have attracted much attention.

The greatest advantage of the metal-atom encapsulating binary nanocluster is that their functionalities can be designed by selecting the species of encapsulating central atom while retaining the geometrical symmetry. Among them, metal-atom encapsulating  $Si_{16}$  cage nanoclusters of the  $M@Si_{16}$  have been extensively investigated experimentally and theoretically, because they exhibit so-called magic number behavior in the gas phase,<sup>[13-23]</sup> and because they seem to have a close affinity for silicon-based electronic nanodevices.<sup>[14, 20, 28]</sup> Koyasu *et al.* firstly discovered the unique magic number behavior experimentally by generating clusters with the double-laser vaporization method. That is, the stable charge of  $M@Si_{16}$  changes with the central metal atom.<sup>[15]</sup> The origin of the magic number behavior has been experimentally and theoretically interpreted using two factors of geometric stability resulting from high structural symmetry and electronic shell closure (68 electrons).<sup>[19]</sup> Since the electronic closure in  $M@Si_{16}$  is satisfied by encapsulating group-4 atoms ( $M = Ti, Zr, \text{ and } Hf$ ) in the neutrals,  $M@Si_{16}$  with group-3 ( $M = Sc, Y, \text{ and } Lu$ ) and group-5 ( $M = V, Nb, \text{ and } Ta$ ) atoms complete

the 68 electron shells in the anion and cation forms, respectively.<sup>[15–19, 21–23]</sup> This means that superatoms with halogen-, rare-gas-, and alkali-like natures can be fabricated by changing the central atom of  $M@Si_{16}$ . In these extensive discussions of the magic number behavior for  $M@Si_{16}$ , however, there have been a few experimental approaches to elucidate their chemical robustness even in the free gas phase.<sup>[17]</sup> This problem was mainly caused because the amount of generated cluster was limited due to the generation system. In other words, if one can improve the synthetic quantity of  $M@Si_{16}$ , various evaluation methods will be applicable.

Such caged nanoclusters can be expected to act as a building block for nanocluster-assembled materials, the chemical robustness of the nanocluster being an important factor in successfully fabricating functional nanomaterials via the accumulation and aggregation of individual nanoclusters. One of the major strategies for nanocluster-assembled materials is the formation of a ligated nanocluster, in which an appropriate ligand protects the nanocluster core geometrically and electronically, to prevent from degradation of their intrinsic properties induced by aggregation of the nanoclusters. Ligand-free accumulation is another important route to form the nanocluster-assembled material, particularly as the properties of an assembly of naked nanoclusters are expected to be unsteady but revolutionary because of conserving their superatomic nature. This strategy has a promising potential to discover a novel property of the assembled nanoclusters owing to their superatomic interaction, which is attractive from the viewpoints of providing charge transport with lower energy dissipation and higher mobility.

In order to utilize the superatomic nanoclusters in a naked form for assembly into functional devices, they need to be deposited and immobilized onto a solid-state substrate.

To perform the size selective isolation of the naked nanoclusters, magic numbered “ion” formation in the gas phase is a versatile tool to couple with mass spectrometry. The caged nanocluster of  $\text{Ta@Si}_{16}^+$  is a good candidate to examine the superatomic behavior to assemble themselves, because an ion signal of  $\text{TaSi}_{16}^+$  ( $m/z = 630$ ) prominently appears as magic numbers.<sup>[15,17]</sup> Indeed the deposition of  $\text{Ta@Si}_{16}^+$  onto a substrate was examined by scanning probe microscopy/spectroscopy showing the physical properties of height and the HOMO-LUMO gap on several substrates,<sup>[29,30]</sup> but important chemical issues of their chemical states and stability are unknown for the functional assembled materials.

Here, we have deposited  $\text{Ta@Si}_{16}^+$  (Figure 4.1) on a surface of highly oriented pyrolytic graphite (HOPG) and probed its chemical state and chemical stability by means of X-ray photoelectron spectroscopy (XPS), which provides reliable information about chemical status of particular elements by measuring the energy positions of inner-core electrons. The result shows that the  $\text{Ta@Si}_{16}$  deposited on the substrate maintains its

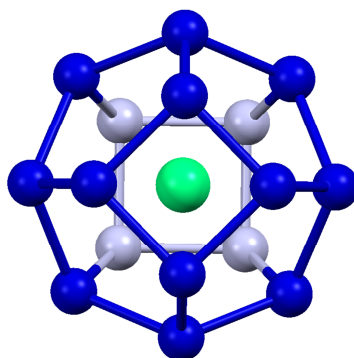


Figure 4.1 A molecule model of  $\text{Ta@Si}_{16}^+$ . Sixteen blue spheres show Si atoms and a central green sphere shows a Ta atom.

metal-encapsulating framework even after thermal and chemical treatments, and fur-

ther revealing the formation of spatially delocalized electronic states owing to the charge transfer between  $\text{Ta@Si}_{16}^+$  and a counter anion,  $\text{C}_{60}^-$ .

## 4.2 Experiment

The apparatus and principle of nanocluster generation and photoelectron spectroscopy were described in Chapter 2. In this section, the experimental manipulation of sample preparation is introduced.

Briefly, prior to the  $\text{Ta@Si}_{16}$  nanocluster deposition, a HOPG surface was cleaned by cleaving in atmosphere and heating (750 K, >50 h) in ultrahigh vacuum (UHV,  $<2 \times 10^{-8}$  Pa) and coated with a  $\text{C}_{60}$  film using a Knudsen effusion cell. The  $\text{C}_{60}$  film thickness and growth speed were set to two monolayers (MLs) and 0.07 ML/min, respectively, under quartz crystal microbalance monitoring. The  $\text{Ta@Si}_{16}$  nanoclusters were generated by magnetron sputtering using a Ta-Si alloy target and  $\text{Ar}^+$  ions at the cluster ion source.

By optimizing the condition of the nanocluster synthesis, the  $\text{Ta@Si}_{16}^+$  cations were selectively generated and selectively deposited onto a HOPG substrate by fixing the quadrupole mass filter at an  $m/z$  value of 630 with a mass resolution ( $m/\Delta m$ ) of about 50. Deposition time and average ion current were set to 150 min and 510 pA, respectively, which corresponds to  $5 \times 10^{13}$  nanoclusters in total. Assuming a deposition area of  $2.8 \times 10^{13}$  nm<sup>2</sup> (6 mm in diameter) and a  $\text{Ta@Si}_{16}$  diameter of 0.8–0.9 nm,<sup>[29]</sup> the nanocluster coverage was estimated to be 1 ML.

The deposited sample was transferred to an XPS and UPS system connected with

the nanocluster deposition system under UHV conditions and exposed to X-ray (Mg  $K\alpha$ ; photon energy ( $h\nu$ ) = 1253.6 eV) or vacuum ultraviolet irradiation (He I $\alpha$ ;  $h\nu$  = 21.22 eV). A sample voltage is applied during the deposition to collect the cluster ion but it was kept to be as close to zero as possible, to typically more than  $-5$  V. The applied voltage makes it possible to soft land the Ta@Si<sub>16</sub> nanoclusters on the HOPG with a low kinetic energy of  $< 0.5$  eV per atom. The typical deposition amount is  $5 \times 10^{13}$  ions, which is estimated by the ion current measured from the sample and the deposition time. The diameter of the nanocluster-deposited area is about 8.5 mm. The nanocluster deposited sample was transferred to the XPS system connected to the deposition system while maintaining vacuum conditions (about  $10^{-8}$  Pa).

All XPS measurements were performed in an ultrahigh vacuum (UHV) chamber where the base pressure was better than  $2 \times 10^{-8}$  Pa. In the XPS measurement, an X-ray (Mg  $K\alpha$ , photon energy ( $h\nu$ ) = 1253.6 eV) was irradiated onto the sample surface, and photoelectrons were detected by a hemispherical electron analyzer with a detection angle of  $45^\circ$  from surface normal. The binding energy of core electrons was calibrated by the XPS peak of the Au 4f core level (see Chapter 3). It was carefully verified that there were no effects of X-ray irradiation on the XPS spectra for all samples.

## 4.3 Results

### 4.3.1 Geometric characterization of Ta@Si<sub>16</sub> deposited on a HOPG

Figure 4.2 shows XPS spectra (circles) measured around the (a) Si 2*p* and (b) Ta 4*f* core levels, where the background component determined by the Shirley method is

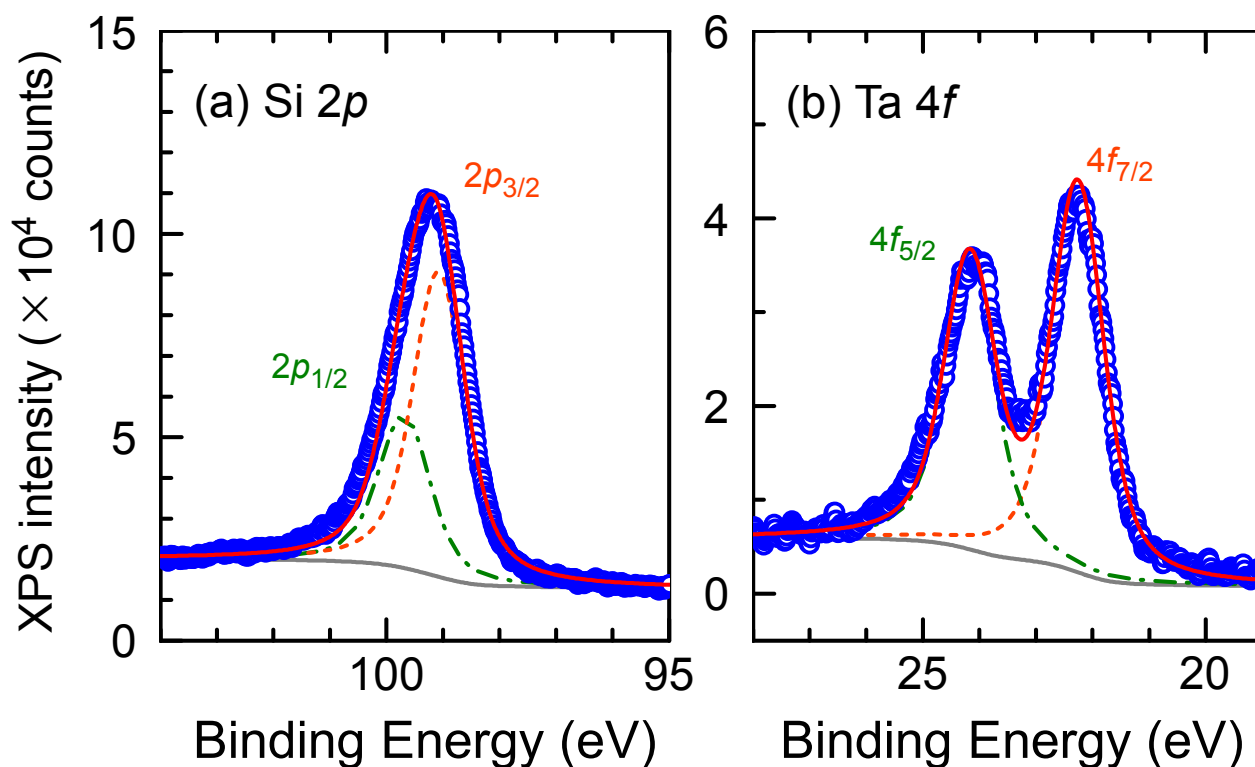


Figure 4.2 XPS spectra for Ta@Si<sub>16</sub> deposited on HOPG around (a) Si 2*p* and (b) Ta 4*f* core levels. The fitted results (red line) and spin-orbit contributions (orange dotted and green dashed dotted lines) are superimposed in (a) and (b). Reprinted with permission from {Shibuta, M.; Ohta, T.; Nakaya, M.; Tsunoyama, H.; Eguchi, T.; Nakajima, A. Chemical characterization of an alkali-like superatom consisting of a Ta-encapsulating Si<sub>16</sub> cage}. Copyright {2015} American Chemical Society.

4*f* and Si 2*p* is evaluated to be 1:1.58 that agrees well with the ratio calculated for Ta@Si<sub>16</sub> (1:1.53) using photoemission cross sections of Si 2*p* and Ta 4*f*.<sup>[31]</sup> For the chemical analysis of Ta 4*f* and Si 2*p* core levels, background groups were subtracted from the raw data, while XPS of bare HOPG is also subtracted in advance for the Ta 4*f*. After these treatments, bare core levels were fitted with a Voigt function having a full width at half maximum of 1.11 eV, whose Gaussian and Lorentzian contribution

## 図 4.2 Ta@Si<sub>16</sub>保護金クラスターの構造

are 0.75 eV and 0.56 eV, respectively, which is the instrumental broadening determined based on the measurement of the Au 4*f* core level for Au(111) surface. (See section 3.3.1) The energy separation and branching ratio for the spin-orbit splitting of Si 2*p* and Ta 4*f* are taken from literature values.<sup>[33,34]</sup> The orange dotted lines in Figure 4.2(a) and (b) represent the component of Si 2*p*<sub>3/2</sub> and Ta 4*f*<sub>7/2</sub>, and the green dashed dotted lines represent Si 2*p*<sub>1/2</sub> and Ta 4*f*<sub>5/2</sub>, respectively. As shown by the red lines, both levels are reproduced with a single chemical component indicating uniform chemical environments of Ta and Si. These results reveal that a symmetric Si cage is formed around the Ta atom as a metal-encapsulating cage structure of Ta@Si<sub>16</sub>, i.e., 16 Si atoms are isotropically distributed around a central Ta atom.

The energy position of Si 2*p*<sub>3/2</sub> (99.1 eV) is very close to the bulk value (99.2 eV),<sup>[33]</sup> while that of Ta 4*f*<sub>7/2</sub> (22.3 eV) is about 0.6 eV larger than that of the bulk (21.6 eV).<sup>[34]</sup> Since energy positions of both core levels of Si 2*p* and Ta 4*f* are sensitive to the number of valence electrons (about 1 eV shift per a valence electron),<sup>[35,36]</sup> the result indicates that Ta has a slight positive charge, while Si is almost neutral. In fact, the result implies that deposited Ta@Si<sub>16</sub> might be positively charged on the HOPG to satisfy a 68 electron shell closing, but it is hard to discuss the accurate charge state of individual Ta@Si<sub>16</sub> on HOPG with XPS. This is because the caged Si atoms themselves are negatively charged owing to larger electronegativity than Ta. Since the donated electron from the Ta atom is shared with 16 Si atoms, the amount of chemical shift in Si 2*p* is too small to determine the charge state.

As discussed below, our STM observations reveal that Ta@Si<sub>16</sub> deposited on HOPG accumulate into small islands. By analogy with alkali-metal atoms on graphite, the

charge transfer would be much less in the accumulated clusters than the isolated ones, which is supported by our XPS results for Ta@Si<sub>16</sub> on C<sub>60</sub> (see Chapter 5). Figures 4.3(a) and (b) show STM images (120 × 120 nm<sup>2</sup>) obtained from Ta@Si<sub>16</sub> deposited on a HOPG and a line profile taken along the broken line in the image. Island structures are formed and the islands consist of small dot-shaped components with a height of about 1 nm, which would correspond to individual Ta@Si<sub>16</sub>. The results indicate that Ta@Si<sub>16</sub> can accumulate while keeping their superatomic properties, although they do not show ordered arrangements on HOPG. Since assembled structures are formed not only by their own interactions but also by surface/interface interactions, a HOPG seems less likely to form a Ta@Si<sub>16</sub> assembly.

### 4.3.2 Heating effect

Figure 4.4 shows the background-subtracted XPS spectra before and after heating at a temperature of 720 K for 16 h. After the heating, the Si 2*p* slightly shifted toward the higher binding energy (BE) (99.5 eV) and asymmetrically broadened on the higher BE side, while the shape of Ta 4*f* was almost unchanged. This suggests that the surrounding Si cage of Ta@Si<sub>16</sub> is somewhat altered by heating, perhaps by partially coalescing with HOPG or themselves, but the preserved cage prevents the Ta atoms from interacting with others. In fact, when surface Si atoms are bonded with carbon atoms in a defect of the HOPG, it has been reported that the Si 2*p* are shifted to higher energy to around 101.3 eV.<sup>[37]</sup> Furthermore, the broadening of Si 2*p* implies the formation of amorphous network of silicon atoms.<sup>[38]</sup> Importantly, on heating, the compositional ratio of Ta to Si atoms remains constant based on the XPS intensity, Si 2*p*:Ta 4*f* =

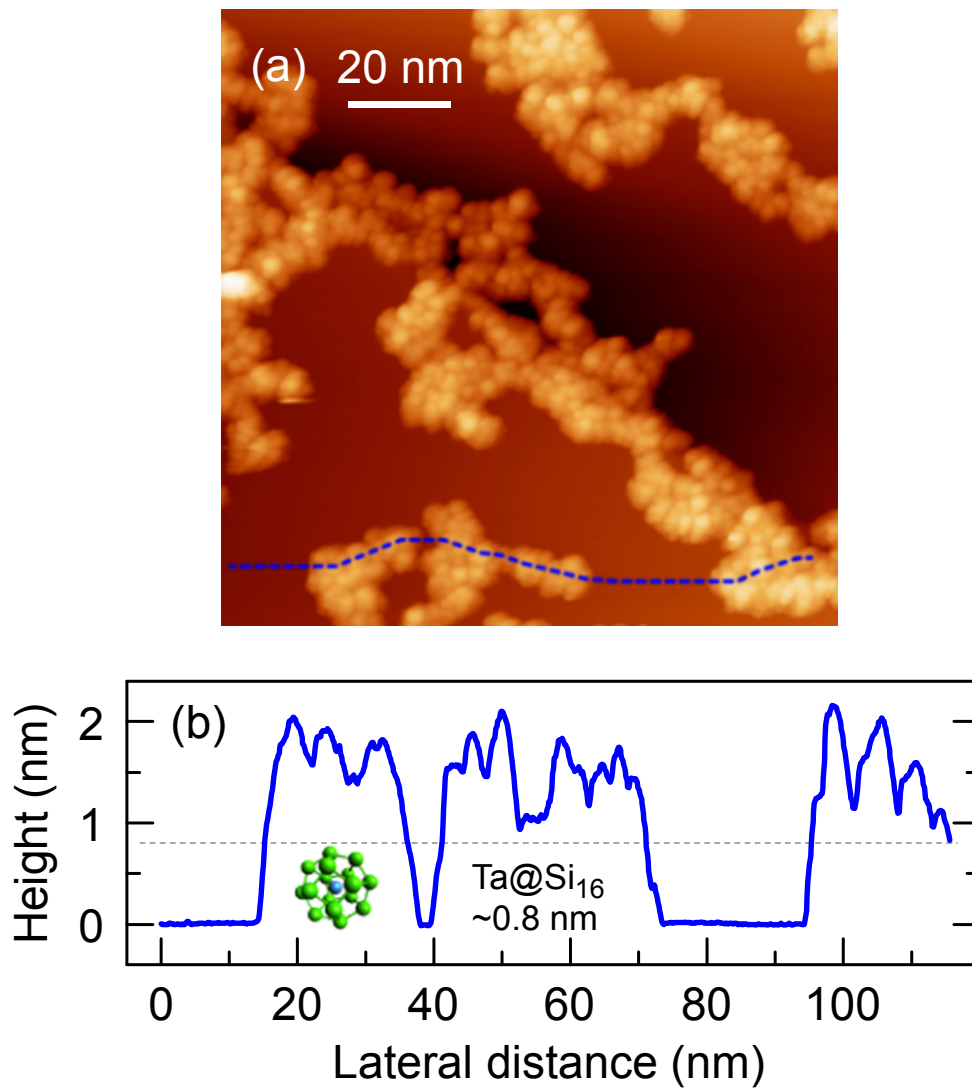


Figure 4.3 (a) An STM image ( $120 \times 120 \text{ nm}^2$ ) of Ta@Si<sub>16</sub> deposited HOPG surface. Tip bias ( $V_{\text{tip}}$ ) and current ( $I_t$ ) are  $-2.3 \text{ V}$  and  $2 \text{ pA}$ , respectively. (b) Height profile taken along a blue-dotted line in (a). Reprinted with permission from {Shibuta, M.; Ohta, T.; Nakaya, M.; Tsunoyama, H.; Eguchi, T.; Nakajima, A. Chemical characterization of an alkali-like superatom consisting of a Ta-encapsulating Si<sub>16</sub> cage}. Copyright {2015} American Chemical Society.

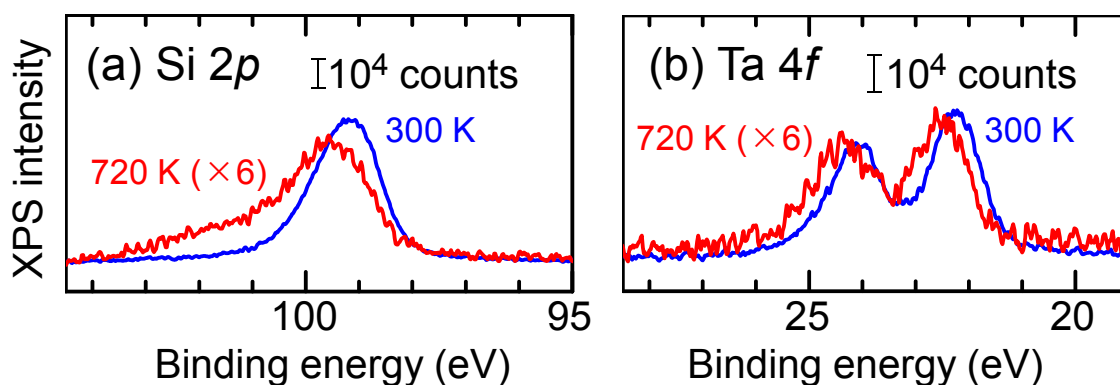


Figure 4.4 Background-subtracted XPS spectra of the Ta@Si<sub>16</sub> film for (a) Si 2*p* and (b) Ta 4*f* before and after heating (720 K, 16 h) are shown by blue and red lines, respectively. Reprinted with permission from {Shibuta, M.; Ohta, T.; Nakaya, M.; Tsunoyama, H.; Eguchi, T.; Nakajima, A. Chemical characterization of an alkali-like superatom consisting of a Ta-encapsulating Si<sub>16</sub> cage}. Copyright {2015} American Chemical Society.

1:1.63, and therefore the cage surface of Ta@Si<sub>16</sub> seems to be partially fused, thereby retaining their individuality. In fact, after heating at a temperature around 400 K, the individual Ta@Si<sub>16</sub> are still discernible in the STM images for the aggregated islands. Figure 4.5 shows STM images of Ta@Si<sub>16</sub> on HOPG at (a) 300 K and (b) 400 K. After heating at 400 K, the STM image was measured around 300 K. After heating, the size of the aggregated islands was enlarged, but the individual Ta@Si<sub>16</sub> nanoclusters are still discernible in the STM images. Furthermore, the heating lessens the intensity of each level to about 1/6, which indicates that the deposited nanoclusters aggregate, although it cannot be excluded that Ta@Si<sub>16</sub> itself might desorb from HOPG. This result may imply that there is a benefit in choosing an appropriate solvent to perform the initial purification steps, because the heating causes the partial degradation of Ta@Si<sub>16</sub>.

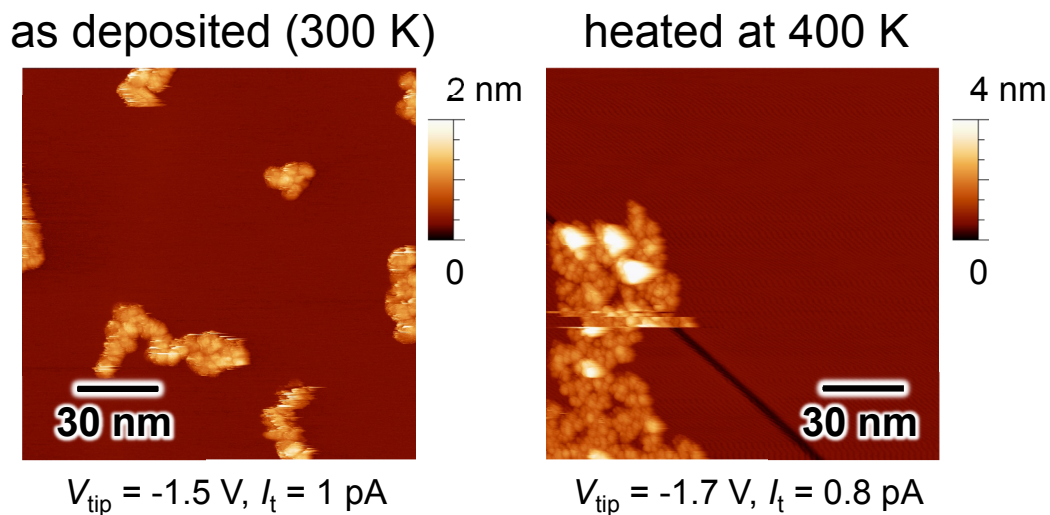


Figure 4.5 STM images of Ta@Si<sub>16</sub> on HOPG at (a) 300 K and (b) 400 K. Reprinted with permission from {Shibuta, M.; Ohta, T.; Nakaya, M.; Tsunoyama, H.; Eguchi, T.; Nakajima, A. Chemical characterization of an alkali-like superatom consisting of a Ta-encapsulating Si<sub>16</sub> cage}. Copyright {2015} American Chemical Society.

### 4.3.3 Oxygen exposure

The above results show that Ta@Si<sub>16</sub> maintains its metal-encapsulating framework even after deposition onto HOPG, hence being expected to exhibit high chemical stability. In order to demonstrate this, the Ta@Si<sub>16</sub> deposited on the HOPG was exposed to oxygen, and its chemical state tracked by XPS. Figure 4.6(a) and (b) shows the XPS spectra around the Si 2*p* and Ta 4*f* levels taken before and after oxygen exposure, respectively. Each spectrum is normalized by the total intensity after subtracting the background. Superimposed spectra normalized to the intensity are also shown at the bottom. The amount of oxygen exposure is noted in Langmuir, L (1 L = 1.33 × 10<sup>-4</sup> Pa s). For both levels, no significant difference is apparent below an exposure of 1 × 10<sup>4</sup>

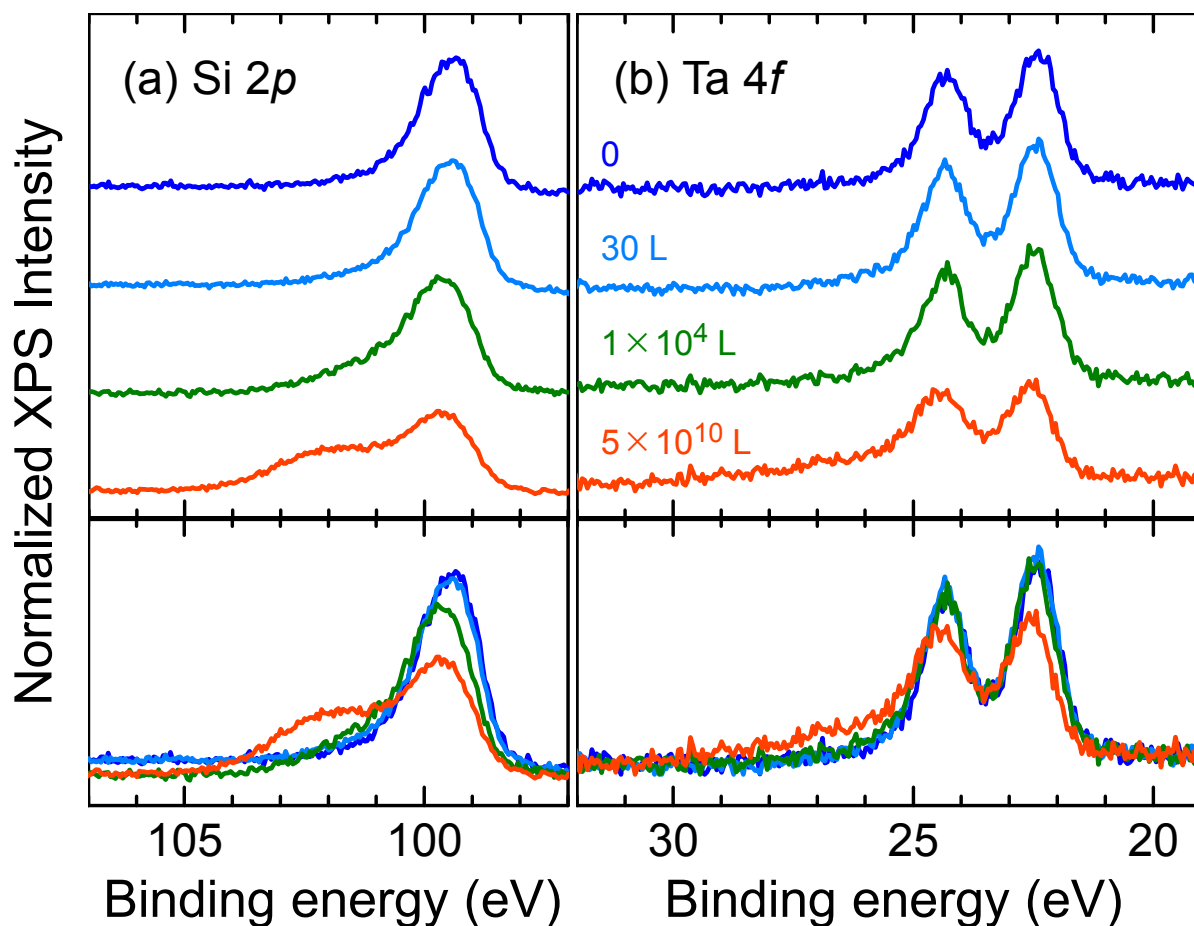


Figure 4.6 Normalized XPS spectra for Ta@Si<sub>16</sub> deposited on HOPG in (a) Si 2*p* and (b) Ta 4*f* levels, depending on oxygen exposures in the range 0–5 × 10<sup>10</sup> L, where the background are subtracted. For comparison, all series are superimposed in the bottom of each figure. Reprinted with permission from {Shibuta, M.; Ohta, T.; Nakaya, M.; Tsunoyama, H.; Eguchi, T.; Nakajima, A. Chemical characterization of an alkali-like superatom consisting of a Ta-encapsulating Si<sub>16</sub> cage}. Copyright {2015} American Chemical Society.

L. Even after exposing to 5 × 10<sup>10</sup> L (0.1 MPa × 60 s) oxygen, the main components of Si 2*p* and Ta 4*f* stay at the energy positions of pristine Ta@Si<sub>16</sub>, although additional components appear at higher BE of both levels, which can be attributed to the oxide of each element. Since it has been reported that surface atoms of bulk Si and Ta start to

react with oxygen at much smaller dosages,  $<50$  L,<sup>[35,39]</sup> our result clearly shows that Ta@Si<sub>16</sub> on HOPG has a very low reactivity toward oxygen.

Although Ta@Si<sub>16</sub> shows substantial resistance toward an O<sub>2</sub> adsorption reaction, it does eventually react to form oxides, and the Ta@Si<sub>16</sub> becomes markedly distorted. The O<sub>2</sub> exposure evolution of the Ta 4*f* peak is apparently slower than that of the Si 2*p* peak, suggesting that the surface Si of the cage is oxidized first, rather than the central Ta atom. Although the 1*s* peak of O atoms was observed at the BE of 532.5 eV, attributable to the oxidation states of O<sup>2-</sup> (Figure 4.7),<sup>[35]</sup> no clear direct evidence for (Ta@Si<sub>16</sub>)<sub>2</sub>O formation was obtained that would signal the stoichiometric behavior of an alkali-like superatom.

For comparison, anions of TaSi<sub>3</sub> nanoclusters, which cannot have a metal-encapsulating structure, were deposited onto HOPG and exposed to oxygen. Figures 4.8(a) and (b) shows the XPS spectra around Si 2*p* and Ta 4*f* obtained from TaSi<sub>3</sub> deposited on HOPG for changing oxygen dosages. Both levels show much broader structures than that of Ta@Si<sub>16</sub>. After exposing to  $5 \times 10^{10}$  L oxygen, clear peaks suggesting single chemical components appeared at the BE of 102.8 eV for Si 2*p* and 27.2 eV for Ta 4*f*<sub>7/2</sub>, which are close to those reported for a tantalum disilicide (TaSi<sub>2</sub>) film oxidized by exposing to air.<sup>[36]</sup> This result suggests that some of the TaSi<sub>3</sub> deposited on HOPG was already oxidized before oxygen exposure experiments. The oxidation of TaSi<sub>3</sub> during the synthesis and/or deposition could be caused by oxygen impurity contained in the Ar and He gases used to synthesize nanoclusters, because the concentration of residual oxygen ( $<0.01$  ppm by volume) might be sufficient to oxidize TaSi<sub>3</sub> even in the vacuum sample preparation. The above result clearly

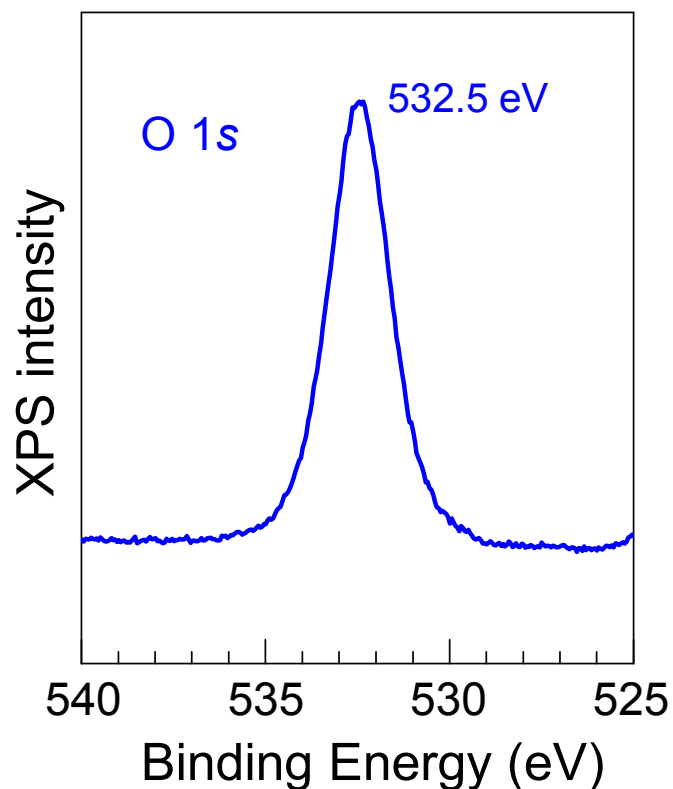


Figure 4.7 XPS spectrum of O 1s core levels for Ta@Si<sub>16</sub> on C<sub>60</sub>/HOPG after  $1 \times 10^5$  Pa oxygen exposure for 40 h. Reprinted with permission from {Shibuta, M.; Ohta, T.; Nakaya, M.; Tsunoyama, H.; Eguchi, T.; Nakajima, A. Chemical characterization of an alkali-like superatom consisting of a Ta-encapsulating Si<sub>16</sub> cage}. Copyright {2015} American Chemical Society.

elucidates that Ta@Si<sub>16</sub> acquire a high chemical stability against oxidation owing to its metal-encapsulating framework.

#### 4.3.4 Valence band structures

As well as XPS, ultraviolet photoemission spectroscopy (UPS) is a powerful technique to investigate valence electronic states. However, performing UPS with 21.22 eV photons for deposited Ta@Si<sub>16</sub> exhibits no distinct peaks assignable to the electronic states of

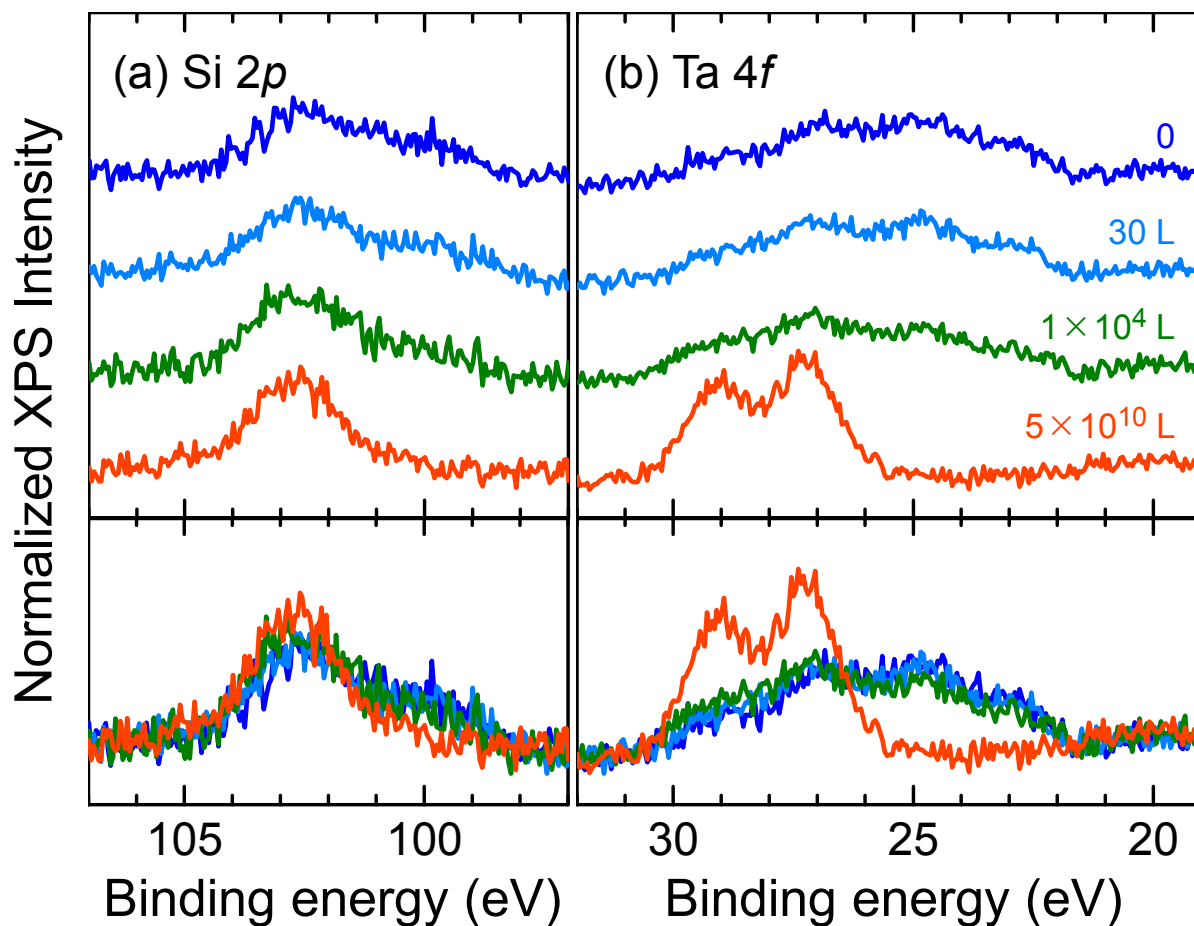


Figure 4.8 XPS spectra for TaSi<sub>3</sub> deposited on HOPG in (a) Si 2*p* and (b) Ta 4*f* levels under the same condition as Figure 4.6, depending on oxygen exposures in the range 0–5 × 10<sup>10</sup> L. For comparison, all series of spectra are superimposed in the bottom of each figure. Reprinted with permission from {Shibuta, M.; Ohta, T.; Nakaya, M.; Tsunoyama, H.; Eguchi, T.; Nakajima, A. Chemical characterization of an alkali-like superatom consisting of a Ta-encapsulating Si<sub>16</sub> cage}. Copyright {2015} American Chemical Society.

Ta@Si<sub>16</sub> either on HOPG or on C<sub>60</sub>/HOPG, as shown in Figure 4.9. With the deposition of Ta@Si<sub>16</sub> onto C<sub>60</sub>/HOPG, the C<sub>60</sub>-derived peaks show a small energy shift of 0.2 eV toward the Fermi level and a new broad component in the low-energy region. Since similar spectral changes have been observed in the UPS spectra for a sodium (Na)-

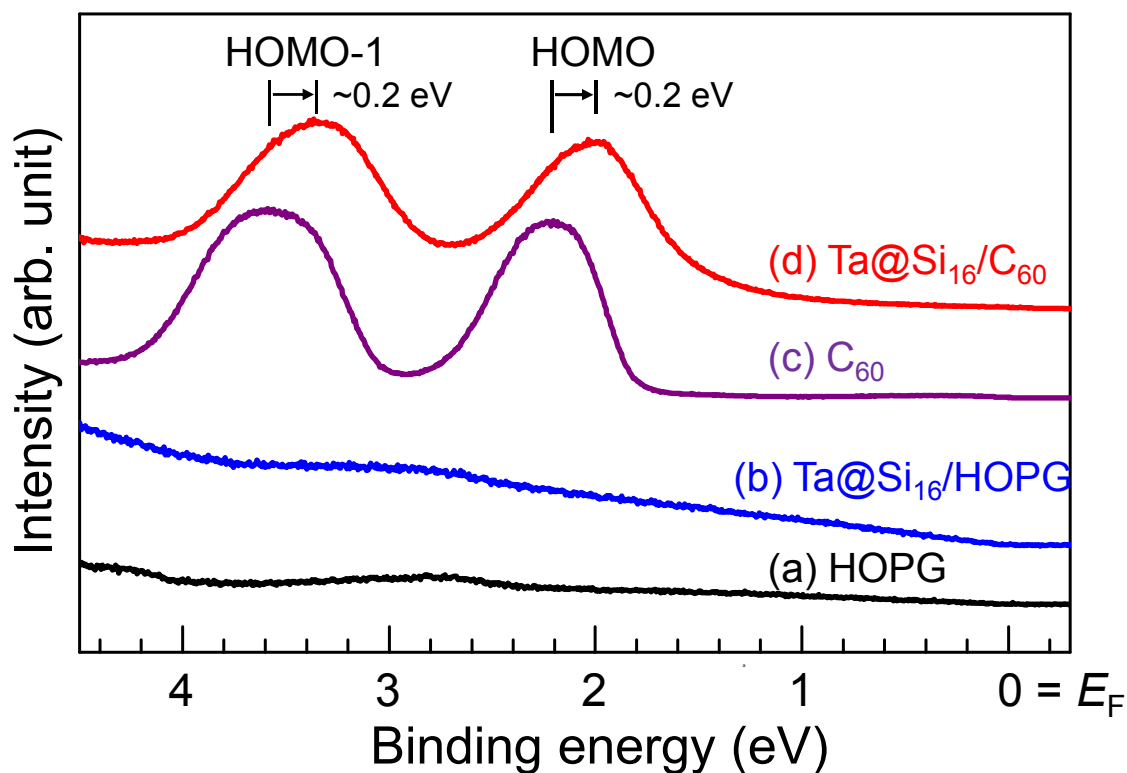


Figure 4.9 Valence (UPS) spectra for (a) HOPG, (b) Ta@Si<sub>16</sub>/HOPG, (c) C<sub>60</sub> monolayer, and (d) Ta@Si<sub>16</sub> on C<sub>60</sub>/HOPG. Reprinted with permission from {Shibuta, M.; Ohta, T.; Nakaya, M.; Tsunoyama, H.; Eguchi, T.; Nakajima, A. Chemical characterization of an alkali-like superatom consisting of a Ta-encapsulating Si<sub>16</sub> cage}. Copyright {2015} American Chemical Society.

doped C<sub>60</sub> film,<sup>[40]</sup> the spectral changes may suggest the alkali-like superatom behavior of Ta@Si<sub>16</sub>. Recently, Claes *et al.* studied the infrared multiple photon dissociation (IR-MPD) spectrum of Si<sub>16</sub>V<sup>+</sup> and reported that the IR-MPD spectrum is very different from those of other Si<sub>*n*</sub>V<sup>+</sup> (*n* = 12–15).<sup>[21]</sup> It shows no distinct, narrow absorption peaks but has a couple of broad features. Using a molecular dynamics simulation, indeed, they suggest that Si<sub>16</sub>V<sup>+</sup> is dynamic, undergoing rapid transitions between nearly degenerate local minima. The dynamic behavior for Si<sub>16</sub>V<sup>+</sup> might be consistent with no distinct

peaks in the UPS in this study because fluctuating structures of  $\text{Si}_{16}\text{Ta}^+$  would not exhibit any stationary electronic states.

## 4.4 Conclusions

The chemical states and stability of Ta@Si16 deposited on a HOPG have been evaluated by XPS, revealing a uniform chemical state of the relevant elements. Combining these data with evidence of a low reactivity toward oxygen exposure proves that the metal-encapsulating cage of Ta@Si<sub>16</sub> has been maintained after deposition onto the substrate, a situation which is also supported by the STM. The chemical robustness of M@Si<sub>16</sub> nanoclusters will enable us to construct novel devices utilizing their unique properties as superatoms. We expect these experimental findings to greatly contribute to the opening up of a new field of nanomaterial science based on superatom assembly through functionalities that emerge from an atomic scale interaction among naked superatomic nanoclusters.

## References

- [1] S. Khanna and P. Jena. “Assembling crystals from clusters”. *Phys. Rev. Lett.*, **1992**, 69(11), 1664.
- [2] R. M. Crooks, M. Zhao, L. Sun, V. Chechik and L. K. Yeung. “Dendrimer-encapsulated metal nanoparticles: synthesis, characterization, and applications to catalysis”. *Acc. Chem. Res.*, **2001**, 34(3), 181–190.
- [3] J. Zheng and R. M. Dickson. “Individual water-soluble dendrimer-encapsulated silver nanodot fluorescence”. *J. Am. Chem. Soc.*, **2002**, 124(47), 13982–13983.
- [4] S. B. Darling, N. A. Yufa, A. L. Cisse, S. D. Bader and S. J. Sibener. “Self-organization of FePt nanoparticles on photochemically modified diblock copolymer templates”. *Adv. Mater.*, **2005**, 17(20), 2446–2450.
- [5] A. Castleman and P. Jena. “Clusters: A bridge across the disciplines of environment, materials science, and biology”. *Proc. Natl. Acad. Sci. U. S. A.*, **2006**, 103(28), 10554–10559.
- [6] S. A. Claridge, A. Castleman Jr, S. N. Khanna, C. B. Murray, A. Sen and P. S. Weiss. “Cluster-assembled materials”. *ACS Nano*, **2009**, 3(2), 244–255.
- [7] A. Castleman Jr and S. Khanna. “Clusters, superatoms, and building blocks of new materials”. *J. Phys. Chem. C*, **2009**, 113(7), 2664–2675.
- [8] R. Jin. “Quantum sized, thiolate-protected gold nanoclusters”. *Nanoscale*, **2010**, 2(3), 343–362.
- [9] Y. H. Jang, K. Chung, L. N. Quan, B. Špačková, H. Šípová, S. Moon, W. J. Cho,

- H.-Y. Shin, Y. J. Jang, J.-E. Lee, et al. “Configuration-controlled Au nanocluster arrays on inverse micelle nano-patterns: versatile platforms for SERS and SPR sensors”. *Nanoscale*, **2013**, 5(24), 12261–12271.
- [10] X. Roy, C.-H. Lee, A. C. Crowther, C. L. Schenck, T. Besara, R. A. Lalancette, T. Siegrist, P. W. Stephens, L. E. Brus, P. Kim, et al. “Nanoscale atoms in solid-state chemistry”. *Science*, **2013**, 341(6142), 157–160.
- [11] H. W. Kroto, J. R. Heath, S. C. O’Brien, R. F. Curl, R. E. Smalley, et al. “C<sub>60</sub>: buckminsterfullerene”. *Nature*, **1985**, 318(6042), 162–163.
- [12] H.-J. Zhai, Y.-F. Zhao, W.-L. Li, Q. Chen, H. Bai, H.-S. Hu, Z. A. Piazza, W.-J. Tian, H.-G. Lu, Y.-B. Wu, et al. “Observation of an all-boron fullerene”. *Nat. Chem.*, **2014**, 6(8), 727–731.
- [13] S. M. Beck. “Mixed metal–silicon clusters formed by chemical reaction in a supersonic molecular beam: implications for reactions at the metal/silicon interface”. *J. Chem. Phys.*, **1989**, 90(11), 6306–6312.
- [14] V. Kumar and Y. Kawazoe. “Metal-encapsulated fullerenelike and cubic caged clusters of silicon”. *Phys. Rev. Lett.*, **2001**, 87(4), 045503.
- [15] K. Koyasu, M. Akutsu, M. Mitsui and A. Nakajima. “Selective Formation of MSi<sub>16</sub> (M= Sc, Ti, and V)”. *J. Am. Chem. Soc.*, **2005**, 127(14), 4998–4999.
- [16] J. U. Reveles and S. N. Khanna. “Electronic counting rules for the stability of metal-silicon clusters”. *Phys. Rev. B*, **2006**, 74(3), 035435.
- [17] K. Koyasu, J. Atobe, M. Akutsu, M. Mitsui and A. Nakajima. “Electronic and geometric stabilities of clusters with transition metal encapsulated by silicon”. *J. Phys. Chem. A*, **2007**, 111(1), 42–49.

- [18] M. Torres, E. Fernández and L. Balbás. “Theoretical study of isoelectronic  $\text{Si}_n\text{M}$  clusters ( $\text{M} = \text{Sc}^-, \text{Ti}, \text{V}^+; n = 14\text{--}18$ )”. *Phys. Rev. B*, **2007**, 75(20), 205425.
- [19] J. Lau, K. Hirsch, P. Klar, A. Langenberg, F. Lofink, R. Richter, J. Rittmann, M. Vogel, V. Zamudio-Bayer, T. Möller, et al. “X-ray spectroscopy reveals high symmetry and electronic shell structure of transition-metal-doped silicon clusters”. *Phys. Rev. A*, **2009**, 79(5), 053201.
- [20] H. Cantera-López, L. Balbás and G. Borstel. “First-principles calculations of structural and electronic properties of Ta-doped Si clusters, wires, and bulk systems”. *Phys. Rev. B*, **2011**, 83(7), 075434.
- [21] P. Claes, E. Janssens, V. Ngan, P. Gruene, J. T. Lyon, D. J. Harding, A. Fielicke, M. Nguyen and P. Lievens. “Structural identification of caged vanadium doped silicon clusters”. *Phys. Rev. Lett.*, **2011**, 107(17), 173401.
- [22] J. Lau, M. Vogel, A. Langenberg, K. Hirsch, J. Rittmann, V. Zamudio-Bayer, T. Möller and B. Von Issendorff. “Communication: Highest occupied molecular orbital–lowest unoccupied molecular orbital gaps of doped silicon clusters from core level spectroscopy”. *J. Chem. Phys.*, **2011**, 134(4), 041102.
- [23] J. Atobe, K. Koyasu, S. Furuse and A. Nakajima. “Anion photoelectron spectroscopy of germanium and tin clusters containing a transition-or lanthanide-metal atom;  $\text{MGe}_n^-(n = 8\text{--}20)$  and  $\text{MSn}_n^-(n = 15\text{--}17)$  ( $\text{M} = \text{Sc}\text{--}\text{V}, \text{Y}\text{--}\text{Nb}, \text{and Lu}\text{--}\text{Ta}$ )”. *Phys. Chem. Chem. Phys.*, **2012**, 14(26), 9403–9410.
- [24] A. Nakajima, T. Kishi, T. Sugioka and K. Kaya. “Electronic and geometric structures of aluminum-boron negative cluster ions ( $\text{Al}_n\text{B}_m^-$ )”. *Chem. Phys. Lett.*, **1991**, 187(3), 239–244.

- [25] X. Li and L.-S. Wang. “Experimental search and characterization of icosahedral clusters:  $\text{Al}_{12}\text{X}^-$  ( $\text{X} = \text{C}, \text{Ge}, \text{Sn}, \text{Pb}$ )”. *Phys. Rev. B*, **2002**, 65(15), 153404.
- [26] H.-J. Zhai, J. Li and L.-S. Wang. “Icosahedral gold cage clusters:  $\text{M}@\text{Au}_{12}^-$  ( $\text{M} = \text{V}, \text{Nb}, \text{and Ta}$ )”. *J. Chem. Phys.*, **2004**, 121(17), 8369–8374.
- [27] L.-F. Cui, X. Huang, L.-M. Wang, J. Li and L.-S. Wang. “Endohedral Stannaspherenes  $\text{M}@\text{Sn}_{12}^-$ : A Rich Class of Stable Molecular Cage Clusters”. *Angew. Chem.*, **2007**, 119(5), 756–759.
- [28] T. Iwasa and A. Nakajima. “Geometric, electronic, and optical properties of a superatomic heterodimer and trimer:  $\text{Sc}@\text{Si}_{16}-\text{V}@\text{Si}_{16}$  and  $\text{Sc}@\text{Si}_{16}-\text{Ti}@\text{Si}_{16}-\text{V}@\text{Si}_{16}$ ”. *J. Phys. Chem. C*, **2012**, 116(26), 14071–14077.
- [29] M. Nakaya, T. Iwasa, H. Tsunoyama, T. Eguchi and A. Nakajima. “Formation of a superatom monolayer using gas-phase-synthesized  $\text{Ta}@\text{Si}_{16}$  nanocluster ions”. *Nanoscale*, **2014**, 6(24), 14702–14707.
- [30] M. Nakaya, T. Iwasa, H. Tsunoyama, T. Eguchi and A. Nakajima. “Heterodimerization via the Covalent Bonding of  $\text{Ta}@\text{Si}_{16}$  Nanoclusters and  $\text{C}_{60}$  Molecules”. *J. Phys. Chem. C*, **2015**, 119(20), 10962–10968.
- [31] J. H. Scofield. “Hartree-Slater subshell photoionization cross-sections at 1254 and 1487 eV”. *J. Electron Spectrosc. Relat. Phenom.*, **1976**, 8(2), 129–137.
- [32] T. Ohta, M. Shibuta, H. Tsunoyama, Y. Negishi, T. Eguchi and A. Nakajima. “Size and structure dependence of electronic states in thiolate-protected gold nanoclusters of  $\text{Au}_{25}(\text{SR})_{18}$ ,  $\text{Au}_{38}(\text{SR})_{24}$ , and  $\text{Au}_{144}(\text{SR})_{60}$ ”. *J. Phys. Chem. C*, **2013**, 117(7), 3674–3679.
- [33] G. Rangelov and T. Fauster. “Thermally-induced evolution of codeposited Co–Si

- layers on Si (100) surfaces”. *Surf. Sci.*, **1996**, 365(2), 403–410.
- [34] D. M. Riffe and G. Wertheim. “Ta(110) surface and subsurface core-level shifts and  $4f_{7/2}$  line shapes”. *Phys. Rev. B*, **1993**, 47(11), 6672.
- [35] G. Hollinger, J. Morar, F. Himpsel, G. Hughes and J. Jordan. “Si(111) surface oxidation: O 1s core-level study using synchrotron radiation”. *Surf. Sci.*, **1986**, 168(1), 609–616.
- [36] J. Thomas and L. Hammer. “A Photoelectron Spectroscopy Study of  $\text{CF}_4/\text{H}_2$  Reactive Ion Etching Residue on Tantalum Disilicide”. *J. Electrochem. Soc.*, **1989**, 136(7), 2004–2010.
- [37] I. Kusunoki and Y. Igari. “XPS study of a SiC film produced on Si(100) by reaction with a  $\text{C}_2\text{H}_2$  beam”. *Appl. Surf. Sci.*, **1992**, 59(2), 95–104.
- [38] L. Ley, J. Reichardt and R. Johnson. “Static charge fluctuations in amorphous silicon”. *Phys. Rev. Lett.*, **1982**, 49(22), 1664.
- [39] J. V. d. Veen, F. Himpsel and D. Eastman. “Chemisorption-induced  $4f$ -core-electron binding-energy shifts for surface atoms of W(111), W(100), and Ta(111)”. *Phys. Rev. B*, **1982**, 25(12), 7388.
- [40] C. Gu, F. Stepniak, D. Poirier, M. Jost, P. Benning, Y. Chen, T. Ohno, J. L. Martins, J. Weaver, J. Fure, et al. “Metallic and insulating phases of  $\text{Li}_x\text{C}_{60}$ ,  $\text{Na}_x\text{C}_{60}$ , and  $\text{Rb}_x\text{C}_{60}$ ”. *Phys. Rev. B*, **1992**, 45(11), 6348.

## Chapter 5

# Charge Transfer Complexation of

# Ta-Encapsulating Superatom

# Ta@Si<sub>16</sub> with C<sub>60</sub>

## 5.1 Introduction

Nanoclusters consisting of several to several hundreds of atoms have recently emerged as promising building blocks for functional materials implemented to next-generation chemical and electronic devices.<sup>[1-5]</sup> Specifically, metal-encapsulating  $\text{Si}_{16}$  caged nanoclusters ( $\text{M@Si}_{16}$ ) have attracted a great deal of attention because their electronic properties can be precisely tuned by changing the central metal atom following the silicon-based material science.<sup>[6-11]</sup> Because of their 68 electron closed-shell structure,  $\text{M@Si}_{16}$  nanoclusters containing a group 4 metal atom ( $\text{M} = \text{Ti}, \text{Zr}, \text{and Hf}$ ), for which each silicon atom bears four valence electrons, exhibit rare-gas-like superatom behaviors.<sup>[1,6-8,12-14]</sup> Their group 3 ( $\text{M} = \text{Sc}, \text{Y}, \text{and Lu}$ ) and group 5 ( $\text{M} = \text{V}, \text{Nb}, \text{and Ta}$ ) nanoclusters show halogen- and alkali-like nature, respectively, because the excess or missing electron satisfies the electronic closed-shell structure.<sup>[8,12,13]</sup>

In order to utilize these nanocluster superatoms for functional materials applications, the halogen- or alkali-like superatoms prefer a counter material to produce a more stable compound via charge transfer (CT).<sup>[10]</sup> Surrounding the nanocluster core by a protective ligand outer layer is one plausible strategy. In fact, numerous charged metal nanoclusters have been successfully synthesized and isolated by stabilization using electron accepting or donating ligands in the liquid phase.<sup>[4,5,15-17]</sup>

In contrast, their assembly or aggregate as “naked” nanoclusters are considered very important for material science applications utilizing their superatomic nature, because ligand protection may significantly modify their original properties. Vacuum deposition

onto a substrate offers a workable technique for the treatment and isolation of naked nanoclusters synthesized in the gas phase. In addition, the interaction between the nanocluster and the substrate should be designed to achieve their immobilization in a monodispersed manner. When deposited on chemically inert highly oriented pyrolytic graphite (HOPG), alkali-like Ta@Si<sub>16</sub> nanocluster superatoms diffuse on the surface and aggregate with each other while maintaining their unique chemical and thermal robustness.<sup>[18]</sup>

Molecular films may provide substrates that immobilize the nanoclusters by superatom-molecule complex formation without surface diffusion or aggregation. Nakaya *et al.* have recently observed an individual alkali-like Ta@Si<sub>16</sub> nanocluster on ordered electron-acceptable C<sub>60</sub> molecular film by scanning tunneling microscopy (STM),<sup>[19]</sup> consistent with nanocluster immobilization. Furthermore, Ta@Si<sub>16</sub> readily forms the stoichiometric one-to-one Ta@Si<sub>16</sub>C<sub>60</sub> complex on C<sub>60</sub> films.<sup>[19,20]</sup> If this hypothesis is right, it may give us an approach to choose an appropriate substrate for immobilizing M@Si<sub>16</sub> superatoms. Although the chemical states of Ta@Si<sub>16</sub> on C<sub>60</sub>/HOPG was estimated by comparing its HOMO-LUMO gap with theoretical results, its exact chemical state, which is crucial for the treatment of M@Si<sub>16</sub> nanocluster-based CT complexes stabilized by counter molecules, remains unclear.

In this study, the chemical states of Ta@Si<sub>16</sub> nanocluster superatom deposited on a C<sub>60</sub> film were determined by X-ray photoelectron spectroscopy (XPS) and ultraviolet photoelectron spectroscopy (UPS). Typically, XPS provides inner core levels to describe the chemical environment while UPS unveils a valence electronic structure just below Fermi level ( $E_F$ ), which is sensitively relevant to chemical bond formation. These mea-

measurements revealed that the Ta@Si<sub>16</sub> nanocluster generated a new CT complex with C<sub>60</sub> fullerene via one electron transfer. Moreover, the (Ta@Si<sub>16</sub>)<sup>+</sup>C<sub>60</sub><sup>-</sup> CT complex and oxides of Ta@Si<sub>16</sub> displayed high thermal and chemical robustness after heating or oxygen exposure.

## 5.2 Experiment

The apparatus and principle of nanocluster generation and photoelectron spectroscopy were described in Chapter 2. In this section, the experimental manipulation of sample preparation is explained.

Briefly, prior to the Ta@Si<sub>16</sub> nanocluster deposition, a HOPG surface was cleaned by cleaving in atmosphere and heating (750 K, >50 h) in ultrahigh vacuum (UHV, <2 × 10<sup>-8</sup> Pa) and coated with a C<sub>60</sub> film using a Knudsen effusion cell. The C<sub>60</sub> film thickness and growth speed were set to two monolayers (MLs) and 0.07 ML/min, respectively, under quartz crystal microbalance monitoring. The Ta@Si<sub>16</sub> nanoclusters were generated by magnetron sputtering using a Ta-Si alloy target and Ar<sup>+</sup> ions at the cluster ion source.

By optimizing the condition of the nanocluster synthesis, the Ta@Si<sub>16</sub><sup>+</sup> cations were selectively generated owing to its geometric and electronic stability (68 electrons). They were also selectively deposited onto the C<sub>60</sub> film by fixing the quadrupole mass filter at an  $m/z$  value of 630 with a mass resolution ( $m/\Delta m$ ) of about 50. The collision energy of nanoclusters toward the C<sub>60</sub> film was kept as low as possible (ca. 5 eV) to avoid nanocluster destruction and penetration. Deposition time and average ion current were

set to 150 min and 510 pA, respectively, which corresponds to  $2.9 \times 10^{13}$  nanoclusters in total. Assuming a deposition area of  $2.8 \times 10^{13} \text{ nm}^2$  (6 mm in diameter) and a Ta@Si<sub>16</sub> diameter of 0.8–0.9 nm,<sup>[19]</sup> the nanocluster coverage was estimated to be 1 ML.

The deposited sample was transferred to an XPS and UPS system connected with the nanocluster deposition system under UHV conditions and exposed to X-ray (Mg K $\alpha$ ; photon energy ( $h\nu$ ) = 1253.6 eV) or vacuum ultraviolet irradiation (He I $\alpha$ ;  $h\nu$  = 21.22 eV). Photoelectrons were detected using a hemispherical electron analyzer (VG SCIENTA, R-3000) for XPS and UPS photoemission angles of 45° and 0° with respect to the surface normal, respectively. In the XPS analysis, the instrumental broadening of core level was considered as a Voigt function (full widths at half maximum (FWHMs) amounted to 1.09 eV, for which Gaussian and Lorentzian components equaled 0.75 and 0.56 eV, respectively) determined from a peak analysis of Au 4*f* core level for a reference Au(111) surface described in Chapter 3.<sup>[21]</sup> XPS and UPS measurements were performed at room temperature for the substrate prepared without or with heating treatments.

## 5.3 Results

### 5.3.1 XPS spectra of Ta@Si<sub>16</sub> deposited on a C<sub>60</sub> film

Figure 5.1 shows the XPS spectra of (a) Si 2*p* and (b) Ta 4*f* core levels for Ta@Si<sub>16</sub> deposited on the C<sub>60</sub> film (Ta@Si<sub>16</sub>/C<sub>60</sub>/HOPG). Figure 5.2 shows C 1*s* core levels for bare HOPG (bottom), HOPG coated with a 2 ML-C<sub>60</sub> film (C<sub>60</sub>/HOPG, middle), and Ta@Si<sub>16</sub>/C<sub>60</sub>/HOPG (top). In these spectra, the horizontal axis corresponds to the binding energy relative to the Fermi level,  $E_F$ .

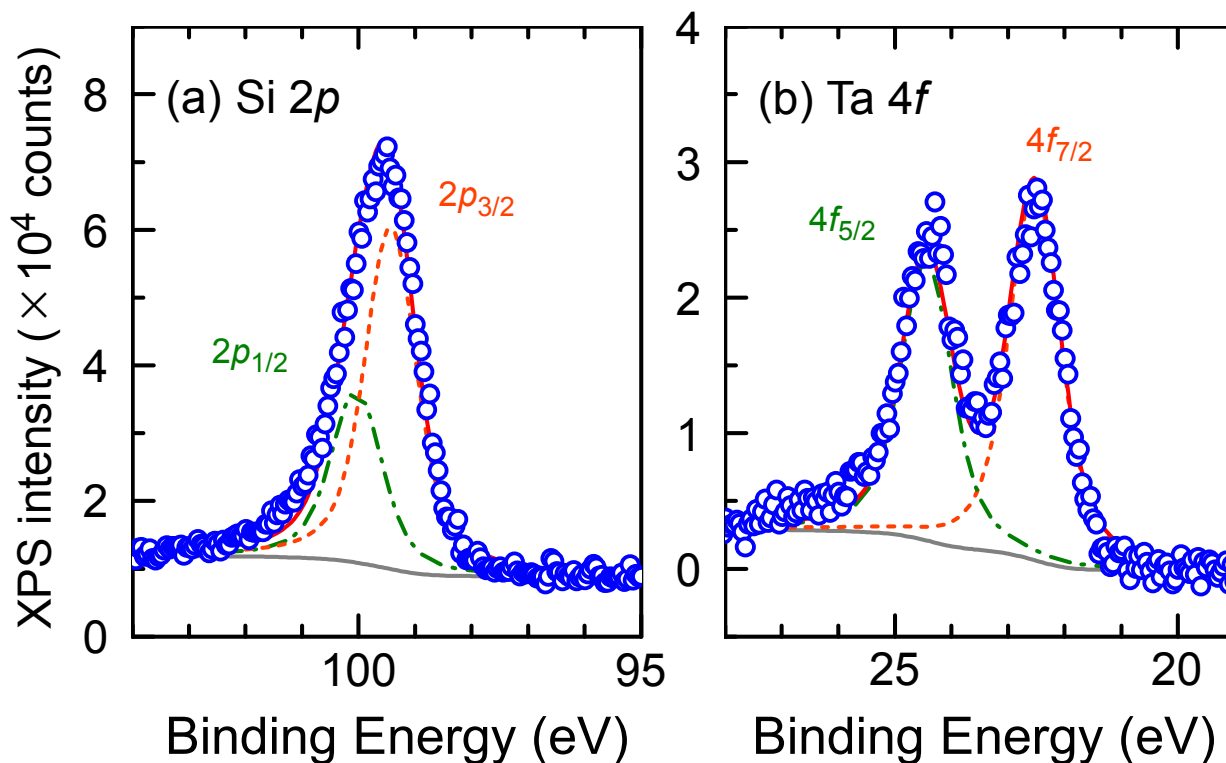


Figure 5.1 XPS spectra of (a) Si  $2p$  and (b) Ta  $4f$  for Ta@Si<sub>16</sub>/C<sub>60</sub>/HOPG. Fitted results (red line) and spin-orbit contributions (orange dotted and green dash-dotted lines) are superimposed. In the fitting procedure, energy separations and branching ratios were set to 0.6 eV, 1:2 for Si  $2p$  and 1.9 eV, 3:4 for Ta  $4f$ , respectively.<sup>[22,23]</sup> Reprinted with permission from {Ohta, T.; Shibuta, M.; Tsunoyama, H.; Eguchi, T.; Nakajima, A. Charge transfer complexation of Ta-encapsulating Ta@Si<sub>16</sub> superatom with C<sub>60</sub>}. Copyright {2016} American Chemical Society.

Both Si  $2p$  and Ta  $4f$  derived core level signals observed for the Ta@Si<sub>16</sub>-covered C<sub>60</sub> film presented adequate intensities for chemical analysis. Their integrated intensity ratio between Ta  $4f$  and Si  $2p$  signals after a subtraction of Shirley background (gray line) is **図 チオラート保護金クラスターの構造** 1:1.57. This ratio agreed well with the simulated value (1:1.53), which was calculated based on a corresponding atomic composition ratio of 1:16 and photoemission cross-sections for both core levels.<sup>[18,24]</sup> This agreement indicates that generated Ta@Si<sub>16</sub>

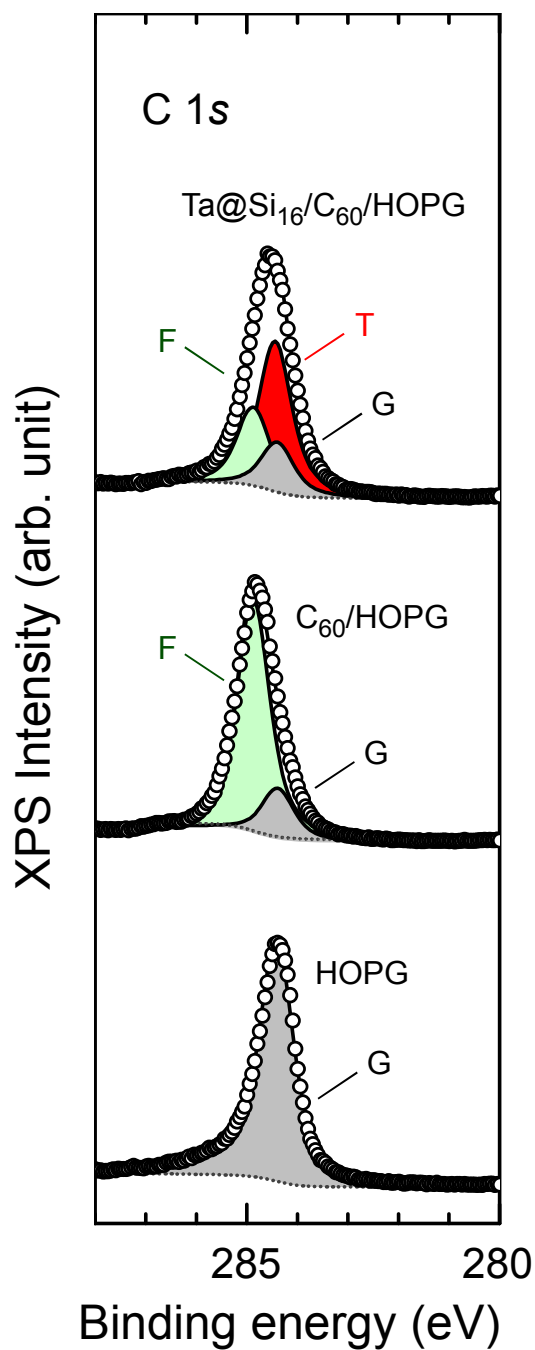


Figure 5.2 XPS spectra of C 1s for Ta@Si<sub>16</sub>/C<sub>60</sub>/HOPG (top), C<sub>60</sub>/HOPG (middle), and HOPG (bottom) were fitted using three components labeled by G, F, and T (see text) after Shirley background subtraction (gray dotted line) Reprinted with permission from {Ohta, T.; Shibuta, M.; Tsunoyama, H.; Eguchi, T.; Nakajima, A. Charge transfer complexation of Ta-encapsulating Ta@Si<sub>16</sub> superatom with C<sub>60</sub>}. Copyright {2016} American Chemical Society.

nanoclusters successfully deposited on the  $C_{60}$  film with mass selection.

The chemical states of deposited  $Ta@Si_{16}$  were characterized by spectral deconvolution using the instrumental broadening of the Voigt function. Moreover, energy separations and branching ratios resulting from the spin-orbit splittings of Si  $2p_{3/2,1/2}$  and Ta  $4f_{7/2,5/2}$  were set the literature values.<sup>[22, 23]</sup> The fitted results (red lines, Figures 5.1(a) and (b)) show that the experimental data for Ta and Si atoms can be favorably reproduced by assuming a single chemical environment for each atom. These results revealed that the Ta-encapsulating  $Si_{16}$  cage kept its original framework on the  $C_{60}$  film. Therefore, all sixteen Si atoms are isotropically distributed around the central Ta atom.

Moreover, the binding energies of core levels provided information on the charge states of the  $C_{60}$ -supported  $Ta@Si_{16}$ . These binding energies equaled 99.4 and 22.5 eV for Si  $2p_{3/2}$  and Ta  $4f_{7/2}$  core levels, respectively. The binding energy of Ta  $4f_{7/2}$  is 0.9 eV higher than that of bulk ( $Ta^0$ : 21.6 eV);<sup>[22]</sup> while the binding energy of Si  $2p_{3/2}$  is almost the same in that of bulk ( $Si^0$ ) within the scattered reported data (99.0–100.0 eV depending on the dopant).<sup>[24, 25]</sup> Reported Ta  $4f_{7/2}$  and Si  $2p_{3/2}$  core level energy shifts amounted to 0.9 and 1.0 eV for  $Ta^{1+}$ <sup>[26]</sup> and  $Si^{1+}$ ,<sup>[27–29]</sup> respectively. These results indicate that the central Ta atom in the  $Ta@Si_{16}$  is positively charged like a  $Ta^{1+}$  while the surrounding Si atoms are neutral, and therefore the overall charge state of  $Ta@Si_{16}$  superatom is monocationic, i.e.  $(Ta@Si_{16})^+$ .

Based on the principle of 68 electron shell closure,<sup>[12–14]</sup> the  $Ta@Si_{16}$  nanocluster exhibits an alkali-like superatomic behavior, which promotes the release of one electron to produce the electronically stabilized monocation  $(Ta@Si_{16})^+$ . From the stoichiometric

viewpoint, indeed, previous STM results have shown that the uppermost  $C_{60}$  molecules provided a favorable adsorption site at deposition densities approximating 1 ML,<sup>[20]</sup> suggesting that  $Ta@Si_{16}$  interacted with  $C_{60}$  in a one-to-one manner. Since  $C_{60}$  displays high electron acceptability,<sup>[30]</sup> the deposited  $Ta@Si_{16}$  may be stabilized by formation of a superatomic CT complex of  $(Ta@Si_{16})^+C_{60}^-$ .

Concurrently, the XPS analysis for C 1s showed that the counter molecule  $C_{60}$  adopted a monoanionic charge state. First, the C 1s peak was analyzed for bare HOPG and 2 ML  $C_{60}$ /HOPG. A graphite-derived C 1s peak typically fits an asymmetric Voigt function (Doniach-Sunjic line shape with a singularity index) while its  $C_{60}$ -derived peak matches a symmetric Voigt function.<sup>[31]</sup> The XPS signal obtained for HOPG (area G) was fitted with an asymmetric peak at 284.4 eV (Figure 5.2, bottom). After fixing the peak shape and energy position of G, the C 1s peak component derived from pristine  $C_{60}$  film was extracted as a symmetric peak (area F) with Voigt function by deconvolution of the spectrum acquired for the 2 ML  $C_{60}$  film (Figure 5.2, middle). The fitted binding energy (284.8 eV) agreed well with literature values<sup>[32]</sup> while the area ratio between F and G amounted to 5.88:1.

The  $Ta@Si_{16}$  deposition on the  $C_{60}$  film (Figure 5.2, top) substantially broadened the C 1s peak, suggesting that an additional spectral component appeared at a lower binding energy. This additional chemical component should correspond to the photoemission from  $C_{60}$  molecules interacting with the deposited  $Ta@Si_{16}$  ( $(Ta@Si_{16})^+C_{60}^-$ : area T), as schematically illustrated in Figure 5.3; the energy position was 284.4 eV. Despite the considerable energetic overlap between components T and G, the fit was achieved by fixing the area ratio between  $C_{60}$  (F + T) and HOPG (G) derived signals to 5.88:1, which

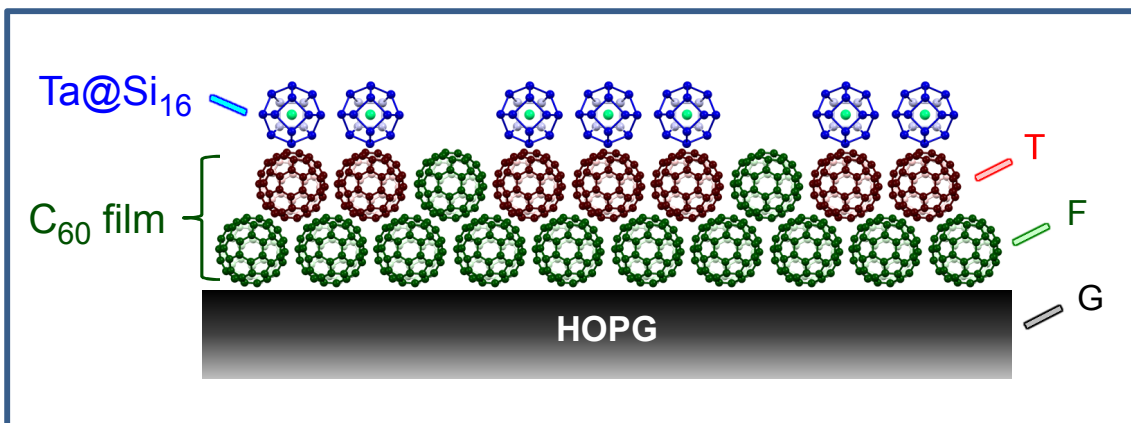


Figure 5.3 A schematic illustration of the cross-sectional view for Ta@Si<sub>16</sub>/2 ML-C<sub>60</sub>/HOPG. Reprinted with permission from {Ohta, T.; Shibuta, M.; Tsunoyama, H.; Eguchi, T.; Nakajima, A. Charge transfer complexation of Ta-encapsulating Ta@Si<sub>16</sub> superatom with C<sub>60</sub>}. Copyright {2016} American Chemical Society.

was determined from the XPS analysis of pristine C<sub>60</sub> film (Figure 5.2, middle). The evaluated intensity ratio amounted to 1.93:3.95 (=1:2.05) between F and T, giving rise to a F:T:G ratio of 1.93:3.95:1. As illustrated in Figure 5.3, the deposition of Ta@Si<sub>16</sub> (1 ML) on the 2 ML C<sub>60</sub> film chemically modified all topmost C<sub>60</sub> molecules, generating one C<sub>60</sub><sup>-</sup> layer (top) over a neutral C<sub>60</sub> layer (bottom). The estimated intensity ratio was 1:2.05 between F and T by accounting for the inelastic mean free path of electron in solid C<sub>60</sub> (2.15 nm),<sup>[33]</sup> in good agreement with the evaluated ratio. This suggests that the two-layered structure of C<sub>60</sub> is formed as shown in Figure 5.3, consistent with the STM measurements.<sup>[19]</sup>

Since component T displayed 0.4 eV lower binding energy than F, the C<sub>60</sub> molecule complexed with Ta@Si<sub>16</sub> exhibited a negative charge. The degree of electron transfer was quantified by comparing the XPS results with previous data for C<sub>60</sub> monolayer films deposited on noble metal substrates. A 1 ML C<sub>60</sub> film formed on Au substrate exhibited a C 1s peak at lower binding energy than that of multilayered C<sub>60</sub> films. When one

electron ( $1 e^-$ ) was transferred from the substrate to  $C_{60}$ ,<sup>[34–39]</sup> the C 1s peak appeared at about 0.4 eV lower binding energy than for neutral  $C_{60}$  in multilayered  $C_{60}$  films. Therefore, the difference in binding energy observed between F and T (0.4 eV) implies that T corresponds to the monoanionic state  $C_{60}^-$ . Interestingly, the binding energy of C 1s peak for  $C_{60}$  film on HOPG is independent of the coverage, showing negligible CT between substrate and  $C_{60}$  molecules.

Overall, these analyses of C 1s for the  $C_{60}$  film substrate as well as Si 2p and Ta 4f for deposited Ta@Si<sub>16</sub> suggest that the deposited Ta@Si<sub>16</sub> nanocluster associates with  $C_{60}$  to form a one-to-one CT complex consistent with the superatomic alkali fulleride (Ta@Si<sub>16</sub>)<sup>+</sup> $C_{60}^-$  at the surface. In fact, when the Ta@Si<sub>16</sub> nanocluster was deposited on bare HOPG, which acted as a chemically inert substrate, no additional spectral component (such as T in Figure 5.2) was observed. Figure 5.4 shows the C 1s XPS spectra of HOPG before (black) and after Ta@Si<sub>16</sub> deposition (red). The binding energy and peak width remained unchanged upon Ta@Si<sub>16</sub> deposition, indicating the absence of chemical interactions between deposited Ta@Si<sub>16</sub> and HOPG.

### 5.3.2 Heating effect

As expected, the formation of CT complex stabilized the generated nanocluster superatom on the surface. Figures 5.5(a) and (b) show the influence of heating on the XPS spectra of Si 2p and Ta 4f core levels for Ta@Si<sub>16</sub> deposited on  $C_{60}$  (Ta@Si<sub>16</sub>/ $C_{60}$ /HOPG) films, respectively. Each spectrum was subjected to a Shirley background subtraction. Upon heating at 570 K, both core levels remained almost unchanged except for slight broadening of Si 2p. At 620 K, this broadening became

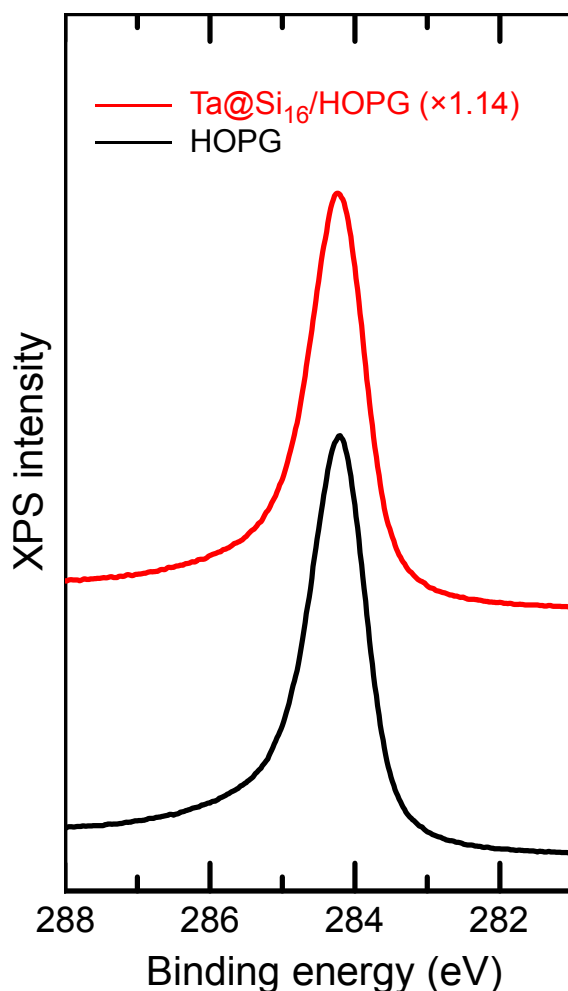


Figure 5.4 XPS spectra of C 1s core levels for HOPG (black) and Ta@Si<sub>16</sub>/HOPG (red). Reprinted with permission from {Ohta, T.; Shibuta, M.; Tsunoyama, H.; Eguchi, T.; Nakajima, A. Charge transfer complexation of Ta-encapsulating Ta@Si<sub>16</sub> superatom with C<sub>60</sub>}. Copyright {2016} American Chemical Society.

more significant, causing a peak assignable to Si<sup>2+</sup> to appear at a binding energy of 102 eV (energy shift: 1.8 eV).<sup>[27–29]</sup> Further heating at 720 K for 16 h enhanced the peak broadening to 102.5 eV, implying that trivalent Si atoms (Si<sup>3+</sup>; energy shift: 2.6 eV) were formed without tetravalent ones (Si<sup>4+</sup>; energy shift: 3.6 ± 0.3 eV).<sup>[27–29]</sup> This strongly suggests that the thermal treatment caused residual oxygen intercalated inside HOPG to exude and react with over-layered (Ta@Si<sub>16</sub>)<sup>+</sup>C<sub>60</sub><sup>-</sup>, producing oxides

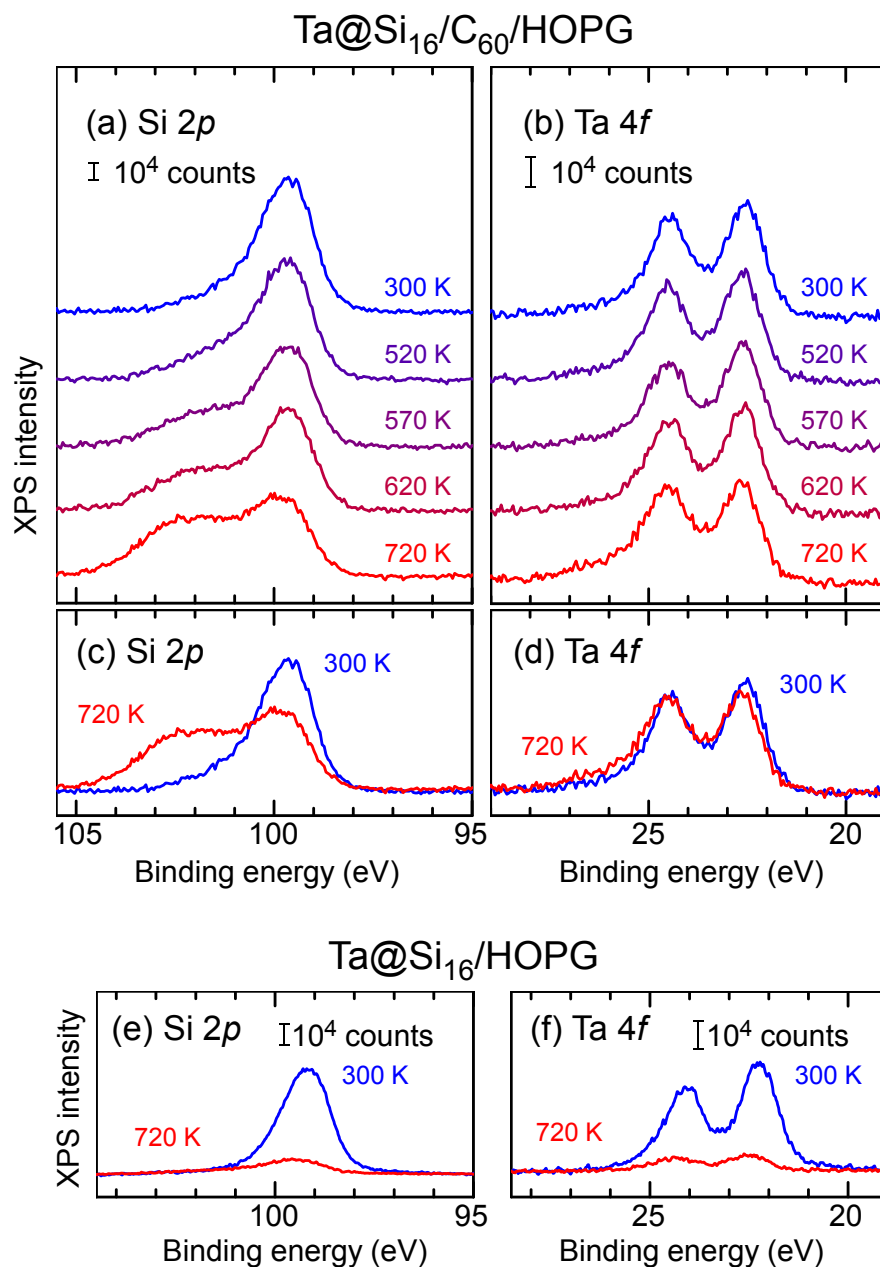


Figure 5.5 XPS spectra of (a) Si 2*p* and (b) Ta 4*f* for Ta@Si<sub>16</sub>/C<sub>60</sub>/HOPG before and after heat treatment. The heating temperatures are noted in the right hand. The spectra at 300 and 720 K in (a) and (b) are overwritten in (c) and (d), respectively. In addition, XPS spectra of (e) Si 2*p* and (f) Ta 4*f* at 300 and 720 K for Ta@Si<sub>16</sub>/HOPG are shown. Reprinted with permission from {Ohta, T.; Shibuta, M.; Tsunoyama, H.; Eguchi, T.; Nakajima, A. Charge transfer complexation of Ta-encapsulating Ta@Si<sub>16</sub> superatom with C<sub>60</sub>}. Copyright {2016} American Chemical Society.

of superatoms. In fac

above 620 K at about

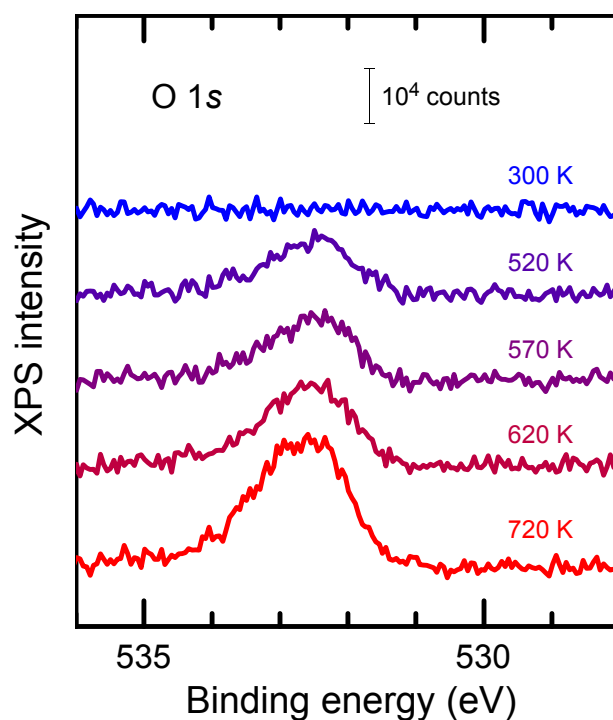


Figure 5.6 XPS spectra of O 1s core levels for Ta@Si<sub>16</sub>/C<sub>60</sub>/HOPG before and after heating. The heating temperatures are shown in the spectra. Reprinted with permission from {Ohta, T.; Shibuta, M.; Tsunoyama, H.; Eguchi, T.; Nakajima, A. Charge transfer complexation of Ta-encapsulating Ta@Si<sub>16</sub> superatom with C<sub>60</sub>}. Copyright {2016} American Chemical Society.

that the O 1s peak position is sensitive to the binding partner because the oxide ion polarizability strongly affects the binding energy.<sup>[40,41]</sup> The result for the O 1s peak at about 532.5 eV well corresponds to that for O atoms bound to Si in SiO<sub>2</sub> (532–533 eV),<sup>[41–43]</sup> while that for O atoms bound to Ta in Ta<sub>2</sub>O<sub>5</sub> appears at lower energy region (530–531 eV).<sup>[43,44]</sup> This suggests that oxygen atoms form a chemical bond with Si atoms as Si=O or Si–O–Si bonds, resulting in a superatom oxide network.

Interestingly, despite the growth of the O 1s with heating, few fully oxidized signals corresponding to Si<sup>4+</sup> were observed (Figure 5.5(a)), indicating that the oxidation of Ta@Si<sub>16</sub> leads to superatom oxide networks without fully oxidized species, such as SiO<sub>2</sub>.

Both bulk Si and Ta surfaces exhibit similar chemical reactivity toward oxygen atoms.<sup>[45]</sup> However, unlike Si 2*p*, Ta 4*f* mostly retained its spectral shape upon heating, even at 720 K for 16 h (Figure 5.5(b)). This result clearly indicates that, despite their partial oxidation, Si atoms surrounded the Ta atom, protecting this central atom. Therefore, the Ta-encapsulating framework with sixteen Si contributed to high robustness against thermal or chemical perturbation.

In the presence of C<sub>60</sub> layers, the XPS spectra for Si 2*p* and Ta 4*f* differed dramatically after heating at 720 K for 16 h. This difference was more obvious in superimposed spectra, shown in Figure 5.5(c) and (d). When Ta@Si<sub>16</sub> was directly deposited onto HOPG, the XPS intensities of both core levels decreased to 1/6 under the same heat treatment conditions (720 K for 16 h) owing to desorption and/or migration of Ta@Si<sub>16</sub> (Figures 5.5(e) and (f)).<sup>[18]</sup> In contrast, these XPS intensities were maintained at 720 K upon introduction of the C<sub>60</sub> molecular film (Figures 5.5(c) and (d)). This difference shows that Ta@Si<sub>16</sub> was tightly fixed to the C<sub>60</sub> surface by forming the (Ta@Si<sub>16</sub>)<sup>+</sup>C<sub>60</sub><sup>-</sup> CT complex.

Figure 5.7 shows the XPS spectra of C 1s for Ta@Si<sub>16</sub>/C<sub>60</sub>/HOPG before and after heating at temperatures ranging between 520 and 720 K. The C 1s peak shifted toward lower binding energy between 520 and 620 K. Despite a difficult peak deconvolution in a similar manner to Figure 5.2, this peak shift may be attributed to the reduction of

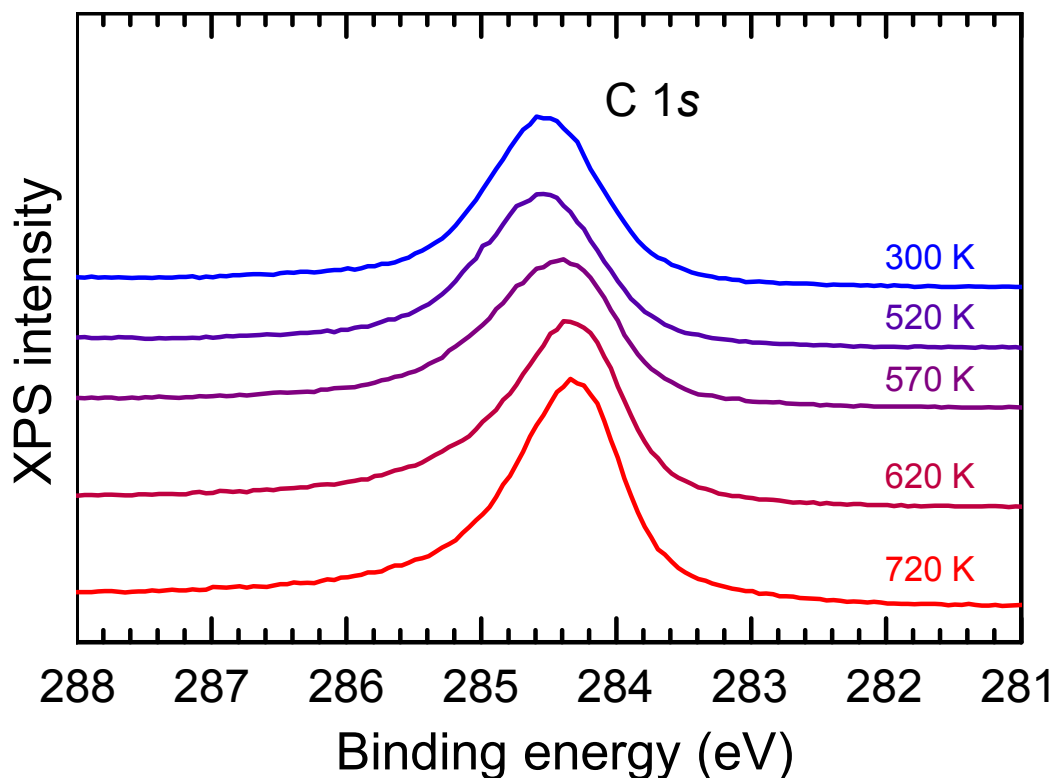


Figure 5.7 XPS spectra of C 1s for Ta@Si<sub>16</sub>/C<sub>60</sub>/HOPG before and after heat treatment. The heating temperatures are noted in the right hand. Reprinted with permission from {Ohta, T.; Shibuta, M.; Tsunoyama, H.; Eguchi, T.; Nakajima, A. Charge transfer complexation of Ta-encapsulating Ta@Si<sub>16</sub> superatom with C<sub>60</sub>}. Copyright {2016} American Chemical Society.

free C<sub>60</sub> molecules.

While the C<sub>60</sub> desorption process cannot be discussed quantitatively from the XPS results, UPS measurements enabled a quantitative assessment of the C<sub>60</sub> desorption because the peaks corresponding to C<sub>60</sub> are detectable. UPS spectra measured before and after thermal treatments confirmed that Ta@Si<sub>16</sub> was attached to the C<sub>60</sub> surface. Figures 5.8(a) and (b) compare the UPS spectra obtained at different substrate temperatures for C<sub>60</sub>/HOPG and Ta@Si<sub>16</sub>/C<sub>60</sub>/HOPG, respectively. At 300 K, two

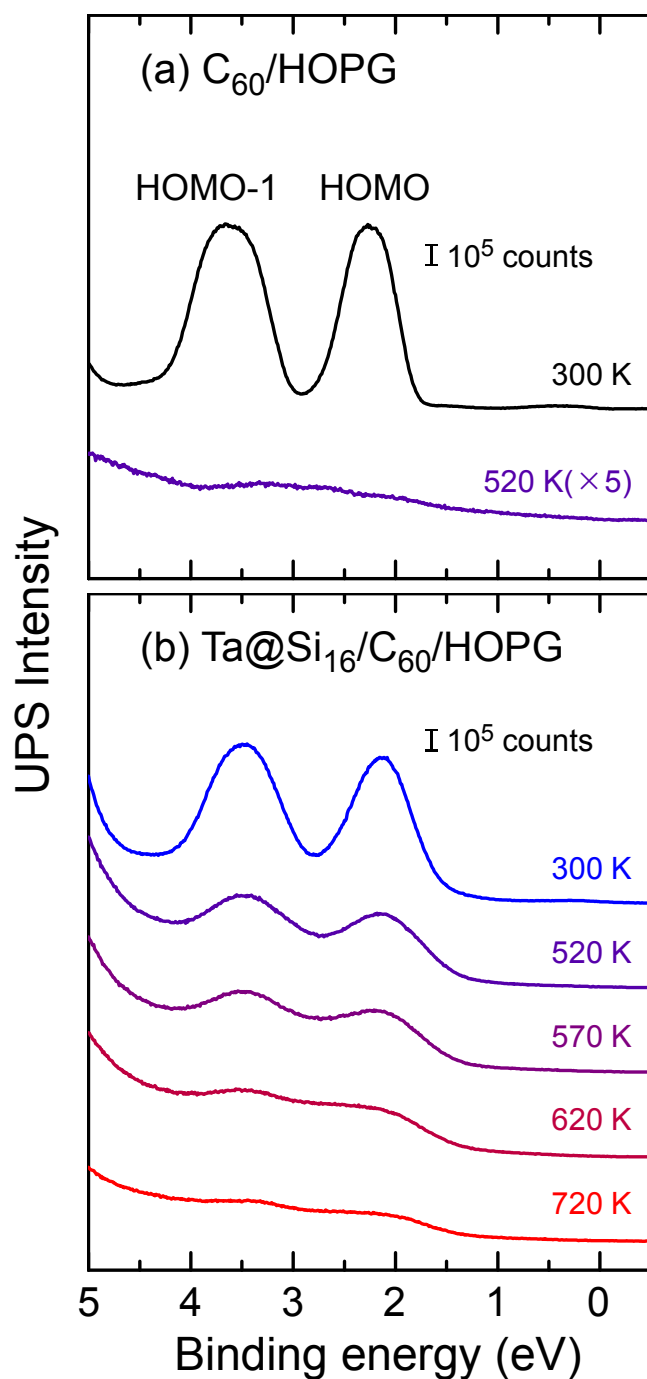


Figure 5.8 UPS spectra for (a) 2 ML  $C_{60}$ /HOPG and (b)  $Ta@Si_{16}/C_{60}$ /HOPG before and after heat treatments. The heating temperatures are noted in the right hand. Reprinted with permission from {Ohta, T.; Shibuta, M.; Tsunoyama, H.; Eguchi, T.; Nakajima, A. Charge transfer complexation of Ta-encapsulating  $Ta@Si_{16}$  superatom with  $C_{60}$ }. Copyright {2016} American Chemical Society.

intense peaks were observed at 2.2 and 3.6 eV below  $E_F$  (Figure 5.8(a) top), which are assignable to  $C_{60}$ -derived the highest occupied molecular orbital (HOMO) and the second HOMO (HOMO-1), respectively.<sup>[46]</sup> When  $C_{60}$ /HOPG was heated to 520 K, these peaks disappeared completely because of the thermal desorption of  $C_{60}$ , consistent with the reported sublimation temperature (469–495 K) at  $2 \times 10^{-8}$  Pa.<sup>[47]</sup> Instead of disappearing, both  $C_{60}$ -derived peaks surprisingly retained approximately 60% of their original intensities at temperatures exceeding 520 K when the Ta@Si<sub>16</sub> nanoclusters were deposited on  $C_{60}$ /HOPG. Since free  $C_{60}$  molecules desorb at 520 K, these residual  $C_{60}$  molecules on the surface may originate from the  $(Ta@Si_{16})^+C_{60}^-$ . The reduced peak intensity observed for the HOMO and HOMO-1 of  $C_{60}$  could be attributed to the desorption of free  $C_{60}$  molecules from the surface. In other words, the UPS spectrum at 520 K would represent the electronic structures of the CT complex  $(Ta@Si_{16})^+C_{60}^-$ . As shown in Figure 5.8(b), the HOMO and HOMO-1 peaks shifted toward lower binding energy by ca. 0.2 eV from those of a pristine  $C_{60}$  film upon heating at 520 K. With the release of surplus  $C_{60}$ , residual  $C_{60}$  should correspond to Ta@Si<sub>16</sub>-complexed  $C_{60}^-$ . Indeed, the spectral behavior was consistent with that of  $C_{60}$  monolayer film on Au substrate,<sup>[34–39]</sup> confirming the formation of  $(Ta@Si_{16})^+C_{60}^-$ .

Upon heating to 570 K in Figure 5.8(b), the spectral features were mostly retained (within 90% intensities), showing that the CT complex did not desorb or decompose within the temperature range. At 620 K, the  $C_{60}$ -derived peaks became weaker and broader, indicative of complex degradation or migration. In fact, the STM image of the heated sample (720 K, 16 h) showed aggregated structures on a HOPG substrate from which free  $C_{60}$  molecules desorbed. Figure 5.9(a) shows an STM image ( $100 \times 100$  nm<sup>2</sup>)

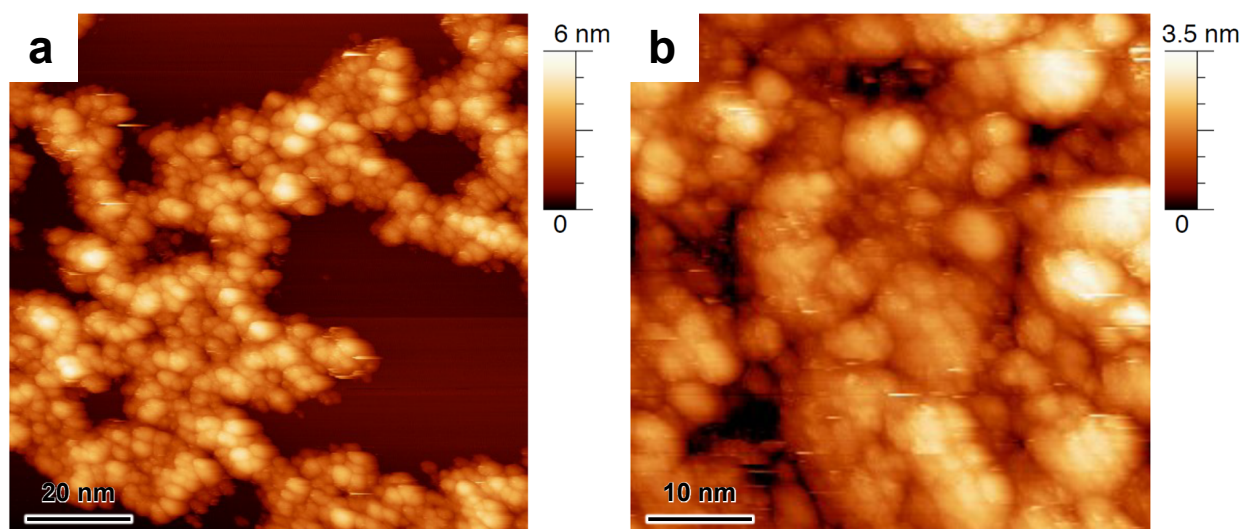


Figure 5.9 STM images of Ta@Si<sub>16</sub>/C<sub>60</sub>/HOPG after heating at 720 K of (a) (100 × 100 nm<sup>2</sup>) and (b) magnified for islands (50 × 50 nm<sup>2</sup>). Reprinted with permission from {Ohta, T.; Shibuta, M.; Tsunoyama, H.; Eguchi, T.; Nakajima, A. Charge transfer complexation of Ta-encapsulating Ta@Si<sub>16</sub> superatom with C<sub>60</sub>}. Copyright {2016} American Chemical Society.

small dots with a height of 2–3 nm are formed on a flat HOPG surface. This result indicates that free C<sub>60</sub> molecules were desorbed from HOPG during heating. Figure 5.9(b) shows a magnified image (50 × 50 nm<sup>2</sup>) for the dense region where Ta@Si<sub>16</sub> nanoclusters cover the substrate. Even after the thermal treatment at 720 K, dot structures were distinguishable in the image, suggesting the robustness of the Ta@Si<sub>16</sub> caged framework.

Furthermore, the temperature dependence of the UPS spectra suggests that the counterpart anion of Ta@Si<sub>16</sub> is switched from C<sub>60</sub> to other chemical species. At 720 K, XPS intensities were almost preserved for Si 2*p* (Figure 5.5(c)) and Ta 4*f* (Figure 5.5(d))

despite a negligible amount of residual  $C_{60}$  was detected in UPS spectra. The most probable species of the counterpart are  $O^{2-}$  ions, as discussed above (see Figure 5.6). Therefore, above 520 K, the counterion exchange started from  $C_{60}^-$  to  $O^{2-}$  together with morphological degradation, producing oxides of Ta@Si<sub>16</sub> superatom.

The result of Ta@Si<sub>16</sub> superatom oxides is consistent to the XPS spectra obtained for Si 2*p* and C 1*s*. As mentioned above, Si atoms were partially oxidized into Si<sup>2+</sup> upon heating. Moreover, the C 1*s* peak may exclusively result from bare HOPG. Note that no valence structures were observed for Ta@Si<sub>16</sub>. Although no explicit justification can be provided, this may be caused by the fluctuation of Ta@Si<sub>16</sub> framework.<sup>[18]</sup>

### 5.3.3 Oxygen exposure

In addition to thermal stability, the chemical robustness of (Ta@Si<sub>16</sub>)<sup>+</sup>C<sub>60</sub><sup>-</sup> toward molecular oxygen (O<sub>2</sub>) was examined at 300 K. Figures 5.10(a) and (b) show background-subtracted XPS spectra of Si 2*p* and Ta 4*f* core levels taken before and after O<sub>2</sub> exposure, respectively. The amount of O<sub>2</sub> exposure was quantified in Langmuir (L, 1 L = 1.33 × 10<sup>-4</sup> Pa s) as noted in the figure. As seen in these core levels, there is almost no significant difference up to the O<sub>2</sub> exposure of 1 × 10<sup>4</sup> L. Even after 5 × 10<sup>10</sup> L O<sub>2</sub> exposure (0.1 MPa × 60 s), the main components of Si 2*p* and Ta 4*f* peaks retained at the original energy positions, indicating that most of the Ta@Si<sub>16</sub> framework survived under ambient conditions. This behavior differs from the performance of Si and Ta surfaces in the bulk, in which they are readily oxidized below 5 L O<sub>2</sub>.<sup>[27,48]</sup> Furthermore, this tolerance to O<sub>2</sub> exposure seems unusual among the alkali fullerenes. For example, potassium atoms in a K<sub>6</sub>C<sub>60</sub> thin film start to react

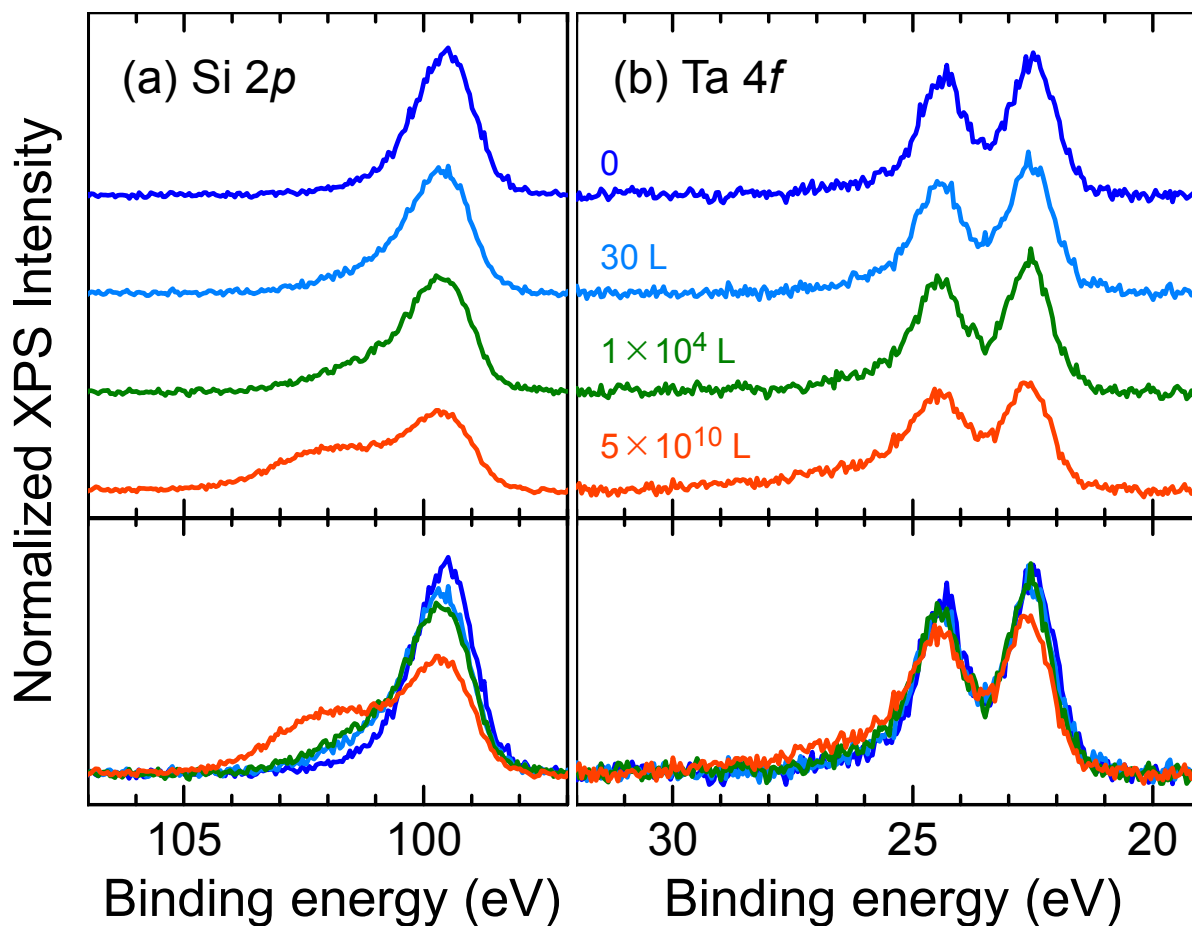


Figure 5.10 XPS spectra normalized at peak areas after Shirley background subtraction for Ta@Si<sub>16</sub>/C<sub>60</sub>/HOPG in (a) Si 2*p* and (b) Ta 4*f* levels at oxygen exposure levels ranging from 0 to  $5 \times 10^{10}$  L, where the backgrounds are subtracted. For comparison, all series of spectra are superimposed at the bottom of each figure. Reprinted with permission from {Ohta, T.; Shibuta, M.; Tsunoyama, H.; Eguchi, T.; Nakajima, A. Charge transfer complexation of Ta-encapsulating Ta@Si<sub>16</sub> superatom with C<sub>60</sub>}. Copyright {2016} American Chemical Society.

with oxygen at 2 L and form a surface oxide (K<sub>2</sub>O<sub>2</sub>) below 10 L.<sup>[49]</sup> Interestingly, XPS spectra of Si 2*p* and Ta 4*f* after exposure to  $5 \times 10^{10}$  L oxygen are very similar to the ones after heating at 720 K, showing that the products were the same. Therefore, the counterpart of Ta@Si<sub>16</sub><sup>+</sup> changed from C<sub>60</sub><sup>-</sup> to O<sup>2-</sup> upon heating or oxygen exposure,

giving rise to Ta@Si<sub>16</sub> superatom oxides.

## 5.4 Conclusions

The chemical states and stability of Ta@Si<sub>16</sub> deposited on a C<sub>60</sub> film on HOPG were evaluated by XPS and UPS. The results reveal that Ta@Si<sub>16</sub> superatoms combined with formed C<sub>60</sub> to generate the one-to-one superatomic complex (Ta@Si<sub>16</sub>)<sup>+</sup>C<sub>60</sub><sup>-</sup> via CT. This complex showed chemical and thermal robustness, demonstrating that the metal-encapsulating silicon nanocluster superatoms have a promising potential to be utilized for building blocks of novel functional materials.

## References

- [1] P. Jena. “Beyond the periodic table of elements: The role of superatoms”. *J. Phys. Chem. Lett.*, **2013**, 4(9), 1432–1442.
- [2] S. A. Claridge, A. Castleman Jr, S. N. Khanna, C. B. Murray, A. Sen and P. S. Weiss. “Cluster-assembled materials”. *ACS Nano*, **2009**, 3(2), 244–255.
- [3] X. Roy, C.-H. Lee, A. C. Crowther, C. L. Schenck, T. Besara, R. A. Lalancette, T. Siegrist, P. W. Stephens, L. E. Brus, P. Kim, et al. “Nanoscale Atoms in Solid-State Chemistry (Science (2013)(157-160))”. *Science*, **2014**, 344(6181), 255.
- [4] H. Yang, Y. Wang, H. Huang, L. Gell, L. Lehtovaara, S. Malola, H. Häkkinen and N. Zheng. “All-thiol-stabilized Ag<sub>44</sub> and Au<sub>12</sub>Ag<sub>32</sub> nanoparticles with single-crystal structures”. *Nat. Commun.*, **2013**, 4.
- [5] J. M. Pettibone, W. A. Osborn, K. Rykaczewski, A. A. Talin, J. E. Bonevich, J. W. Hudgens and M. D. Allendorf. “Surface mediated assembly of small, metastable gold nanoclusters”. *Nanoscale*, **2013**, 5(14), 6558–6566.
- [6] V. Kumar and Y. Kawazoe. “Metal-encapsulated fullerenelike and cubic caged clusters of silicon”. *Phys. Rev. Lett.*, **2001**, 87(4), 045503.
- [7] H. Kawamura, V. Kumar and Y. Kawazoe. “Growth behavior of metal-doped silicon clusters Si<sub>n</sub>M (M= Ti, Zr, Hf; n= 8–16)”. *Phys. Rev. B*, **2005**, 71(7), 075423.
- [8] K. Koyasu, M. Akutsu, M. Mitsui and A. Nakajima. “Selective Formation of MSi<sub>16</sub> (M= Sc, Ti, and V)”. *J. Am. Chem. Soc.*, **2005**, 127(14), 4998–4999.
- [9] M. Torres, E. Fernández and L. Balbás. “Theoretical study of isoelectronic Si<sub>n</sub>M

- clusters (M= Sc<sup>-</sup>, Ti, V<sup>+</sup>; n= 14–18)”. *Phys. Rev. B*, **2007**, 75(20), 205425.
- [10] H. Cantera-López, L. Balbás and G. Borstel. “First-principles calculations of structural and electronic properties of Ta-doped Si clusters, wires, and bulk systems”. *Phys. Rev. B*, **2011**, 83(7), 075434.
- [11] T. Iwasa and A. Nakajima. “Geometric, electronic, and optical properties of a superatomic heterodimer and trimer: Sc@Si<sub>16</sub>-V@Si<sub>16</sub> and Sc@Si<sub>16</sub>-Ti@Si<sub>16</sub>-V@Si<sub>16</sub>”. *J. Phys. Chem. C*, **2012**, 116(26), 14071–14077.
- [12] J. U. Reveles and S. N. Khanna. “Electronic counting rules for the stability of metal-silicon clusters”. *Phys. Rev. B*, **2006**, 74(3), 035435.
- [13] K. Koyasu, J. Atobe, M. Akutsu, M. Mitsui and A. Nakajima. “Electronic and geometric stabilities of clusters with transition metal encapsulated by silicon”. *J. Phys. Chem. A*, **2007**, 111(1), 42–49.
- [14] J. Lau, K. Hirsch, P. Klar, A. Langenberg, F. Lofink, R. Richter, J. Rittmann, M. Vogel, V. Zamudio-Bayer, T. Möller, et al. “X-ray spectroscopy reveals high symmetry and electronic shell structure of transition-metal-doped silicon clusters”. *Phys. Rev. A*, **2009**, 79(5), 053201.
- [15] A. C. Templeton, W. P. Wuelfing and R. W. Murray. “Monolayer-protected cluster molecules”. *Acc. Chem. Res.*, **2000**, 33(1), 27–36.
- [16] S. Yamazoe, K. Koyasu and T. Tsukuda. “Nonscalable oxidation catalysis of gold clusters”. *Acc. Chem. Res.*, **2013**, 47(3), 816–824.
- [17] R. Jin. “Quantum sized, thiolate-protected gold nanoclusters”. *Nanoscale*, **2010**, 2(3), 343–362.
- [18] M. Shibuta, T. Ohta, M. Nakaya, H. Tsunoyama, T. Eguchi and A. Naka-

- jima. “Chemical characterization of an alkali-like superatom consisting of a Ta-encapsulating Si<sub>16</sub> Cage”. *J. Am. Chem. Soc.*, **2015**, 137(44), 14015–14018.
- [19] M. Nakaya, T. Iwasa, H. Tsunoyama, T. Eguchi and A. Nakajima. “Formation of a superatom monolayer using gas-phase-synthesized Ta@Si<sub>16</sub> nanocluster ions”. *Nanoscale*, **2014**, 6(24), 14702–14707.
- [20] M. Nakaya, T. Iwasa, H. Tsunoyama, T. Eguchi and A. Nakajima. “Heterodimerization via the covalent bonding of Ta@Si<sub>16</sub> nanoclusters and C<sub>60</sub> Molecules”. *J. Phys. Chem. C*, **2015**, 119(20), 10962–10968.
- [21] T. Ohta, M. Shibuta, H. Tsunoyama, Y. Negishi, T. Eguchi and A. Nakajima. “Size and structure dependence of electronic states in thiolate-protected gold nanoclusters of Au<sub>25</sub>(SR)<sub>18</sub>, Au<sub>38</sub>(SR)<sub>24</sub>, and Au<sub>144</sub>(SR)<sub>60</sub>”. *J. Phys. Chem. C*, **2013**, 117(7), 3674–3679.
- [22] G. Rangelov and T. Fauster. “Thermally-induced evolution of codeposited Co-Si layers on Si(100) surfaces”. *Surf. Sci.*, **1996**, 365(2), 403–410.
- [23] D. M. Riffe and G. Wertheim. “Ta(110) surface and subsurface core-level shifts and 4f<sub>7/2</sub> line shapes”. *Phys. Rev. B*, **1993**, 47(11), 6672.
- [24] J. H. Scofield. “Hartree-Slater subshell photoionization cross-sections at 1254 and 1487 eV”. *J. Electron Spectrosc. Relat. Phenom.*, **1976**, 8(2), 129–137.
- [25] J. Hedman, Y. Baer, A. Berndtsson, M. Klasson, G. Leonhardt, R. Nilsson and C. Nordling. “Influence of doping on the electron spectrum of silicon”. *J. Electron Spectrosc. Relat. Phenom.*, **1972**, 1(1), 101–104.
- [26] S.-F. Ho, S. Contarini and J. Rabalais. “Ion-beam-induced chemical changes in the oxyanions (Mo<sub>y</sub><sup>n-</sup>) and oxides (Mo<sub>x</sub>) where M= chromium, molybdenum, tungsten,

- vanadium, niobium and tantalum”. *J. Phys. Chem.*, **1987**, 91(18), 4779–4788.
- [27] M. Gomoyunova, I. Pronin, D. Malygin, N. Gall, D. Vyalikh and S. Molodtsov. “Photoemission study of cobalt interaction with the oxidized Si(100)  $2 \times 1$  surface”. *Surf. Sci.*, **2006**, 600(12), 2449–2456.
- [28] J. Oh, H. Yeom, Y. Hagimoto, K. Ono, M. Oshima, N. Hirashita, M. Nywa, A. Toriumi and A. Kakizaki. “Chemical structure of the ultrathin SiO<sub>2</sub>/Si(100) interface: An angle-resolved Si 2*p* photoemission study”. *Phys. Rev. B*, **2001**, 63(20), 205310.
- [29] F. Himpsel, F. McFeely, A. Taleb-Ibrahimi, J. Yarmoff and G. Hollinger. “Microscopic structure of the SiO<sub>2</sub>/Si interface”. *Phys. Rev. B*, **1988**, 38(9), 6084.
- [30] D. M. Guldi. “Fullerenes: three dimensional electron acceptor materials”. *Chem. Commun.*, **2000**, (5), 321–327.
- [31] J. Leiro, M. Heinonen, T. Laiho and I. Batirev. “Core-level XPS spectra of fullerene, highly oriented pyrolytic graphite, and glassy carbon”. *J. Electron Spectrosc. Relat. Phenom.*, **2003**, 128(2), 205–213.
- [32] W. M. Tong, D. A. Ohlberg, H. K. You, R. S. Williams, S. J. Anz, M. M. Alvarez, R. L. Whetten, Y. Rubin and F. N. Diederich. “X-ray diffraction and electron spectroscopy of epitaxial molecular Buckminsterfullerene films”. *J. Phys. Chem.*, **1991**, 95(12), 4709–4712.
- [33] H.-N. Li, X.-X. Wang and W.-F. Ding. “Electron attenuation lengths in fullerene and fullerides”. *J. Electron Spectrosc. Relat. Phenom.*, **2006**, 153(3), 96–101.
- [34] S. Modesti, S. Cerasari and P. Rudolf. “Determination of charge states of C<sub>60</sub> adsorbed on metal surfaces”. *Phys. Rev. Lett.*, **1993**, 71(15), 2469.
- [35] B. Hoogenboom, R. Hesper, L. Tjeng and G. Sawatzky. “Charge transfer and

- doping-dependent hybridization of C<sub>60</sub> on noble metals”. *Phys. Rev. B*, **1998**, 57(19), 11939.
- [36] P. Rudolf, M. S. Golden and P. A. Brühwiler. “Studies of fullerenes by the excitation, emission, and scattering of electrons”. *J. Electron Spectrosc. Relat. Phenom.*, **1999**, 100(1), 409–433.
- [37] S. Chase, W. Bacsa, M. Mitch, L. Piloni and J. Lannin. “Surface-enhanced Raman scattering and photoemission of C<sub>60</sub> on noble-metal surfaces”. *Phys. Rev. B*, **1992**, 46(12), 7873.
- [38] S. Kang, Y. Yi, C. Kim and C. Whang. “Electronic structure of C<sub>60</sub> on Au studied by using X-ray and UV photoelectron spectroscopy”. *J. Korean Phys. Soc.*, **2005**, 46(5), 1148–1151.
- [39] F. Schiller, M. Ruiz-Osés, J. Ortega, P. Segovia, J. Martínez-Blanco, B. Doyle, V. Pérez-Dieste, J. Lobo, N. Néel, R. Berndt, et al. “Electronic structure of C<sub>60</sub> on Au(887)”. *J. Chem. Phys.*, **2006**, 125(14), 144719.
- [40] G. Pacchioni and P. S. Bagus. “Theoretical analysis of the O(1s) binding-energy shifts in alkaline-earth oxides: Chemical or electrostatic contributions”. *Phys. Rev. B*, **1994**, 50(4), 2576.
- [41] V. Dimitrov and T. Komatsu. “Classification of simple oxides: a polarizability approach”. *J. Solid State Chem.*, **2002**, 163(1), 100–112.
- [42] W. Mullins. “Optical basicity of metal oxides and XPS measurement”. *Surf. Sci.*, **1992**, 262(3), L144–L146.
- [43] E. Atanassova and D. Spassov. “X-ray photoelectron spectroscopy of thermal thin Ta<sub>2</sub>O<sub>5</sub> films on Si”. *Appl. Surf. Sci.*, **1998**, 135(1), 71–82.

- [44] E. Atanassova, T. Dimitrova and J. Koprinarova. “AES and XPS study of thin RF-sputtered Ta<sub>2</sub>O<sub>5</sub> layers”. *Appl. Surf. Sci.*, **1995**, 84(2), 193–202.
- [45] J. Thomas and L. Hammer. “A photoelectron spectroscopy study of CF<sub>4</sub>/H<sub>2</sub> reactive ion etching residue on tantalum disilicide”. *J. Electrochem. Soc.*, **1989**, 136(7), 2004–2010.
- [46] C. T. Chen, L. H. Tjeng, P. Rudolf, G. Meigs, J. E. Rowe, J. Chen, J. P. J. McCauley, A. B. Smith, A. R. McGhie, W. J. Romanow and E. W. Plummer. “Electronic states and phases of K<sub>x</sub>C<sub>60</sub> from photoemission and X-ray absorption spectroscopy”. *Nature*, **1991**, 352(6336), 603–605.
- [47] V. Piacente, G. Gigli, P. Scardala, A. Giustini and D. Ferro. “Vapor pressure of C<sub>60</sub> buckminsterfullerene”. *J. Phys. Chem.*, **1995**, 99(38), 14052–14057.
- [48] J. V. d. Veen, F. Himpsel and D. Eastman. “Chemisorption-induced 4*f*-core-electron binding-energy shifts for surface atoms of W(111), W(100), and Ta(111)”. *Phys. Rev. B*, **1982**, 25(12), 7388.
- [49] P. Benning, D. Poirier, T. Ohno, Y. Chen, M. Jost, F. Stepniak, G. Kroll, J. Weaver, J. Fure and R. Smalley. “C<sub>60</sub> and C<sub>70</sub> fullerenes and potassium fullerides”. *Phys. Rev. B*, **1992**, 45(12), 6899.

## Chapter 6

# Conclusions

## 6.1 Conclusions

In this thesis, the properties of deposited nanoclusters have been investigated using photoelectron spectroscopies.

At first, the electronic states of three different sizes of compositionally precise thiolate-protected gold nanoclusters,  $\text{Au}_{25}(\text{SR})_{18}$ ,  $\text{Au}_{38}(\text{SR})_{24}$ , and  $\text{Au}_{144}(\text{SR})_{60}$  ( $\text{R} = \text{C}_{12}\text{H}_{25}$ ), have been evaluated by X-ray photoemission spectroscopy (XPS). The Au  $4f$  core-levels of the nanoclusters are well reproduced by two spectral components derived from centered core-Au and positively charged shell-Au atoms, the numbers of which are determined based on the atomic structure of the nanoclusters. The spin-orbit splitting of Au  $5d_{5/2}$  and  $5d_{3/2}$  in the valence band becomes narrower than that of bulk Au, depending on the cluster size, which is quantitatively characterized by a reduction in the average coordination number of Au. The Au  $5d$  valence-band spectra also show that the charge reorganization of  $5d$  electrons induced by interaction with thiol molecules is more significant for the  $5d_{5/2}$  than the  $5d_{3/2}$  level.

Next, in order to evaluate the properties without interactions between core cluster structure and ligand protections, “naked clusters” have been focused on. Nanocluster deposition system was developed to reveal the chemical characterization for an alkali-like superatom consisting of a Ta-encapsulating  $\text{Si}_{16}$  cage,  $\text{Ta}@\text{Si}_{16}$ . After evaluating the performance of the apparatus, a thin  $\text{Ta}@\text{Si}_{16}$  film was produced on a graphite substrate, and the local electronic structure of the cage atoms was clarified using XPS in an element specific manner. The XPS spectra derived from Ta  $4f$  and Si  $2p$  core

levels have been well modeled with a single chemical component, revealing the formation of a symmetric Si cage around the Ta atom in the deposited nanoclusters. On chemical treatments by heating or oxygen exposure, it is found that the deposited Ta@Si<sub>16</sub> is thermally stable up to 700 K and is also exceptionally less reactive toward oxygen compared to other Ta-Si nanoclusters, although some heat degradation and oxidation accompany the treatments.

In order to reveal the superatomic character of Ta@Si<sub>16</sub>, it has been deposited on an electron acceptable C<sub>60</sub> fullerene film, and evaluated by XPS and ultraviolet photoelectron spectroscopy (UPS). XPS results for Si, Ta, and C showed that Ta@Si<sub>16</sub> combines with a single C<sub>60</sub> molecule to form the superatomic charge transfer (CT) complex, (Ta@Si<sub>16</sub>)<sup>+</sup>C<sub>60</sub><sup>-</sup>. The high thermal and chemical robustness of the superatomic CT complex has been revealed by the XPS and UPS measurements conducted before and after heat treatment and oxygen exposure. Even after heated to 720 K or subjected to ambient oxygen, Ta@Si<sub>16</sub> retained its original framework, and just forming oxides of Ta@Si<sub>16</sub> superatom. These results show the promising possibility of applying Ta@Si<sub>16</sub> as a building block to fabricate cluster-assembled materials consisting of naked nanoclusters.

## 6.2 Outlooks of this research

As described above, the physical properties of mass-selectively deposited nanoclusters have been evaluated relating to their structures. This work will open up new prospects for investigation of assembled nanoclusters and bridge the gap between the basic science

and technology based on nanoclusters.

In this thesis, Ta@Si<sub>16</sub> was especially focused on among the metal-encapsulating silicon cage clusters (M@Si<sub>16</sub>), but the cluster generation system developed so far can also synthesize other M@Si<sub>16</sub> nanoclusters. By combining them, a hetero-dimer film made of two types of M@Si<sub>16</sub> can be synthesized. Since such a dimer would have a strong electric dipole moment due to charge transfer character, it has a potential to be utilized for devices.<sup>[1]</sup> Furthermore, assembling nanoclusters with atomic level precision can open up a new era in material science.<sup>[2]</sup> I hope that this work will help to promote the investigations of such superatomic nanocluster-based materials.

## References

- [1] T. Iwasa and A. Nakajima. “Geometric, electronic, and optical properties of a superatomic heterodimer and trimer:  $\text{Sc@Si}_{16}\text{-V@Si}_{16}$  and  $\text{Sc@Si}_{16}\text{-Ti@Si}_{16}\text{-V@Si}_{16}$ ”. *J. Phys. Chem. C*, **2012**, 116(26), 14071–14077.
- [2] P. Jena. “Beyond the periodic table of elements: The role of superatoms”. *J. Phys. Chem. Lett.*, **2013**, 4(9), 1432–1442.

# Appendix: Publications and Presentations

## Papers

- [1] T. Ohta, M. Shibuta, H. Tsunoyama, Y. Negishi, T. Eguchi, and A. Nakajima. “Size and structure dependence of electronic states in thiolate-protected gold nanoclusters of  $\text{Au}_{25}(\text{SR})_{18}$ ,  $\text{Au}_{38}(\text{SR})_{24}$ , and  $\text{Au}_{144}(\text{SR})_{60}$ ”, *J. Phys. Chem. C*, **2013**, 117(7), 3674–3679.
- [2] M. Shibuta, T. Ohta, M. Nakaya, H. Tsunoyama, T. Eguchi, and A. Nakajima. “Chemical characterization of an alkali-like superatom consisting of a Ta-encapsulating  $\text{Si}_{16}$  cage”, *J. Am. Chem. Soc.*, **2015**, 134(44), 14015–14018.
- [3] T. Ohta, M. Shibuta, H. Tsunoyama, T. Eguchi, and A. Nakajima. “Charge transfer complexation of Ta-encapsulating  $\text{Ta@Si}_{16}$  superatom with  $\text{C}_{60}$ ”, *J. Phys. Chem. C*, **2016**, 120(28), 15265–15271.
- [4] M. Shibuta, K. Yamamoto, T. Ohta, M. Nakaya, T. Eguchi and A. Nakajima. “Direct observation of photocarrier electron dynamics in  $\text{C}_{60}$  films on graphite by time-resolved two-photon photoemission”, submitted.

## Poster presentations at international conferences

- [1] T. Ohta, M. Shibuta, H. Tsunoyama, Y. Negishi, T. Eguchi, and A. Nakajima. “Size and Structure Dependence of Electronic States in Thiolate-Protected Gold Nanoclusters of  $\text{Au}_{25}(\text{SR})_{18}$ ,  $\text{Au}_{38}(\text{SR})_{24}$ , and  $\text{Au}_{144}(\text{SR})_{60}$ ”, Symposium on Size Selected Clusters 2013, Davos, Switzerland (March 2013).
- [2] T. Ohta, M. Shibuta, H. Tsunoyama, T. Eguchi, and A. Nakajima. “Chemical

Properties of Size-selected Metal-Silicon Binary Clusters Deposited on Graphite Substrate Studied by X-ray Photoelectron Spectroscopy”, 31st Symposium on Chemical Kinetics and Dynamics, Sapporo, Japan (June 2015).

- [3] T. Ohta, M. Shibuta, H. Tsunoyama, T. Eguchi, and A. Nakajima. “Chemical Evaluation of Ta@Si<sub>16</sub> Nanocluster Deposited on Graphite Surface by X-ray Photoelectron Spectroscopy”, 2015 International Chemical Congress of Pacific Basin Societies, Honolulu, USA (December 2015).

## Poster presentations at domestic conferences

- [1] 太田努, 渋田昌弘, 角山寛規, 根岸雄一, 江口豊明, 中嶋敦. “X線光電子分光法によるチオレート保護金クラスターの研究：電子状態のサイズ依存性と幾何構造との相関”, ナノ学会第10回大会, 大阪市 (2012年6月).
- [2] 太田努, 渋田昌弘, 角山寛規, 根岸雄一, 江口豊明, 中嶋敦. “精密合成・単離されたチオレート保護金クラスターのX線光電子分光：電子状態のサイズ依存性と幾何構造との相関”, 表面・界面スペクトロスコーピー2012, 吹田市 (大阪府) (2012年12月).